High-resolution grating-based phase-contrast imaging for synchrotron radiation sources

Vom Promotionsausschuss des
Fachbereichs Physik der
Universität Hamburg zur Erlangung des
akademischen Grades 'Doctor rerum naturalium'
genehmigte Dissertation

vorgelegt von Alexander C. Hipp aus Bad Friedrichshall

Hamburg, 2018

High-resolution grating-based phase-contrast imaging at synchrotron radiation sources

Alexander C. Hipp

Abstract

The advantages of phase-contrast based imaging in comparison to conventional attenuation-based radiography or tomography, especially for the investigation of low absorbing material, has been demonstrated multiple times. On the one hand, grating-based phase-contrast imaging can provide a better contrast for such materials, but on the other hand it usually comes with a limited spatial resolution.

Aim of this work is the instrumentation of a grating-based phase-contrast imaging setup at the synchrotron radiation source PETRA III (DESY), to allow for quantitative phase-contrast imaging with a spatial resolution in the range a few micrometer. Two types of setups, namely single-grating and double-grating interferometer were designed and established. Both setups were optimised to cover an energy range as large as possible and to allow for a routine operation.

Both setup types were studied and compared by simulations with the focus on the spatial resolution and signal-to-noise ratio as well as the influence of instabilities of the setup. The results of simulations indicate, that the single-grating interferometer is the preferable setup type. Although the performance in terms of signal-to-noise ratio and resolution is comparable for both setup types, the single-grating interferometer benefits from a much higher reliability through its high robustness against grating instabilities. Phantom samples were especially designed to verify the simulations results by equivalent experiments. The quantitative data obtained from the measurements shows a high coincidence with the simulation prediction. The experimental results moreover prove, that the presented single grating setup is an instrument that allows for a spatial resolution of up to 5 μm at a field of view of 7 mm.

Hochauflösende gitterbasierte Phasenkontrastbildgebung an Synchrotronstrahlungsquellen

Zusammenfassung

Diverse Vorteile auf Phasenkontrast basierender Bildgebung gegenüber konventioneller absorptionsbasierte Radiographie oder Tomographie, besonders für die Untersuchung von schwach absorbierenden Materialien, wurden schon mehrfach demonstriert. Zwar kann der verbesserte Bildkontrast gitterbasierter Phasenkontrastbildgebung von großem Vorteil sein, jedoch ist zumeist die vergleichsweise limitierte räumliche Auflösung von Nachteil.

Ziel dieser Arbeit ist der Aufbau eines Gitterinterferometers an der Synchrotron-Strahlungsquelle PETRA III (DESY), um quantitative Phasenkontrastbildgebung mit einer räumliche Auflösung im Bereich weniger Mikrometer zu ermöglichen. Hierzu wurden zwei verschiedene Arten von Gitterinterferometer, basierend auf einem einzelnen oder auf zwei Gittern, entworfen und aufgebaut. Beide Aufbauten wurden dahingehend optimiert, einen möglichst weiten Energiebereich abzudecken und einen routinemäßigen Betrieb zu gewährleisten. Mit besonderem Augenmerk auf die Leistungsfähigkeit, die das Ein-Gitter-Interferometer bietet, wird hier analysiert wie sich dieser Aufbau mit dem konventionellen Zwei-Gitter-Interferometer misst. Unter die Bewertungskriterien fallen hierbei neben der räumlichen Auflösung besonders auch das Signal zu Rausch Verhalten sowie die Stabilität des jeweiligen Aufbaus.

Für diese Auswertungen wurden Testkörper bestehend aus wohldefinierten Materialien konstruiert und mit den jeweiligen Aufbauten untersucht. Basierend auf den Ergebnissen von Simulationen und den dazu passenden Experimenten kann gezeigt werden, dass ein Ein-Gitter-Interferometer bestens dazu geeignet ist quantitative Phasenkontrastbildgebung mit einer räumlichen Auflösung von bis zu $5\ \mu m$, bei einem Sichtfeld von $7\ mm$, zu ermöglichen.

Eidesstattliche Versicherung / Declaration on oath

Hiermit versichere ich an Eides statt, die vorliegende Dissertationsschrift selbst verfasst und keine anderen als die angegebenen Hilfsmittel und Quellen benutzt zu haben.

Die eingereichte schriftliche Fassung entspricht der auf dem elektronischen Speichermedium.

Die Dissertation wurde in der vorgelegten oder einer ähnlichen Form nicht schon einmal in einem früheren Promotionsverfahren angenommen oder als ungenügend beurteilt.

Regensburg, den 22.05.2018

_____
Alexander Hipp

Contents

1 Introduction

X-ray computed tomography (CT) has taken a leading role in the field of non-destructive three dimensional imaging. Thanks to the high spatial resolution, penetration depth and the fast acquisition time of present systems, X-ray micro-tomography is an essential imaging modality for materials testing and morphological studies. Conducted at synchrotron radiation facilities, the performance of the system can benefit immensely from the high photon flux provided by the source and the possibility of monochromatic radiation. Since the development of synchrotron-radiation-based microtomography ($SR\mu CT$) [1], its advantages have become important for a continuously growing number of researchers. The reachable high spatial and density resolution make it a valuable investigation tool for a broad range of applications reaching from biological soft tissue samples to high dense metal foams [2, 3, 4, 5].

Although $SR\mu CT$ can reach a good contrast for large a variety of samples, it still comes with some drawbacks. Especially for low absorbing materials such as biological soft tissues or light polymer samples, the reachable contrast is strongly dependent on the applied photon energy. A higher contrast for those materials can be achieved by staining the object with some contrast agent. However, this brings additional efforts to the sample preparation due to the staining process, and often must not be applied e.g. for unique samples, as the original state of the sample is changed during the preparation process. Another difficulty using attenuation-based tomography is the investigation of multi-material objects. According to the photoelectric effect, the attenuation coefficient is approximately proportional to Z^n (n is a number between 4 and 5), thus attenuation based tomography lacks a suitable contrast among different low-Z materials in the presence of high-Z material components in the sample.

To overcome this limitation, several new X-ray phase-contrast imaging methods have been developed at synchrotron radiation facilities [6, 7]. Instead of exploit-

ing the attenuation of the X-ray wavefront induced by the object, phase-contrast focuses on the phase shift induced by the object. Particularly for low-Z material, the phase-shift cross-section is in the order of 100 to 1000 larger than the attenuation cross-section [8, 9]. As the observed phase-shift is linear proportional to the electron density of the investigated material [10], phase-contrast measurements allow to investigate samples demanding for a large dynamic range in the observed contrast.

Propagation-based phase-contrast [11, 12, 13] and grating-based phase-contrast [14, 15] using a grating interferometer are the most common phase-contrast techniques combined with micro-tomography at synchrotron radiation sources. Especially the grating-interferometer based systems benefit from the possibility for quantitative evaluation in terms of electron density. Moreover, a qualitative description of the scattering, called dark field signal, can be captured at the same time.

The development of lab sources and optics enables both methods to be applied with conventional X-ray sources [16, 17], including commercial full-protection devices [18, 19, 20]. However, synchrotron radiation sources still have many advantages, due to their high flux, monochromatic radiation and especially their high coherence. The high flux of the synchrotron radiation gives the possibility for high throughput experiments, while the monochromaticity gives access to quantitative results [21, 22, 10] without need for a reference material as with a polychromatic source [23]. Thus very high spatial resolution can be achieved keeping a good photon statistics and a short scan duration.

The aim of this work was to establish a grating interferometer for differential phase-contrast measurements at the two PETRA III beamline P05 and P07, with the focus on a high spatial resolution, a reasonable acquisition time and the operation as a user experiment. As the whole project was carried out within the framework of the virtual institute *VI-NXMM*[1] and the Helmholtz portfolio project *Technology and Medicine*[2] the applicability for a wide range of different experiments was a key criteria for the developed instrument.

With the target on a reliable and robust setup to enable the fast and direct access

---

[1]Virtual Institute New X-ray analytical Methods in Material science,
   http://www.roentgenbildgebung.de
[2]Technology and Medicine - in vivo multimodal imaging of polymeric biomaterials

to the synchrotron radiation user community, the interferometer has to provide a high stability in order to allow a fully automatised processing and reconstruction routine with a minimum manual intervention. The gratings are the decisive component for a interferometer, which controls the system performance and quality of the results. The common implementation of a grating interferometer at synchrotron radiation facilities consists of two gratings, a phase grating and an absorption grating. In the hard X-ray regime, high aspect ratios (>100) of the grating structures are necessary for the absorption grating. One common problem for high aspect ratios is the lamellas instability during the fabrication process [24, 25].

To overcome the limitations from grating fabrications, the usability and performance of a single-grating interferometer has been thoroughly investigated. The potential of such an interferometer for high spatial resolution imaging has already been demonstrated [26], but yet misses a profound investigation of its capabilities and limitations. This work contains an in-depth performance analysis of a single-grating interferometer based-on simulations and its experimental verifications. For both investigations the key performance indicators which define the accuracy of the measurement are given by the signal-to-noise ratio and the achievable spatial resolution. A state-of-the-art double-grating interferometer was also used and analysed to make a comparative study between single- and double-grating setup. Besides spatial resolution and signal to noise ratio the performance analysis comprises the presence of image artefacts and stability.

2 Theory

2.1 X-Ray Interaction with Matter

X-rays are electromagnetic (EM) waves with wavelengths comparable to the size of an atom. When an X-ray beam passes through an object, the interaction can take complex forms depending on the sample [27, 28] and photon characteristics [29]. The high penetration ability of X-rays makes radiography and tomography valuable tools to investigate bulk material [28]. Particularly hard X-rays (wavelength $\lambda < 1\mathring{A}$) [30] are preferable in materials science research due to larger penetration depths. The X-ray interaction with matter is composed of major types: coherent scattering (also known as elastic scattering) [28], Compton scattering (inelastic scattering), photoelectric effect, pair production and photodisintegration [31]. Among these, coherent scattering, Compton scattering and photoelectric absorption are the most important processes in the typical energy range from 1 keV to 100 keV, which is commonly used for materials science.

The complex index of refraction $\underline{n}$ is used to quantitatively describe the X-ray interaction with matter:

$$\underline{n} = n + i\beta \ . \tag{2.1}$$

Here, n is the real part of the refractive index, defined by

$$n = \frac{c}{v} \tag{2.2}$$

with c being the speed of light and v as the phase velocity of the electromagnetic wave. For X-rays, the real part of the refractive index usually is close to but smaller than 1 and therefore the refractive index often is written as

$$\underline{n} = 1 - \delta + i\beta. \tag{2.3}$$
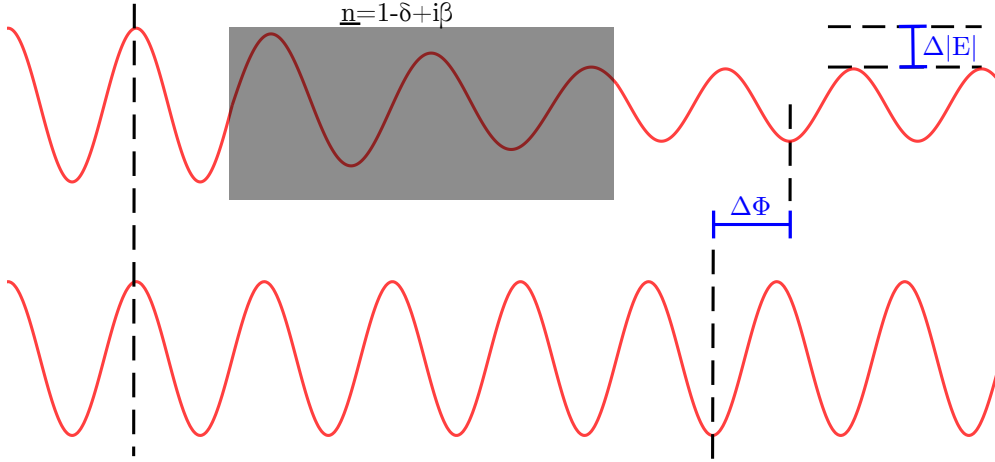
Figure 2.1: Monochromatic X-ray wave passing through vacuum and an opaque object. The wave passing through the object gets weaken in its amplitude ($\Delta|E|$) and changes its wavelength within the object resulting in a phase shift ($\Delta\Phi$) compared to a reference wave.

The so-called *refractive index decrement* δ indicates a phase shift to the penetrating electro-magnetic wave. The *extinction coefficient* β is a measure for the attenuation of the electromagnetic wave caused by the material. Real (n) and imaginary part (β) can be expressed by the atomic scattering factors f_1 and f_2, the classical electron radius r_e, the wavelength λ and the atom density ρ_i:

$$\underline{n} = 1 - \delta + i\beta = 1 - \frac{r_e}{2\pi}\lambda^2 \sum_i \rho_i(f_{i,1} + if_{i,2}) . \tag{2.4}$$

The imaginary part of the scattering factor is derived from the atomic photo-absorption cross section σ_a:

$$f_2 = \frac{\sigma_a}{2r_e\lambda}. \tag{2.5}$$

The real part of the atomic scattering factor is related to the imaginary part by the Kramers-Kronig dispersion relation [31]:

$$f_1 = Z' + \frac{1}{\pi r_e hc} \int\limits_0^\infty \frac{\epsilon^2 \sigma_a(\epsilon)}{E^2 - \epsilon^2}. \tag{2.6}$$

In the high energy regime, f_1 approaches to Z', which differs from the atomic num-

ber Z by a small relativistic correction. For hard X-rays δ can be approximately described as

$$\delta \approx \frac{r_e}{2\pi}\lambda^2 \sum_i \rho_i Z_i = \frac{\rho_e r_e}{2\pi}\lambda^2 \ , \tag{2.7}$$

which is proportional to the electron density ρ_e.

2.1.1 Attenuation Contrast / Phase Contrast

Attenuation-based contrast is defined by the intensity loss of the incoming X-ray beam after penetrating an object. The beam intensity I_0 before and the intensity I behind the object are connected by the Beer-Lambert Law [33]:

$$I = I_0 \cdot e^{-\mu d} \tag{2.8}$$

Here, $\mu = 4\pi\beta/\lambda$ is the attenuation coefficient and d the thickness of the sample. For an inhomogeneous object with a non-constant attenuation coefficient, the equation can be written in differential form. The intensity behind the sample is then given by the line integral through the object.

$$\frac{dI}{I(z')} = -\mu(z')dz' \quad \Leftrightarrow \quad I(z) = I_0 \cdot e^{-\int \mu(z')dz'} \tag{2.9}$$

Phase-contrast describes the phase difference $\Delta\Phi$ of an electro-magnetic wave to a reference wave, with wavelength λ, resulting from the penetration of an object with thickness d.

$$\Phi_r(d) = \Phi_0 - 2\pi d/\lambda \tag{2.10}$$

$$\Phi_s(d) = \Phi_0 - 2\pi d(1 - \delta)/\lambda \tag{2.11}$$

$$\Delta\Phi = \Phi_s(d) - \Phi_r(d) = 2\pi\delta d/\lambda \tag{2.12}$$

Here, Φ_s is the phase of the EM-wave that passed through the sample and Φ_r the phase of a reference wave through free space with refractive index $n = 1$. Analogue to the Beer-Lambert Law (eq. 2.9), equation 2.12 can be written in a differential form:

$$d\Phi = \frac{-2\pi\delta(z')dz'}{\lambda} \quad \Leftrightarrow \quad \Delta\Phi(z) = \frac{-2\pi}{\lambda}\int \delta(z')dz' \tag{2.13}$$

Unlike the direct measurement of attenuation contrast, the phase-contrast signal can only be derived from the measurement of intensity. Although retrieving the phase signal comes with additional effort than retrieving the attenuation signal, the advantages cannot be ignored, especially for low absorbing material.

The phase-shift cross-section of low-Z material is about a factor of 1000 higher than the attenuation cross-section [8]. Thus for a given material, phase-contrast can achieve the same level as attenuation-contrast at much higher photon energies. Especially when working with radiation sensitive material like (living) biological samples, a higher energy can effectively decrease the dose hazard of the sample during the experiment.

Plotting the cross section against the atomic number of the elements, it can be seen that the ratio of δ to β is strongly dependent on the atomic number Z. Figure 2.2A shows the δ and β values of the refractive index dependent on the atomic number Z for an X-ray energy of 20 keV. Attenuation and phase-shift rise with the atomic number increase. Due to the influence of the atomic density, the phase-shift of low-Z materials is dominated by a periodic pattern as consequence of their atom shell structure [34]. For the low Z materials the ratio of δ to β has an order of magnitude of 10^4 (Z=3-6). With ascending atomic number the ratio of δ to β is decreasing towards an order of magnitude of 10^2 (Z>20). This is of great importance when investigating composite-materials samples. Figure 2.2B shows the relative signal strength given by the material normalised to the element with the highest δ respectively β value. While the measurement of the phase-shift would still give a signal strength of around 20% for the low Z material, the attenuation signal would be lower then 5% for all elements with Z lower then 19 (Ca). The comparison shows that for a non-binary system the distinction of material by contrast level will be much easier in phase contrast than through attenuation. Especially in a composite material with a complex mixture from high Z components and several low Z components, the separation of the different weak absorbing material is the main advantage of the phase-contrast. For binary systems where the attenuation-based contrast level at the applicable energy is sufficient, phase-contrast does not provide any additional or superior information.
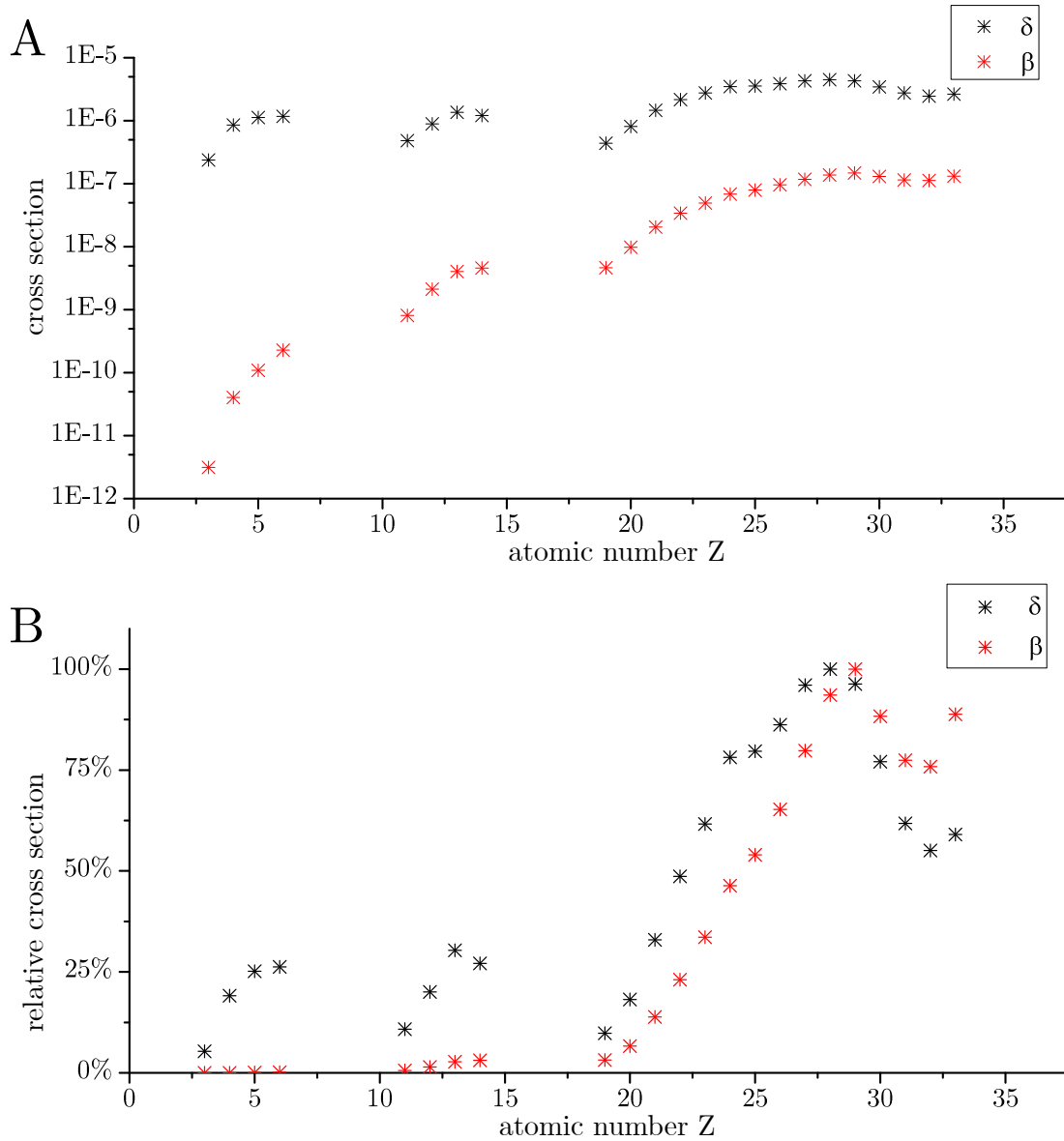
Figure 2.2: A: Plotted values of the attenuation and phase-shift cross section against the atomic number Z of the elements. The phase-shift cross section is on the order of $10^2 - 10^4$ larger than the attenuation cross section. The difference decreases with increasing Z.

B: The relative signal strength of the elements in percentage of the respective highest cross section (Z=28 for δ, Z=29 for β). For the phase-shift a notable signal from low-Z materials relative to the high-Z materials is expected, while the attenuation from the low-Z material is minimal, compared to the attenuation caused by the high-Z material. The plotted data was retrieved using the XOP-Toolkit [32] and correspond to an X-ray energy of 20 keV.

2.2 **Phase Contrast Techniques**

To exploit the phase-shift information of an object, several x-ray phase-contrast methods have been developed [6, 7]. The most prominent ones are the crystal interferometer (Bonse-Hart Interferometer) [35], the diffraction-enhanced imaging (DEI) [36, 37, 38], the propagation-based or in-line phase-contrast [11, 12, 13] and the grating interferometer [39, 40, 17], which all have been shown to be suitable to perform phase-contrast computed tomography [41, 42, 43, 44, 45]. In this section a short summary of those four different techniques will be given.

Crystal Interferometer

A typical crystal interferometer consists of three silicon crystals. The first crystal acts as beam-splitter, the second crystal is used to deflect the separated beams towards each other and the third crystal is placed at the meeting point of these two beams to recombine them before hitting the detector. By inserting a sample in one of the two beam branches after separation, phase shifts are induced to that beam, which will induce interference fringes on the detector. The crystal interferometer can achieve an extremely high sensitivity for the phase shift of the object. This high sensitivity makes the stability of the experiment a crucial parameter for the setup. In contrast to the other techniques this method gives the possibility to directly measure phase-shift. Due to the high sensitivity, the obtained projections in most cases demand for unwrapping of the obtained signal where the phase shift exceeds the limit of $\pm\pi$. To avoid too strong refraction at the border of the investigated sample, the measurements are usually performed within a liquid environment with its optical density similar to that of the object [41].

Diffraction Enhanced Imaging

Diffraction enhanced imaging exploits small variations in the refractive index of the sample, which leads to small refraction angles after the beam passing through the sample. By placing an analyser crystal behind the sample these refraction angles can be measured. The angular position of the analyser crystal requires a very precise alignment. Thus the diffraction enhanced method also demands for

a very high stability of the whole experimental setup, especially for the angular position of the crystal. The obtained projections are overlapping images of the attenuation contrast and the phase contrast. By comparison of two projections from both flanks of the rocking curve, the phase projection and the attenuation projection can be separated. The obtained phase image is the gradient of the refractive index distribution and therefore gives a differential phase-information.

Propagation-based Phase-contrast

The propagation-based phase-contrast or in-line phase-contrast is the most popular phase-contrast imaging method at synchrotron radiation facilities. It is by far the simplest method of the four techniques discussed here. As this technique only relies on a coherent x-ray source, the requirements for instrumentation are much lower then the other techniques. The visualization of phase-shifts is achieved by free-space propagation, with the detector being placed at a certain distance behind the sample. Main characteristic in the obtained projections is edge-enhancement. To separate attenuation and phase information of the projection from each other, several processing algorithms were developed [13]. However, all these algorithms rely on special assumptions made for the sample (e.g. $\mu = 0$). Up to now, no universal analytical method has been found and the results from the developed algorithms are highly depended on the actual sample. Another drawback is, that the phase retrieval from these projections will not give quantitative results, due to the approximations to the sample structure. In case where the investigated system is a binary system with a very low attenuation, this technique gives very good contrast to determine the morphology of the sample. Although the sensitivity to high spatial frequencies of electron density is very high, this technique lacks on sufficient sensitivity for continuous density-variations [46]. The spatial resolution of this technique is close to the resolution of an attenuation projection. A decrease in resolution comes with the smearing as reason of the propagation distance and the filter function of the phase retrieval algorithm.

Grating-based Phase-contrast

Main principle of the grating-based phase-contrast (gbDPC) method is to induce a periodic pattern to the beam profile. Relative changes in the phase-shift will induce small refraction angles which can be observed by measuring the lateral change of the previously induced pattern. Measuring the refraction angles of the sample results in a differential signal of the phase. A common interferometer at synchrotron facilities consists of a set of two gratings. The phase-grating is used to create the interference pattern, where the analyser grating is used to separate maxima and minima in front of the detector. In case where the interference pattern can be resolved directly by the detector, no analyser grating is needed. The grating interferometer is also applicable with low-coherent and polychromatic lab sources[17, 47]. Here, a third grating in front of the source acting as slit system to create an array of small sources with a larger spatial coherence is added to the interferometer.

Grating-based phase contrast has been proven to provide quantitative results. Dependent on the setup it can reach a very high sensitivity for small density variations [48]. The technique is capable of investigating samples demanding for a high dynamic range (e.g soft tissue with metal implants [49]). Due to the linearity of the obtained signal to the electron density of the sample (eq. 2.7), it allows for distinction of different low density materials even in the presence of high density material.

2.3 Grating-Based Phase-Contrast

As previously described, this differential phase-contrast technique relies on the detection of small refraction angles of the incoming X-ray beam caused by differences in the phase-shift induced by the object to the incoming wave. Main principle of this technique can be explained by the so-called Talbot-effect [50]. It describes the fact, that a periodic line pattern (grating) induced to the incident beam will repeat as a self-image after a certain distance namely the Talbot-distance. At fractions of this full Talbot-distance, modulations of the self-image can be observed[51]. The interference pattern itself is used as a carrier for the phase-shift information. It is used as a characteristic pattern of the beam-profile, which allows

to determine its position relative to an unchanged reference beam. This would not be possible with a homogeneous beam profile. The same principle can be found in similar techniques as the speckle-imaging [52, 53, 54] and the edge-illumination phase contrast [55, 56, 57]. The benefit of using a grating-based pattern instead of random speckles is a homogeneous distribution of the carrier modulation and a well pre-defined frequency and intensity. The precise properties of the grating also make it easier to choose between best configurations of energy, propagation distance and grating layout, while the performance of using a random object cannot be foreseen for different configurations. The speckle-based method in any case might be preferable onwards higher resolution x-ray microscopy [58] as for phase-contrast nano-tomography due to the challenges in production of gratings with an adequate period. The drawback of grating based-phase contrast is the limitation of the sensitivity to only one direction of phase-shift, due to the one-dimensional character of the interference pattern. The second dimension can be accessed using more complex grating structures (2-D gratings) and a stepping procedure in both directions [59, 60, 61], which come with the cost of additionally increased scanning time.

2.3.1 Differential phase shift and refraction

When an incoming X-ray beam with the wavelength λ passes through a sample of thickness d described by the complex refractive index

$$\underline{n} = 1 - \delta(\lambda) + i\beta(\lambda) \; , \tag{2.14}$$

with δ being the refractive index decrement and β the absorption index, the phase of the wave is shifted by (eq. 2.12)

$$\Delta\Phi = \frac{2\pi}{\lambda}\delta(\lambda)d \tag{2.15}$$

compared to a reference wave in vacuum. To describe the phenomenon of refraction due to the phase shift, the incoming wavefront is considered as a superposition of monochromatic plane waves. These waves are assumed to be in phase and parallel to each other. With an homogeneous wedge as sample we obtain a difference in the phase shift $\Delta\Phi$ between the sample positions x and $x + \Delta x$ perpendicular
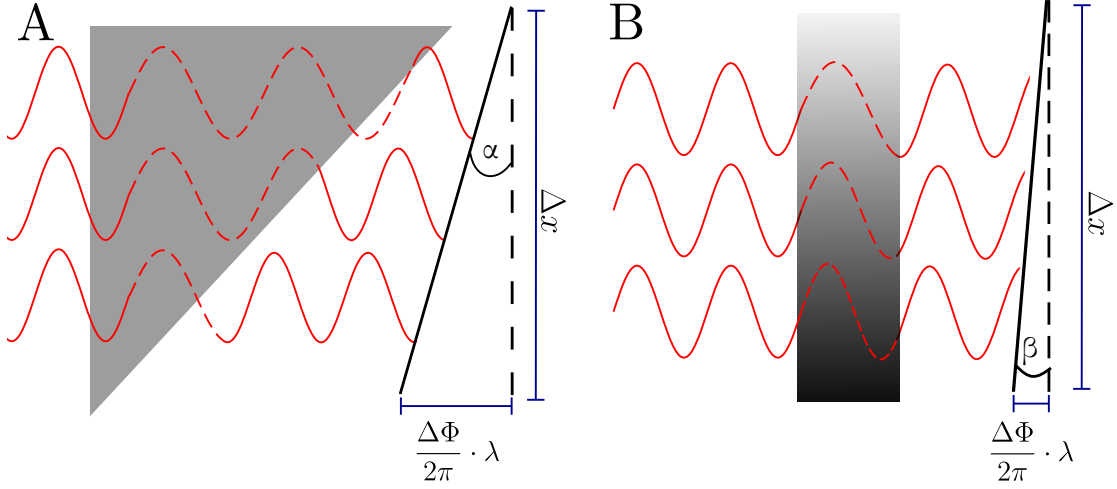
Figure 2.3: Schematic principle of refraction caused by an opaque object. After passing through the sample the outgoing wavefront is deflected by the angle α compared to the original wavefront. 'A' illustrates the refraction angle α due to a varying thickness of the sample. 'B' illustrate the refraction angle β due to a varying refractive index of sample (visualised by the grey-scale).

to the propagation axis z (Fig. 2.3). The wavefront behind the wedge is tilted at the angle α due to this phase shift:

$$\alpha(x) = tan\Big(\frac{\Delta\Phi(x)\lambda}{2\pi\Delta x}\Big) = tan\Big(\frac{\lambda}{2\pi}\frac{\partial\Phi(x)}{\partial x}\Big) \approx \frac{\lambda}{2\pi}\frac{\partial\Phi(x)}{\partial x} \ . \tag{2.16}$$

With the small angle approximation $tan(\alpha) \approx \alpha$, the refraction angle α is proportional to the wavelength of the incoming wave, and the gradient of the phase shift caused by the object. Analogous to an object with changing thickness a refraction angle is also caused by an object with varying density as illustrated in figure2.3B. Imaging methods, which are utilized to detect this gradient, are called differential phase-contrast imaging methods.

2.3.2 Talbot effect and phase grating

When illuminating a grating (grating bars impervious to light) with visible light, an image of the grating can be observed in regular distances downstream the grating [50]. This so-called *Talbot effect* appears for any periodic wavefront.
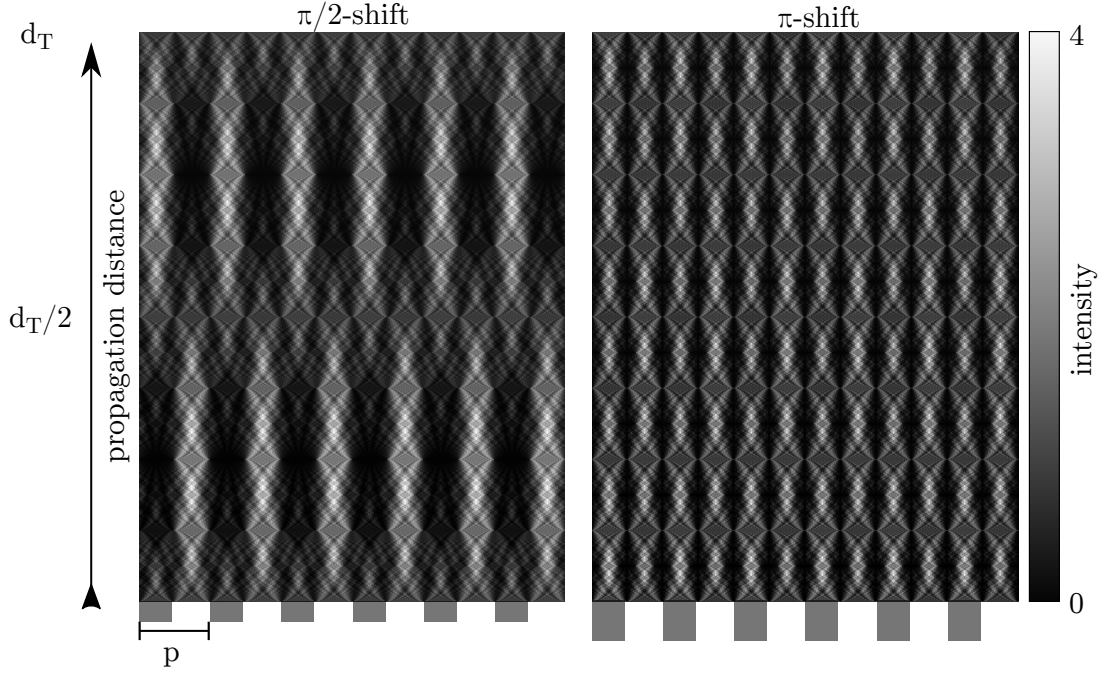
Figure 2.4: Monochromatic Talbot carpets for a $\pi/2$-shifting (left) and a π-shifting (right) phase grating. The fractional Talbot distances are $n \cdot d_T/16$ for a π-shifting grating and $n \cdot d_T/4$ for a $\pi/2$-shifting grating. At even fractional Talbot distances the incoming wavefront repeats itself. At odd fractional Talbot distances the periodic intensity pattern reaches its highest contrast. The lateral period of this pattern is $p/2$ for the π-shifting grating, whereas the period for a $\pi/2$-shifting grating is equal to to the grating period.

When using a grating with period p to create a periodic wavefront, the distance where this wavefront repeats itself is given by the Talbot distance

$$d_T = \frac{2p^2}{\lambda} \ , \tag{2.17}$$

where λ is the wavelength of the light.

The following will consider a plane wavefront ($A_0(x,y) = const.$) and a pure phase grating, which means that no absorption takes place but a phase shift $\Delta\phi(x,y)$ is caused by the grating bars. Since there is no absorption within the grating bars, the wavefront A'_0 directly behind the phase grating and the one A'_{d_T} appearing at

the Talbot distance yield an homogeneous intensity distribution:

$$A'_{d_T}(x,y) = A'_0(x,y) = A_0(x,y)e^{-i\Delta\phi(x,y)} \tag{2.18}$$

$$\Rightarrow I'_{d_T}(x,y) = |A_0(x,y)e^{-i\Delta\phi(x,y)}|^2 = |A_0(x,y)|^2 = const. \tag{2.19}$$

However, at certain periodic distances behind the grating, different intensity patterns can be observed [62]. These distances depend on the wavelength λ, the induced phase shift $\Delta\phi$, the grating period p and the duty cycle of the grating. The duty cycle of a grating is defined as the ratio of grating bar width and period of the grating.

Most setups are equipped with a phase grating either inducing a phase shift of π or $\pi/2$ and having a duty cycle of 0.5. Figure 2.4 illustrates the simulated intensity pattern behind such gratings along the propagation axis z.

These so-called Talbot carpets show that periodic intensity patterns can be observed at fractions of the full Talbot distances

$$d_n(\pi) = \frac{n}{16}d_T = n\frac{p^2}{8\lambda} \tag{2.20}$$

$$d_n(\pi/2) = \frac{n}{4}d_T = n\frac{p^2}{2\lambda} \ , \tag{2.21}$$

where n is an odd integer. These patterns have a lateral period of $p/2$ in case of a π-shifting phase grating and a period of p for a $\pi/2$-shifting grating. At the fractional Talbot distances where n is an even integer, no intensity variation is observable. The observable intensity patterns at odd fractional Talbot distances behind a π-shifting grating are all identical, whereas the intensity patterns at the $1st$ and $3rd$ fractional Talbot distance behind a $\pi/2$-shifting grating are shifted half a period against each other.

2.3.3 Single- and Double-Grating Interferometer

The intensity pattern created by the phase grating can be used to detect the refraction of an incoming beam introduced by the object. The angular deviation α (eq. 2.16) of the beam direction can be observed by a lateral shift

$$S(x) = \alpha(x)d = \frac{\lambda}{2\pi}\frac{\partial\Phi(x)}{\partial x}d \tag{2.22}$$

of the intensity pattern, where d is the propagation distance, x is the lateral position, and λ is the wavelength of the X-ray beam. Therefore the differential phase shift $\partial\Phi(x)/\partial x$ induced by the object can be determined by comparing the detected intensity pattern with and without the object as a reference pattern.

For an interferometer setup, where the interference pattern can be directly resolved by the detector system (p is at least 3-4 times larger then the pixel size), no additional component is needed. Such a setup is called single-grating interferometer it relies on a very high resolving camera system and a small point spread function of the optical system.

For the most common setup at synchrotron radiation facilities, the phase grating period is close to or smaller than the effective pixel size of the detector. In this case a second grating, the so-called analyser grating, has to be placed in front of the detector. The analyser grating is an absorption grating and acts as an aperture to differentiate between maxima and minima of the interference pattern. For a parallel X-ray beam, the period of the analyser grating p_2 has to be equal to the period of the intensity pattern. With $p_2(\pi) = p/2$ and $p_2(\pi/2) = p$ we can rewrite equation 2.20 and 2.21 to

$$d_n = n \frac{p_2^2}{2\lambda} \ .$$

(2.23)

With the second grating, the intensity measured by the detector is dependent on the lateral position of the analyser grating relative to the intensity pattern [39, 40]. For both setups, either single- or double-grating, the intensity is recorded for a series of different grating positions. This procedure is called phase-stepping method. The following section explains how exactly the differential phase shift caused by the object is retrieved from the measured intensities.

2.3.4 Phase Retrieval

Stepping Approach

When using the phase-stepping approach, several images for different lateral positions of one of the phase gratings are recorded to resolve the intensity pattern. The measured intensity in each pixel oscillates between a maximum I_{max} and a minimum I_{min}, depending on the grating position perpendicular to the beam
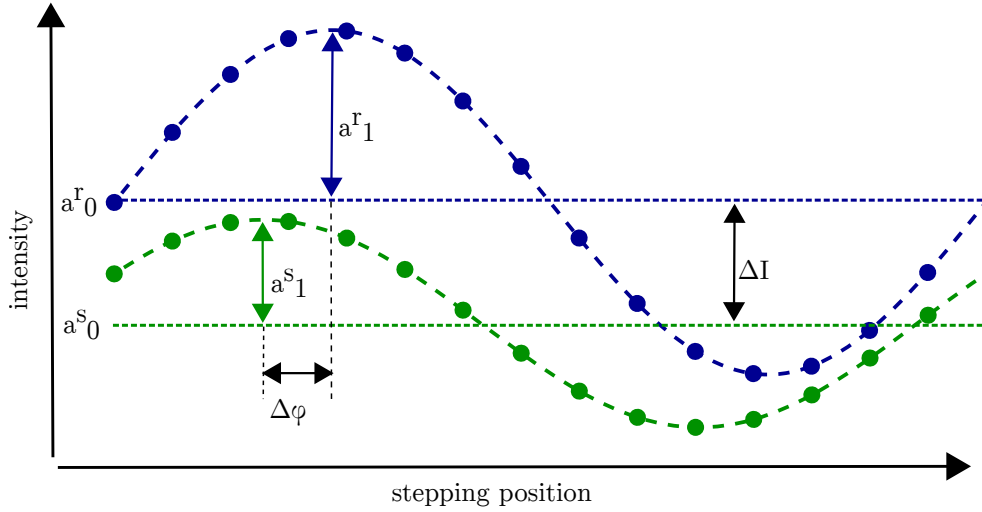
Figure 2.5: Stepping curves for a reference scan (blue solid line) and a sample scan (green dashed line). From the stepping curves the mean intensity a_0, the amplitude a_1 and the displacement φ can be determined.

direction. A sinusoidal curve can be fitted to the measured intensities for each pixel (x_i, y_j). The fitted intensity curves, the so-called stepping curves, for the measurement with sample $I^s(x_i, y_j)$ and without sample $I^r(x_i, y_j)$ can be compared to determine the differential phase shift caused by the object (Fig. 2.5). Here, the intensity curve without object serves as a reference [40].

For each curve we can identify several properties with $i=r$ for the values characterising the reference scan and $i=s$ for the sample scan:

a_0^i: is the mean value of the intensity.
a_1^i: is the amplitude of the sinusoidal fitting curve.
φ^i: is the phase offset of the sinusoidal fitting curve.
V^i: is the ratio of amplitude a_1^i to mean intensity a_0^i, called visibility.

If the stepping distance is chosen to be a multiple of the grating period, then the recorded intensity curve is a periodic function of the stepping position x:

$$f(x) = a_0^i + a_1^i \sin(\omega x + \varphi^i) \ , \tag{2.24}$$

with $\omega = 2\pi/p_2$.

All parameters mentioned above can be determined from this function via Fourier analysis. From the comparison of these values for the two intensity curves three different signals can be determined: the attenuation, the differential phase shift, and the visibility. In order to derive the three parameters in equation 2.24, a stepping series has to consist of at least three different grating positions.

The X-ray beam attenuation $\mathcal{A}$ of the object is defined by the Beer-Lambert law as:

$$\mathcal{A}(x_i, y_j) = -\log \frac{a_0^s(x_i, y_j)}{a_0^r(x_i, y_j)} \; . \tag{2.25}$$

The differential phase shift can be determined from the displacement $\varphi(x_i, y_j)$ of the curves relative to each other.

$$\varphi(x_i, y_j) = \varphi^s(x_i, y_j) - \varphi^r(x_i, y_j) \tag{2.26}$$

The observed displacement $\varphi(x_i, y_j)$ is related to the lateral shift of the intensity pattern $S(x_i, y_j)$ by

$$S(x_i, y_j) = \frac{p_2 \varphi(x_i, y_j)}{2\pi} \; . \tag{2.27}$$

This relation and the equations 2.22 and 2.23 can be used to determine the differential phase shift

$$\frac{\partial \Phi(x_i, y_j)}{\partial x} = \frac{2\pi S(x_i, y_j)}{\lambda d} = \frac{p_2 \varphi(x_i, y_j)}{\lambda d} = \frac{2\varphi(x_i, y_j)}{n p_2} \; . \tag{2.28}$$

The third signal, the visibility, can be used to derive so-called dark-field signal, it is defined as the ratio V^s/V^r between the visibility of the sample scan V^s and the visibility of the reference scan V^r. This signal can be used as additional imaging modality [63] and has been investigated in detail [64, 65]. Within this thesis the main focus is on the phase signal. Therefore the dark-field signal will not be further discussed. However, visibility is a key parameter to judge the performance of a grating interferometer and an important value for grating quality control. A higher visibility provides a better sinusoidal fit, which in turn gives a higher accuracy of the obtained data.

Single-Shot Approach

When a detector system has a high spatial resolution, which is capable to resolve the interference pattern directly, then it is also possible to analyse the refraction angles without recording a full stepping series. The so-called single-shot approach is based on analysing spatial harmonics in the image. The interference pattern is recorded as a periodic pattern of dark and bright stripes in the detector plane. The Fourier transform of this pattern consists of a number of discrete peaks corresponding to the interference pattern frequency and its harmonics. By separating the spatial harmonics, the obtained signals can be extracted into images, which then contain either the absorption or the phase-information [66, 67]. The nth-order spatial harmonic image is defined as the inverse Fourier transform on the interval $\left[\frac{2\pi n}{p} - \pi/p \ , \ \frac{2\pi n}{p} + \frac{\pi}{p} \right]$ as

$$h_n = (x) = exp\left(\frac{i2\pi n x}{p} \right) \cdot \int dk_x \cdot exp(i2\pi k_z \cdot x) \cdot \tilde{I}(k_z), \qquad (2.29)$$

where $\tilde{I}(kx) = (F)(I(x))$ represents the Fourier transform of the intensity I(x). The different harmonic images h_n carry information analogues to the Fourier series terms when using the stepping approach:

$$h_0 \sim a_0 \qquad (2.30)$$

$$h_1 \sim a_1 \cdot exp(i\phi) \qquad (2.31)$$

This approach benefits from a short acquisition time as only one image has to be taken instead of a whole stepping series. Together with the absence of an analyser grating, this extremely reduces the radiation dose. The disadvantage on the other hand is the reduced spatial resolution which is limited by the frequency of the interference pattern. Due to the limited resolution of the single-shot approach, this method was not further considered.
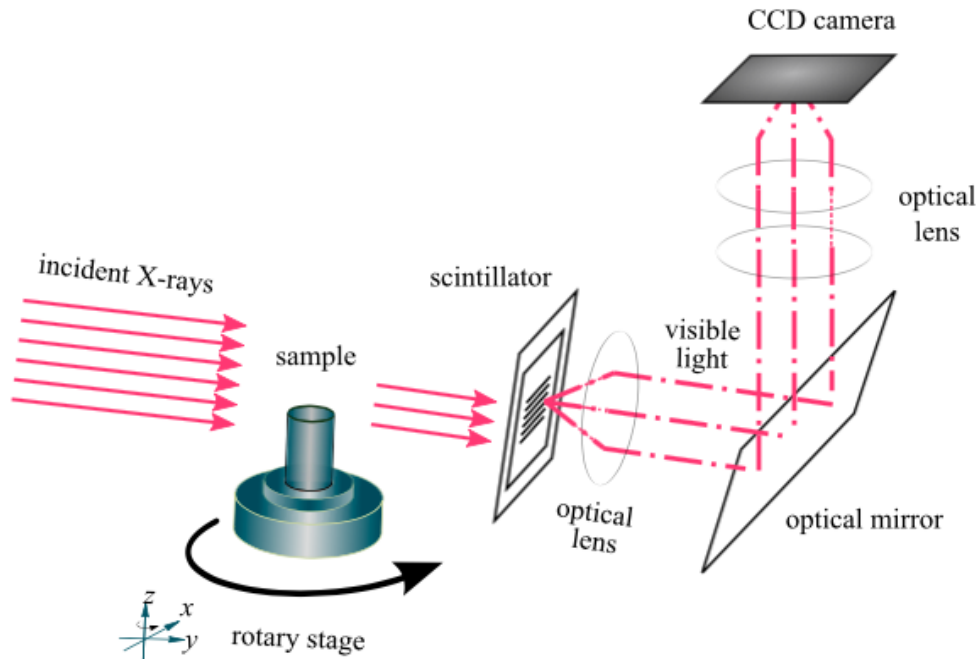
Figure 2.6: A typical micro-tomography setup at a synchrotron radiation facility consists of a high precision rotation axes and a high resolution X-ray detector system. For this purpose usually a scintillator crystal is coupled to a CCD- or CMOS-based camera via a microscope optics.

2.4 The Principle of SRμCT

At a storage ring, charged particles (electrons or positrons) close to the speed of light are kept on a circular trajectory. Synchrotron radiation is produced when these charged particles are accelerated [1] for example using a megnetic field. Due to relativistic effects the accelerated particles emit highly collimated radiation [68] in the direction tangential to their circular orbit [69]. The X- rays produced by the synchrotron radiation source can be 10^{12} times brighter than those from conventional tube sources [68]. The acceleration of the particles takes place at straight sections in the storage ring by use of insertion devices (undulator or wiggler) [70]. These devices consist of an array of magnets, which forces the particles on an oscillating path [30, 71].

Following the insertion device in beam radiation direction a variety of optical

components such as monochromators [72], and focusing mirrors or lenses [73] are installed to obtain the wanted X-ray beam properties.

A simplified synchrotron-radiation based micro computed tomography ($SR\mu CT$) experiment consists of a rotating sample stage, and an X-ray detector to acquire projections of the sample covering 180° of rotation. For high spatial resolution applications the detector system usually consists of a scintillation crystal to convert the x-rays to visible light and a CCD- or CMOS-based camera coupled via some magnifying optics. To avoid image disturbance from propagation effects, the detector system is placed as close as possible behind the sample. For grating-based phase-contrast, this setup has to be extended by one or two gratings and a suitable propagation distance between the sample and detector. Figure 2.6 illustrates a typical $SR\mu CT$-setup.

Synchrotron radiation based micro computerized tomography was first introduced by Bonse et al. [74, 1] and Flannery et al. [75] in the 1980s. With the availability of large synchrotron radiation facilities and further development, $SR\mu CT$ became a well established 3-D imaging method for high spatial- and density-resolution [71, 68].

The highly intense and parallel beam is a valuable feature for a short scan duration and easy reconstruction afterwards. The tunable energy range of synchrotron radiation allows to choose a feasible energy for different samples to maximize the image contrast at a minimum of artefacsts [69].

2.5 Image Processing

The processing of the projections I_P consists of a so-called flat field correction plus the phase-retrieval in case of phase-contrast data. For the flat field correction, the images have to be corrected for the intensity of the X-ray beam, the dark current of the camera and the beam profile of the x-ray beam.

The **dark current** of a camera can be treated as a constant offset of the pixel counts that can be dependent on the applied exposure time. At the beginning or end of each scan a dark image without illumination is taken with the same exposure time as for the projections. This dark image I_D has to be subtracted from

every frame taken during the experiment to get rid of this offset from the dark current. For cooled camera sensors the effect of dark current becomes negligible. Nevertheless the dark image also gives valuable information about hot pixels and stuck pixels.

The **beam intensity** of the X-rays may vary during the experiment. A simple reason for a varying beam intensity is the constant loss of particles in the storage ring. Dependent on the frequency of refilling the storage ring this causes typically a intensity variation between 1% and 20%. With knowledge of the beam current BC within the storage ring every image can be calibrated according to the specific beam current.

The **beam profile** is not completely homogeneous. Therefore a reference profile for an adequate calibration is necessary. For a perfectly stable beam profile one reference image I_R without sample would be enough to take care of this. For a real experiment a series of references is taken before and/or at the end or even regularly during data acquisition to take care of small fluctuations in the beam profile. Either the mean of those references or a single best fitting one can be used for calibration by division of the projection by the reference.

The flat-field corrected image is then given as:

$$I = \frac{I_P - I_D}{I_R - I_D} \cdot \frac{BC_R}{BC_P} \qquad (2.32)$$

For differential phase contrast data obtained from a grating interferometer, the image preprocessing before phase retrieval is similar to the processing for attenuation-contrast data. The correction for dark current and beam intensity are performed the same way on every single image of a stepping series. The correction for the beam profile is replaced by the calibration with a reference stepping series to take care of the pixel dependent phase offset in the projection data. This calibration with the reference scan takes place after the phase retrieval (sec. 2.3.4) for projection and reference data.

2.6 Tomographic Reconstruction

Computed tomography relies on a series of projections of a sample from different rotation angles. To describe a complete tomogram the projections have to cover a sample rotation of 180°. To reconstruct a three dimensional representation of the sample out of the two dimensional projections, different reconstructing strategies can be used. Here only the principle of filtered back projection will be explained. Due to the parallel beam every horizontal slice of the object can be reconstructed separately. For this reason we will only consider one line of each projection, according to the chosen slice. All these single lines represent the line integral through the 2D-object $f(x, y)$ under a certain angle θ. The projections are given by:

$$p(r, \theta) = \int \mu(x, y)ds = -\log(I) \tag{2.33}$$

In the coordinate system of the object r can be parametrized dependent on θ

$$r = x \cos \theta + y \sin \theta \tag{2.34}$$

and equation 2.33 can be rewritten as:

$$p(r, \theta) = \int\limits_{-\infty}^{\infty} \int\limits_{-\infty}^{\infty} \mu(x, y)\delta(x \cos \theta + y \sin \theta - r)dx \; dy \tag{2.35}$$

This function is known as the *Radon transform* of $f(x, y)$ and commonly called sinogram. To reconstruct the object from the sinogram the *filtered backprojection* (see Appendix: B)

$$f_{FB}(x, y) = \int\limits_{0}^{\pi} p'(x \cos \theta + y \sin \theta, \theta)d\theta \tag{2.36}$$

is used with p' as filtered projection profile.

The algorithm for filtered backprojection cannot be applied on data obtained by grating-based phase contrast in this form. Due to the differential character of the projections

$$p_{DPC}(r, \theta) = \frac{d}{dr} \int \delta(x, y)ds \tag{2.37}$$

the filter function has to be replaced by an imaginary filter [76]

$$\mathcal{B}_{\mathcal{DPC}}(\nu) = \frac{1}{2\pi i} sign(\nu) \; . \tag{2.38}$$

Another possibility which allows to avoid the imaginary filter is to integrate the obtained projections, representing the line integral of δ through the sample:

$$p_\delta(r,\theta) = \int p_{DPC}(r,\theta)dr = \int \delta(x,y)ds \; . \tag{2.39}$$

By doing so, the same algorithms and filter functions as for attenuation-based data can be used for reconstruction.

3 Simulations

This chapter deals with simulations to investigate the performance of a single-grating interferometer dependent on the key parameters *propagation distance* and *grating period*. The performance evaluation of the simulations is based on the key features, namely *visibility, sensitivity and spatial resolution*. As comparison to the single-grating setups a two-grating setup in a state-of-the-art configuration was chosen as reference. Most simulations and the preliminary considerations were carried out for a single-grating interferometer with a period of 10 μm and a double-grating interferometer with a phase-grating period of 4.8 μm and an analyser-grating period of 2.4μm to coincide with the experimental part (sec. 5) of this work.

3.1 Preliminary Considerations

3.1.1 Sensitivity

Sensitivity is a key factor of the performance of an interferometer. It describes the possibility to distinguish between materials with regard to their investigated property. The sensitivity S of grating based-phase contrast is usually defined by

Table 3.1: Horizontal source size σ_x and source distance z for the two tomography endstations, and the optimal propagation distances d_{opt} for highest sensitivity.

Beamline	σ_x	z	d_{opt} $(p_1 = 10 \ \mu m)$	d_{opt} $(p_1 = 2.4 \ \mu m)$
IBL	35 μm	85 m	9.7 m	2.3 m
HEMS	35 μm	97 m	11.1 m	2.7 m

the strength of the measured signal ϕ for a correspondend refraction angle α. [77]

$$S := \frac{\phi}{\alpha}. \tag{3.1}$$

To distinguish two signals they have to differ by at least by the uncertainty of the measurement. The minimum detectable refraction angle can be defined with the standard deviation of the measurement $\Delta\phi$ as this uncertainty as [78]:

$$\alpha_{min} = \frac{p_2}{2\pi d}\Delta\phi \tag{3.2}$$

According to Modgregger et al. [78], the sensitivity of a interferometer is related to the reduced inter-grating distance

$$\eta = \frac{\sigma d}{zp_2}, \tag{3.3}$$

where σ is the source size, d is the inter-grating distance, z is the distance from the source to the phase grating and p_2 is the period of the analyser grating. For a single grating interferometer, the analyser grating period p_2 is replaced by the interference pattern period that is equal to p_1 for a $\pi/2$-shift setup, respectively $p_1/2$ in case of a π-shift setup. For the maximum sensitivity the parameters have to be chosen to reach a reduced inter-grating distance of 0.4 independent on the actual setup (according to [78]). Knowing the characteristics of the beamline where the interferometer is going to be installed the optimal inter-grating distance d_{opt} regarding the sensitivity can be calculated. Table 3.1 lists the parameters for the PETRA III beamlines P05 and P07 and the resulting optimal inter-grating distance.

Due to the small source size of PETRA III ($\sigma_x \approx 35\ \mu m$, $\sigma_y \approx 6\ \mu m$), the optimal inter-grating distances already reach several meters for typical grating periods in the range of 2 μm and 10 μm. For a single-grating setup with 10 μm period the optimal distance would already be close to 10 m. Even for a phase grating with a period of 2.4 μm the optimal distance is more then 2 m. These distances are extremely large and can be barely achieved at the experiment. Especially, when placing the phase grating close to the sample the available inter-grating distance or grating to detector distance is limited to roughly 1.5 m for both tomography

Table 3.2: Lateral separation of diffracted X-ray beam at the maximum possible propagation distance. The given relative distances correspond to the propagation distance for energies of 10 keV and 70 keV.

grating period [μm]	rel. distance ξ	beam separation [μm]
4.8	9/16	10.8
4.8	56/16	67.2
10	1/4	10
10	3/4	30

endstations (sec. 4.2). From this we can conclude that the sensitivity for the given experimental conditions at both beamlines will be best for the largest available propagation distance. These consideration of the sensitivity assume that the interferometer is set up at an odd fractional Talbot distance (eq. 2.23) to benefit from the maximum visibility. Restricting the propagation distance to odd fractional Talbot distances results to Talbot orders between the $56th$ order (150.8 cm) at 10 keV and the $9th$ order (146.3 cm) at 70 keV for the double-grating interferometer with highest sensitivity. For the single-grating interferometer the highest sensitivity is achieved at propagation distances between the $3rd$ order (121 cm) at 10 keV and $1st$ order (149.2 cm) at 37 keV. For energies higher then 37 keV no odd fractional Talbot distances can be reached. This perspective does not take into account the dependency of the resolution from the inter-grating distance. It will turn out that the propagation distance has a huge impact on the reachable resolution. The following section will discuss the impact of the propagation distance on the spatial resolution.

3.1.2 Spatial Resolution

As the phase grating of the interferometer acts as a beam splitter, the characteristics of the setup, in particular grating period and inter-grating distance, already define a certain doubling of the given images [40]. Using a high resolution detector with a pixel size in the range of only a few micrometer, the beam separation is detectable and cannot be neglected as it is the case for lab sources with large pixel

sizes ($\sim 100~\mu m$). The beam separation caused by the grating is defined by the diffraction equation:

$$m\lambda = p_1 \sin\alpha \ . \tag{3.4}$$

Here, m represents the diffraction order, λ is the wavelength of the incident X-ray beam, p_1 is the phase-grating period and α is the diffraction angle. The relative intensity, also called diffraction efficiency, of the diffraction orders for a rectangular grating with a duty cycle of 0.5 is given by [79]

$$I_m = 0 \qquad\qquad\qquad m = 0, even \tag{3.5}$$

$$I_m = (2/\pi m)^2 \qquad\qquad\qquad m = odd \ . \tag{3.6}$$

The first diffraction order accounts for more than 80% of the beam intensity. Thus, only the first diffraction order $m = \pm 1$ is applied here.

For small diffraction angles ($\sin\alpha \approx \alpha$) and a given propagation distance, the beam separation Δs is described by:

$$\Delta s = 2\frac{d\lambda}{p_1} \ . \tag{3.7}$$

Replacing d by its ratio to the Talbot distance

$$\xi = \frac{d}{d_T} = \frac{d\lambda}{2p_1^2} \tag{3.8}$$

as *relative distance*, the beam separation can be rewritten independent of the energy.

$$\Delta s = 2\frac{\xi d_T \lambda}{p_1} = 4\xi p_1. \tag{3.9}$$

Thus the beam separation can be defined by the relative distance. Table 3.2 list some values of the beam separation with respect to the maximum propagation distance for energies between 10 keV and 70 keV.

The calculated values for the beam separation at the highest reachable sensitivity are already very large compared to the effective pixel sizes in modern $SR\text{-}\mu CT$ experiments, which typically range from less then 1 μm to 5 μm [80, 81]. For the purpose of a high-resolution phase-contrast setup, the aim is to achieve a spatial resolution in the range of $\approx 5~\mu m$ to bridge the gap between the resolution of

lab based phase-contrast setups and highest resolution phase-contrast methods (e.g propagation based, ptychography, CDI). As a consequence the propagation distance has to be shortened to ensure a beam separation, which does not exceed $5 \ \mu m$. This requires the condition

$$\xi \leq \frac{5\mu m}{4p_1} \ .$$
(3.10)

For the two given phase-grating periods the threshold *relative distances* are 0.26 ($p_1 = 4.8 \ \mu m$) and 0.125 ($p_1 = 10 \ \mu m$). Assigned to the fractional Talbot distances the interferometer using a 4.8 μm-pitch grating inducing a π-shift is limited to *3rd*-fractional Talbot distance. For the 10 μm-pitch grating the limit is even at only half the first fractional Talbot distance.

3.2 Simulation Method

Two main assumptions were used in this simulation work.

1. All gratings are perfectly fabricated (no artefacts) and infinitesimal thin.
2. The incoming wave is represented by a plane wave function.

Thus the gratings can be described by one-dimensional step-functions and the wavefront is modulated according to it before it is propagated. The evolution of the electric field U along the beam direction thus can be expressed by using free space propagation based on the *Fresnel diffraction integral* (sec. C).

The coordinate system for all simulations is defined with the x-axis being horizontally perpendicular to the beam direction, the y-axis vertically perpendicular to the beam direction and the z-axis along the beam direction.

3.2.1 Phase-Grating

The phase grating $g(x, y)$ with a structure height h can be described as a rectangular function:

$$g(x, y) = \begin{cases} h & \text{if } x \bmod p_1 < dc \cdot p_1 \\ 0 & \text{if } x \bmod p_1 \geq dc \cdot p_1 \ , \end{cases}$$
(3.11)

where h_1 is the height of the grating structures, p_1 the period of the grating and d_c is the duty cycle defined as the ratio of lamella-width to period. Based on this function the incoming planar wavefront $U_0(x, y)$ is modulated by the phase-shift and attenuation of the phase grating induced by the grating material.

$$U_{G1}(x, y) = U_0(x, y) \cdot e^{-\frac{2\pi}{\lambda}(i\delta_g + \beta_g)g(x,y)} \tag{3.12}$$

then gives the distorted wavefront behind the phase grating, where δ_g denotes the refractive index decrement and β_g the imaginary part of the refractive index for the grating material.

3.2.2 Object

The sample object $\mathcal{O}(\vec{r}) = \delta(\vec{r}) + i\beta(\vec{r})$ is a matrix, where δ and β are the correspondent refractive index components of the material. The influence of this sample on the wavefront is taken into account in a similar way as the grating by neglecting the width of the object. To represent the sample as a flat object we calculate the line integral along the beam path γ to receive the effective phase-shift and attenuation coefficients $\Delta\phi$ and α of the object $\mathcal{O}$ for the projection angle θ:

$$\Delta\phi(x, y, \theta) + i\alpha(x, y, \theta) = \int_\gamma \mathcal{O}(\vec{r}) \, d\gamma \tag{3.13}$$

An easy procedure to obtain the effective phase-shift and attenuation coefficient for every projection angle ϑ, is to utilise the Radon transform $\mathcal{R}$ of the object:

$$\mathcal{R}(\mathcal{O})(x, y, \vartheta) = \int \mathcal{O}(x\cos\vartheta + z\sin\vartheta, y, x\sin\vartheta - z\cos\vartheta) \, dz \,. \tag{3.14}$$

As a result, a specific projection angle ϑ the effective phase-shift and attenuation coefficients are given as $\Delta\phi(x, y) + i\alpha(x, y) = \mathcal{R}\mathcal{O}(x, \vartheta)$. Applying this to the incoming wavefront $U_{G1}(x, y)$ that was already modulated by the phase grating, the outgoing wavefront is given by

$$U_{\mathcal{O}}(x, y) = U_{G1}(x, y) \cdot e^{-\frac{i2\pi}{\lambda}\Delta\phi} \cdot e^{-\frac{2\pi}{\lambda}\alpha} \,. \tag{3.15}$$

Table 3.3: List of the simulated setups and their key parameters grating period p_1, effective pixel size s and Talbot distance at 20 keV.

Setup	$p_1 [\mu m]$	$s \ [\mu m]$	$d_T \ (20 \ keV) \ [m]$
$SG_{4.8}$	4.8	1.2	0.743
SG_7	7.0	1.2	1.581
SG_{10}	10.0	2.4	3.226
DG	4.8	2.4	0.742

Together with the modulation caused by the grating the simulated projection $U_P(x,y)$ and the simulated flatfield $U_F(x,y)$ at the propagation distance z are given by

$$
\begin{aligned}
U_P(x,y) &= \mathcal{F}^{-1}\left\{\mathcal{F}\left\{U_0(x,y)e^{-\frac{2\pi}{\lambda}(i\delta_g+\beta_g)g(x))}e^{-\frac{2\pi}{\lambda}(i\Delta\phi+\alpha)}\right\}e^{i\pi\lambda z\nu^2}\right\} \\
U_F(x,y) &= \mathcal{F}^{-1}\left\{\mathcal{F}\left\{U_0(x,y)e^{-\frac{2\pi}{\lambda}(i\delta_g+\beta_g)g(x))}\right\}\cdot e^{i\pi\lambda z\nu^2}\right\},
\end{aligned}
\tag{3.16}
$$

with $\nu = \sqrt{\nu_x^2 + \nu_y^2}$ as the spatial frequency. This equation utilized the Fresnel diffraction integral. The resulting intensity pattern at the detector plane is finally given as:

$$
I_z(x,y) = |U_{P/F}(x,y)|^2.
\tag{3.17}
$$

3.3 Simulation Results

3.3.1 Projections

For the analysis of simulated projections four different single-grating setups were investigated and compared to a state-of-the-art double-grating interferometer.

Table 3.3 lists the tested setups with phase grating period p_1 and effective pixel size s.

All the projection simulations were carried out for an X-ray energy of 20 keV. For each projection a stepping series of four images was taken and analysed as described in section 2.3.4.

As object for the projections a virtual test pattern consisting of various double wedges etched into a silicon substrate was used. The wedges were sized from
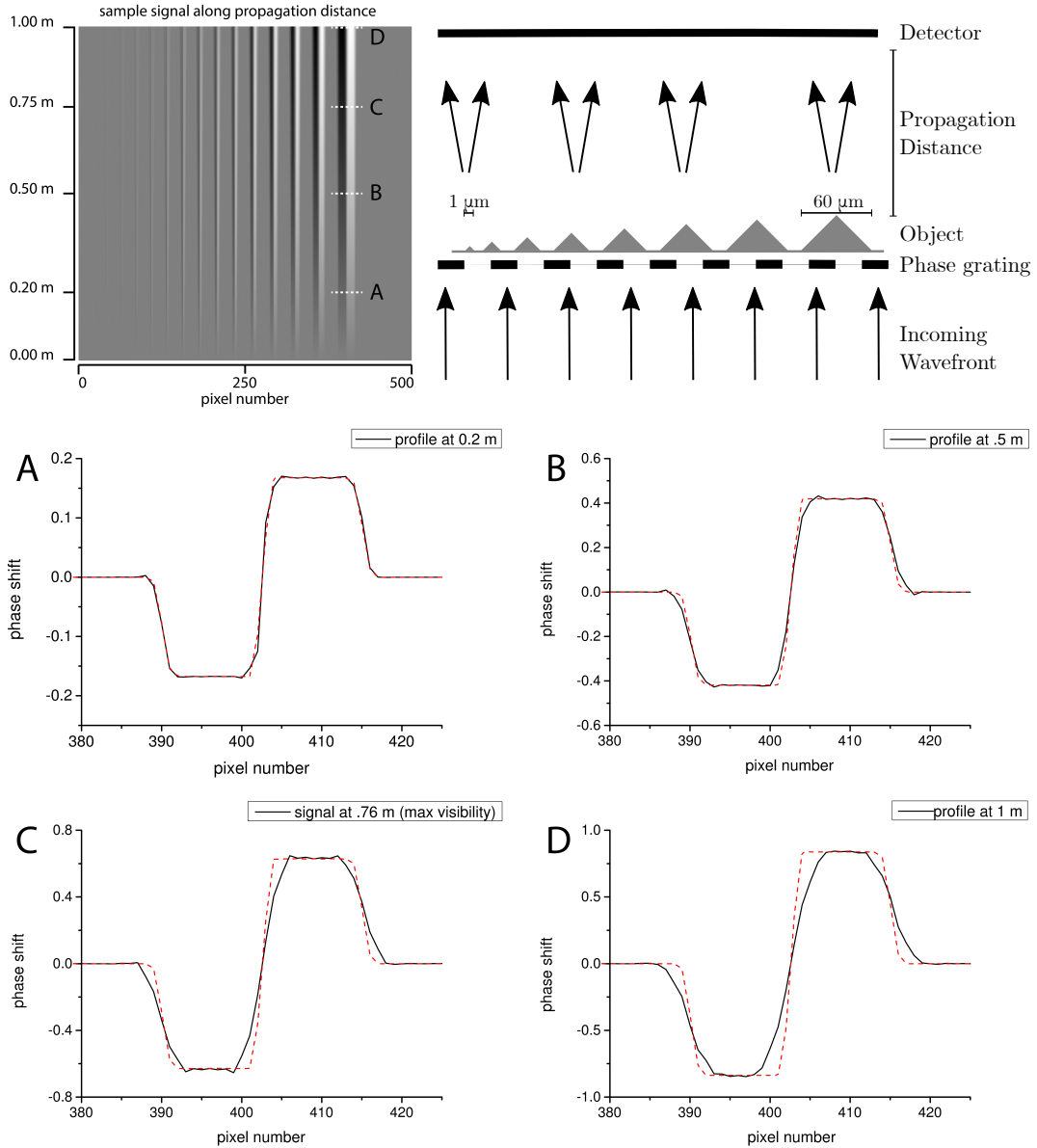
Figure 3.1: The image shows the simulated projected profile of the test sample along the propagation distance. The test sample consists of several Silicon bars with a squared cross-section sized between 1 μm and 60 μm (diagonal). The phase-projection was retrieved from a stepping-scan with 5 steps and with a grating period of 10 μm. Structures below 5 μm are detectable. The plotted profiles of the largest rod at different distances (A, B, C, D) show significant blurring of the edges already at the 1st fractional Talbot distance (C). At short distances (A, B) the projected profile is in very good agreement with the expected signal (red dashed curve).
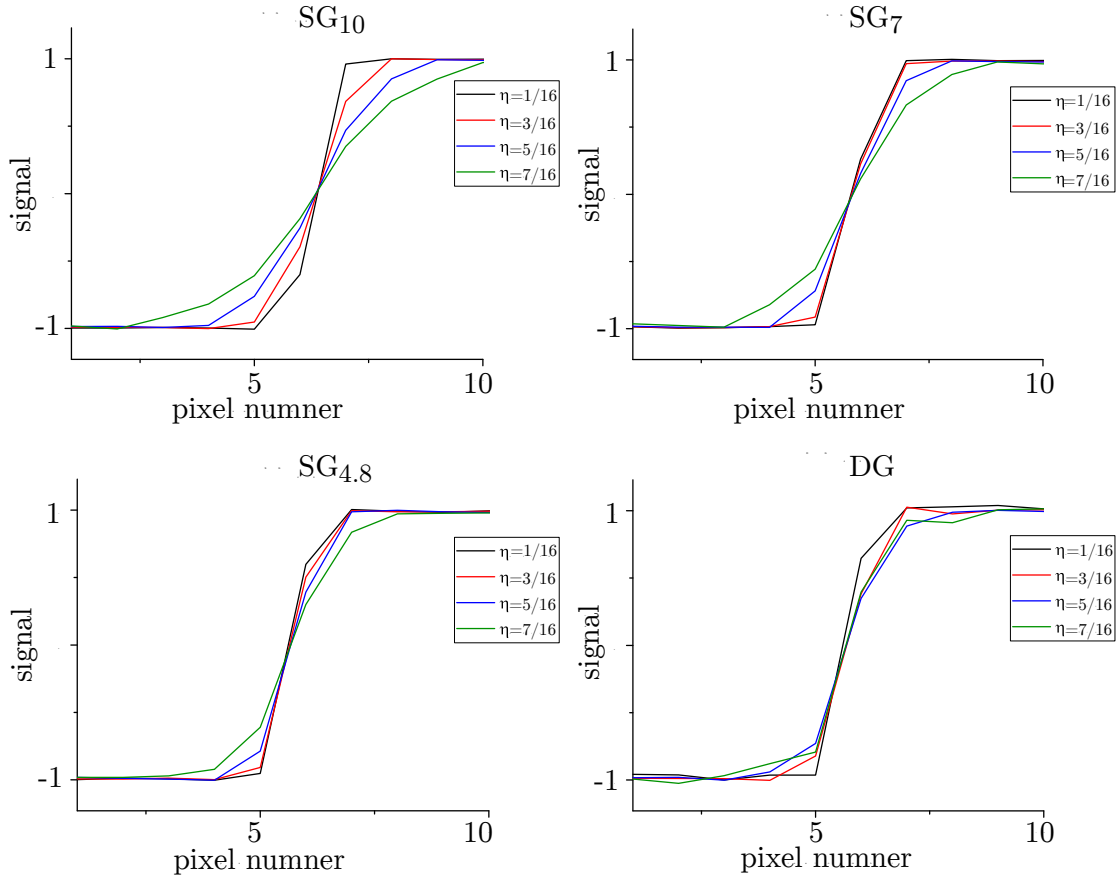
Figure 3.2: The image shows the obtained signal from different setups at varying distances. For the shortest distance all setups show a similar blurring. With increasing relative distance η the blurring increases stronger with larger grating periods.

$1~\mu m$ to $60~\mu m$. For each of the tested single-grating setups projections were simulated for the whole propagation distance range up to the full Talbot distance. Figure 3.1 gives an example of the retrieved projections for the SG_{10} setup up to the first fractional Talbot distance. The edges of the wedges show a blurring that dramatically increases with the growing propagation distance. To compare the effect of blurring for the different setup types, the retrieved line profiles of the projections are compared at different propagation distances. The obtained signals plotted in figure 3.2 represent the transition area of the double wedge from decreasing to increasing object thickness. All signals were normalised to the range of -1 to 1 for a better direct comparison. The four compared propagation

Table 3.4: Sensitivity comparison for the four different setups at the critical distance d_c and the corresponding visibility value dependent on the simulated point spread function.

PSF	**Setup**	d_c $[d/d_T]$	*visibility* [%]	*sensitivity* [arb.]
0.1 p_1	$SG_{4.8}$	0.26	92	1.96
	SG_7	0.178	90	1.91
	SG_{10}	0.125	69	1.46
	DG	0.26	78	1.69
1 μm	$SG_{4.8}$	0.26	48	1.02
	SG_7	0.178	73	1.56
	SG_{10}	0.125	69	1.46
	DG	0.26	73	1.67

distances were chosen equidistant within half of the full Talbot distance.

In the ideal case the obtained signal would jump from -1 to 1 at the transition point, resulting in a recorded step function. However, the projections show that a significant blurring of the step function occurs, dependent on the propagation distance and the investigated setup. For the same relative distance η, the observed blurring increases with larger grating periods. A qualitative comparison shows, that the blurring for the different setups reaches a similar extend for the $SG_{4.8}$ and the DG setup at all distances. The comparison of the profile at the relative distance $\eta = 7/16$ to the other two setups show that a similar quality is reached at $\eta = 5/16$ for the SG_7-setup and at $\eta = 3/16$ for the SG_{10}-setup. This affirms the assumption that the beamsplitter characteristic is one of the driving forces for image blurring with increasing propagation distance. The refraction angle decreases linearly with the grating period, but the effect of blurring increases with larger grating periods for a fixed relative distance as the Talbot distance increases quadratic with the grating period. A material dependent effect on the image blurring could be observed from the present investigation, thus the relative distance declared by equation 3.10 will be used as quantitative measure for further analysis. This distance will be called *critical distance d_c* in the following.

To compare the performance of the different setups the sensitivity of each setup was calculated, dependent on the propagation distance d, interference pattern
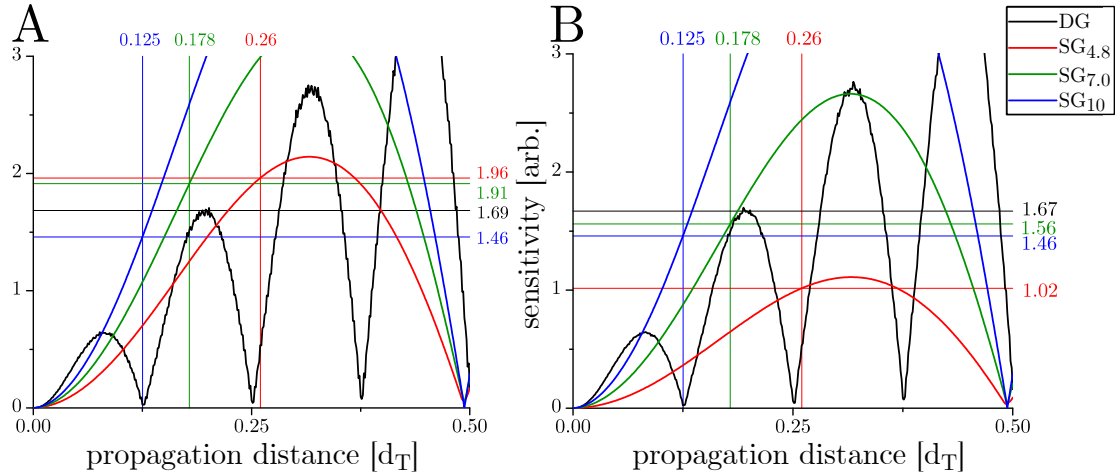
Figure 3.3: A: The comparison of the sensitivity shows an advantage in using smaller grating periods when the blurring by the detector system can be neglected. B: By adding a not negligible point spread function to the simulations, the sensitivity drops dramatically for small grating periods. The double grating interferometer is almost not affected as the analyser grating is used to resolve the interference pattern. The sensitivity results given in Table 3.4 are marked within the figure.

period p, visibility V and the photon counts N.

$$s \sim \frac{d}{p} \cdot V \sqrt{N} \tag{3.18}$$

Here, the fraction d/p is proportional to the obtained signal and $1/(V\sqrt{N})$ is expected to be proportional to the noise. The influence of the photon counts is the same for every of the setups except the double-grating setup. Due to the presence of the analyser grating half the photons are absorbed, thus a factor of $N = 1/2$ is used for the double-grating setup.

Figure 3.3 shows the comparison of the sensitivity for the optimum case that the visibility of each setup is almost not affected by the optical components of the whole setup (FWHM of point spread function (PSF) equal to 10% of the grating period) and a more realistic case where a Gaussian-shaped PSF (FWHM=1 μm) is added to the simulation. In the optimum case, the comparison of the sensitivity of the different SG-setups up to the critical distance d_c shows an advantage in reducing the grating period and enlarging the relative propagation distance.

37
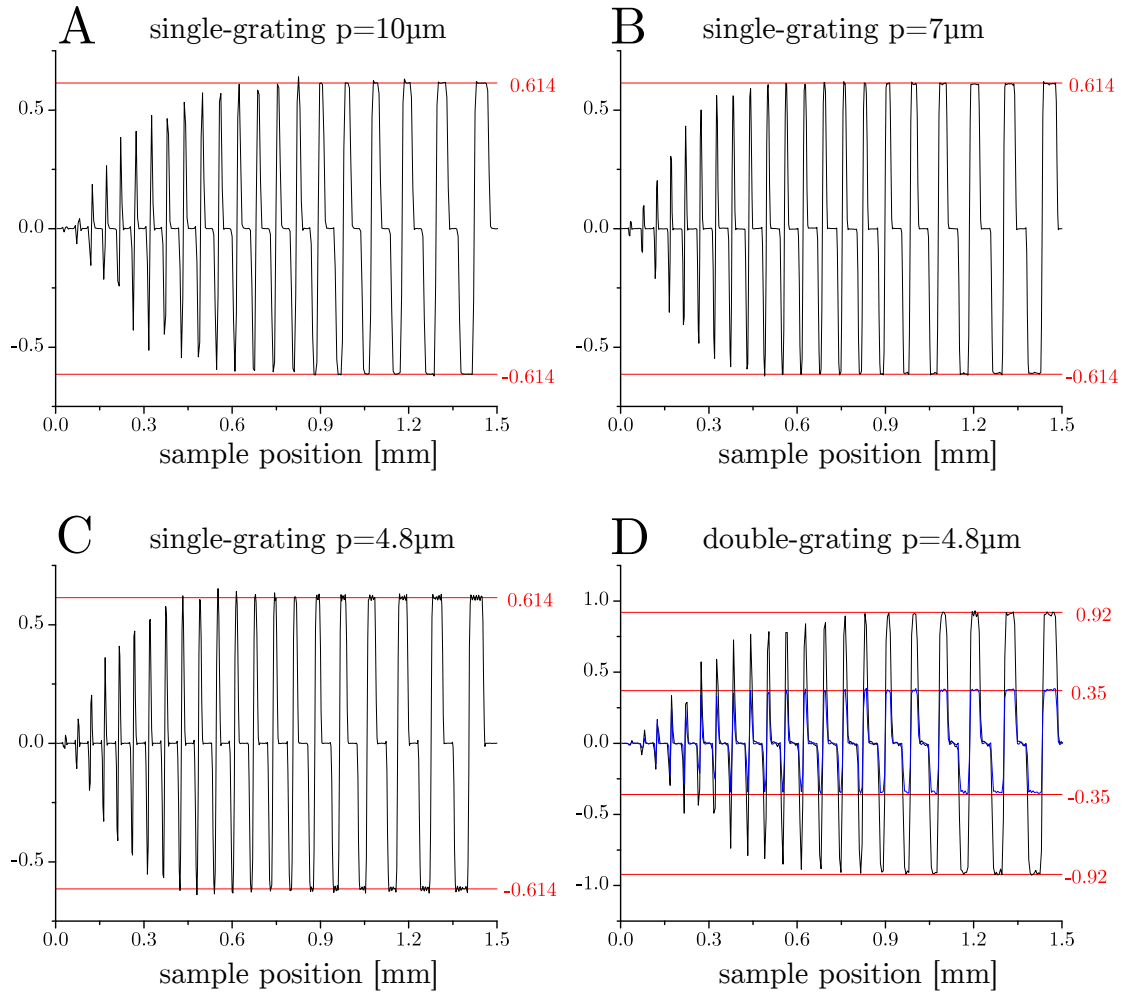
Figure 3.4: Simulated projections of a test pattern for the different setups at the highest sensitivity below the critical distance. The red lines indicate the theoretical value. For all setups all elements of the test pattern can be recognised. Below a certain size of test pattern element the signal does not reach the correct value. With smaller grating periods of the SG-setup more features reach a correct signal. The DG setup behaves similar as the SG_{10}. With a shorter propagation distance the accuracy is similar to the SG_7- and SG_4.8-setup (blue line).

The sensitivity of the DG-setup is lower than for the SG_7-setup and $SG_{4.8}$-setup, but larger than for the SG_{10}-setup. For a camera system with a not negligible PSF the sensitivity of a single-grating setup drops rapidly with smaller grating periods. For the double-grating interferometer, where the analyser grating and not the detector is used to resolve the interference pattern, only a minor influence of the PSF is recognised. In this latter case the sensitivity for the double-grating setup is slightly higher than for the less affected single-grating setups SG_{10} and SG_7. In table 3.4 the results for the highest sensitivity below the critical distance are summarised with the according visibility values.

As comparison for the resolution of the different setups, especially for small features, figure 3.4 shows the acquired profiles of the simulated test pattern. All profiles were acquired at the critical distance d_c except for the double grating setup that shows a higher sensitivity at a distance shorter than d_c. For all setups all features are visible even with sizes much smaller than the utilised grating periods. However, the strength of the signal dramatically falls for test pattern elements smaller than a certain size. The DG setup shows a similar signal trend as the SG_{10} setup, while the $SG_{4.8}$ and SG_7 setup show the better accuracy for the small test pattern structures. By reducing the propagation distance for the DG-setup to the first peak of the sensitivity distribution (close to the first fractional Talbot distance) the obtained signal becomes strongly reduced, but also more accurate for the small test pattern features. From this comparison the conclusion is drawn that the physical propagation distance is the most important factor for the accuracy for small structures.

A main difference between the single-grating and double grating setups becomes visible in the obtained signal. Due to the utilisation of a π-shift grating for the double grating interferometer and the resulting interference pattern period of $p_1/2$ a much higher signal is obtained for a similar level of sensitivity.
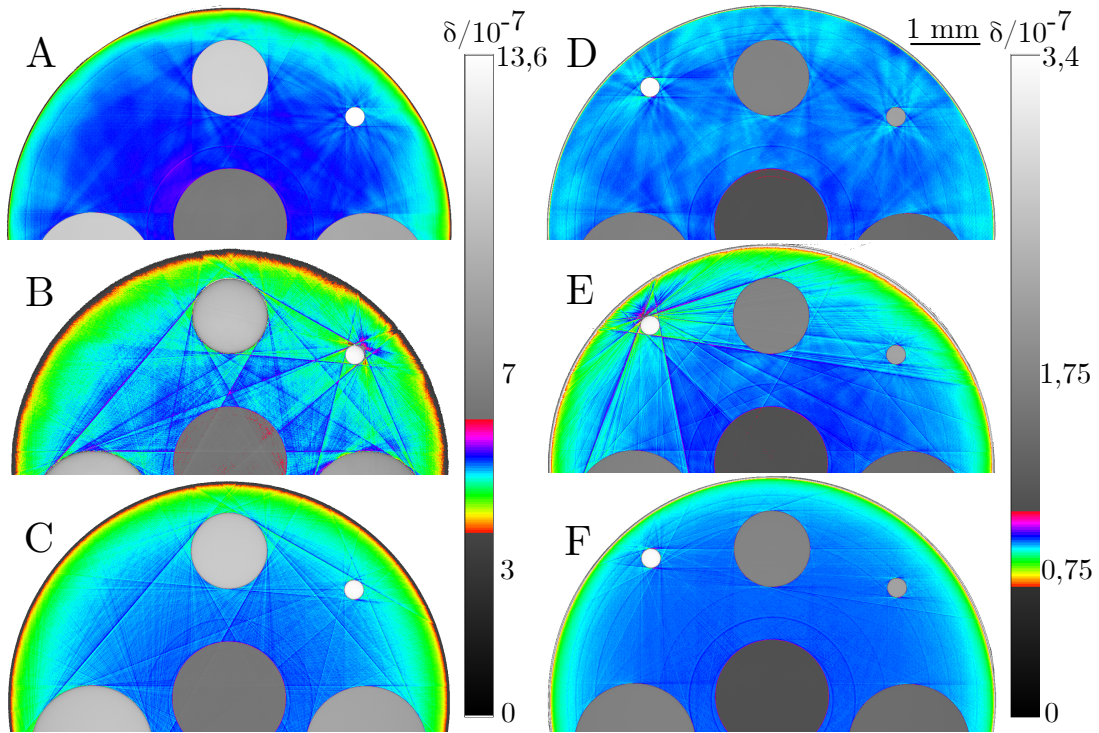
Figure 3.5: Reconstructed slices for the different setups at 20 keV (A-C) and 40 keV (D-F). For both energies the DG_1-setup (A+D) shows the best image quality followed by the SG-setup (C+F). The DG_3-setup shows significant image artefacts at both energies. For all setups the reconstructions at 40 keV show less artefacts. The base material of the sample is visualised in false colors for better visualisation of the artefacts.

3.3.2 Tomography

Tomography simulations of a test phantom were performed to verify the findings from the projection simulations. The simulated test phantoms consist of the same materials as the ones used later on for the test experiments, namely $PMMA$, PA 6.6, Mg, $PCTFE$, $PTFE$, Al, Ti (sec. 5.1 tab. 5.2). The simulations conducted of three different setups, two double-grating setups with $p_1 = 4.8\ \mu m$ and $p_2 = 2.4\ \mu m$ and one single-grating setup with $p_1 = 10\ \mu m$. Based on the findings from the sensitivity investigation, the inter-grating distance for the double-grating setup was set to the third fractional Talbot distance and the propagation distance for the single-grating setup was set to half of the first fractional Talbot distance.

Table 3.5: SNR values for the three simulated setups at 20 keV and 40 keV.

	Material	SG	DG_1	DG_3
20 keV	PMMA	139	165	68
	PA 6.6	120	203	44
	Mg	183	167	95
	PCTFE	250	206	114
	PTFE	227	219	97
	Al	258	180	43
40 keV	PMMA	180	109	124
	PA 6.6	275	169	67
	Mg	228	140	159
	PCTFE	280	216	223
	PTFE	252	222	136
	Al	252	162	185
	Ti	175	178	68

For comparison with a setup of lower sensitivity, the simulation for the double-grating setup was repeated at the first fractional Talbot distance. A comparison of the reconstructions is presented in figure 3.5.

The retrieved SNR-values, presented in table 3.5, obtained from the simulations clearly show the inferiority of the DG_3-setup. The low SNR-values compared to the DG_1- and SG-setup result from the strong presence of streak artefacts. These streak artefacts result from phase-wrapping and therefore from a too high sensitivity. The streak artefacts are clearly visible in the reconstructions, most intense around the most dense material. Also for the SG-setup, streak artefacts can be observed at 20 keV along the materials edges, which are almost not present any more at 40 keV.

For the measurements at 40 keV the SNR-values for the SG-setup are about a factor of 1.6 larger than the values for the DG_1-setup. Although the superiority of the SG-setup is in accordance with the sensitivity considerations, the value of 1.6 is below the expectations of a factor of > 2 from the sensitivity considerations. The comparable low SNR-value for titanium in the SG measurement indicates, that the reconstruction is still corrupted by artefacts. These artefacts might also cause the values to be lower than expected. A quantitative comparison between the SG

and the DG_3 measurement is unrewarding due to the strong corruption of the DG_3 reconstruction. Regarding the spatial resolution achieved in the reconstruction, the different materials in the simulated object were analysed utilizing an MTF-analysis of the materials edges as later described in section 5.8. The determined resolution for all materials independent on the measurement type was determined to roughly 5 μm. This is on the one hand in perfect agreement with the previous investigations, but again is contrary to the assumption that the resolution will be dependent on the investigated material.

Instability

As final part of the simulations study the influence of instability of the grating interferometer together with an period mismatch (only double-grating) is investigated. Due to the beam divergence the projected grating period of the phase grating onto the analyser grating slightly differs from its physical dimension. Although this difference is only in the range of 1-2 ‰ it will result in remaining fringes on the projections. Assuming a perfect stable setup these remaining fringes will vanish by the flat field correction. With a slight instability, introduced by random grating displacement, the fringes are not removed correctly by the flat field correction and will remain in the retrieved phase projection. This will finally result in a disturbed background of the reconstruction. Figure 3.6 shows the introduced artefacts from the instability by appearance of long scale artefacts and increase of high frequent noise. The simulations took into account a grating displacement up to 200 nm for both gratings of the double-grating interferometer. For the single-grating interferometer the displacement was up to 3 μm, as no significant effects were observed for the range up to 1 μm. A increase in the high frequent noise clearly becomes visible, but no low frequent artefacts occur.
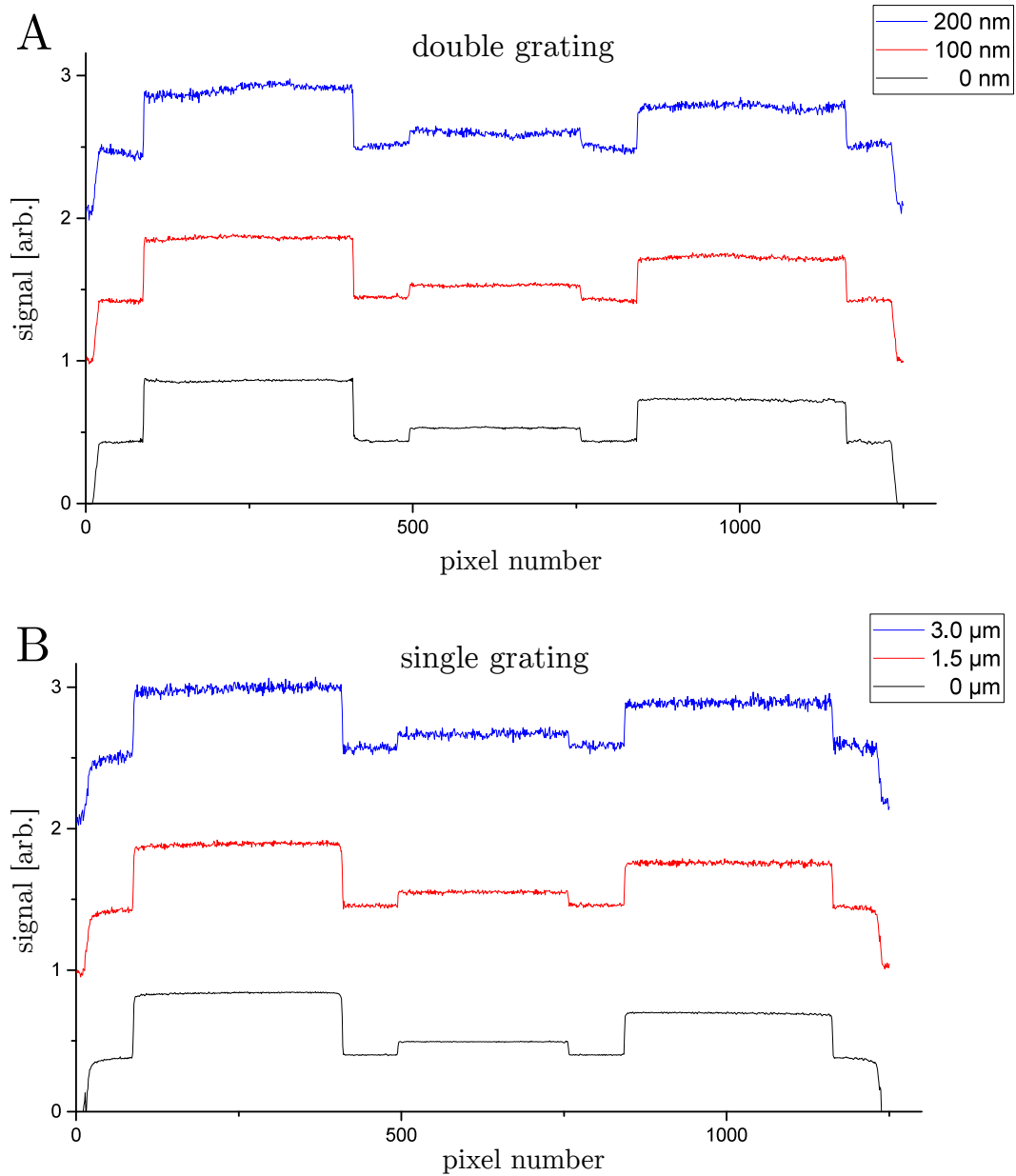
Figure 3.6: Illustration of the influence of grating instabilities. For the *DG*-setup (A) and the *SG*-setup (B) three different levels of instability are plotted. With grating instabilities in the range of a few hundred nanometres the *DG*-setup gets strongly affected by low frequent artefacts additional to high frequent noise. For the *SG* interferometer significant influence on the image quality becomes visible in the range of a few micrometer. High frequent noise can be observed, whereas low frequent artefacts as for the *DG*-setup cannot be noticed.

3.4 Summary

The simulation based investigations of the different setup types revealed valuable information about the expectable performance.

Initial calculations have shown that with the aim on a high resolution setup a strong loss of sensitivity has to be taken into account. While the maximum sensitivity theoretically is reached at several meters of propagation distance, a reasonable resolution can only be achieved at a propagation distance up to the third fractional Talbot distance and is strongly dependent on the phase grating period. Simulated projections of a test pattern consisting of several double wedges have moreover shown, that the blurring strongly increases by the propagation distance. Not only the blurring, but also the sensitivity increases with the propagation distance, therefore the performance of a grating interferometer always relies on a trade off between resolution and sensitivity.

At the critical distance, defined by a certain beam separation, all simulated setups could reach a similar sensitivity with an advantage for smaller grating periods. However, this requires that the point spread function is negligible. For a none negligible point spread function, the smaller grating periods are strongly effected by the blurring and the associated reduced visibility. Therefore, the spatial resolution given by the detector system is the main criterion for the utilisation of a single-grating interferometer and its most important performance characteristic.

Although a high sensitivity is desired in order to achieve a reasonable contrast between the materials, the simulated tomography of the phantoms have shown the vulnerability of the performance for a too strong signal. Phase wrapping as a consequence can have dramatical influence on the obtained signal to noise ratio due to the presence of wrapping artefacts. With higher energies the risk of artefacts occurring can be reduced. For non corrupted projections, the increase in energy will result in a decreased signal to noise ratio.

Not only artefacts from phase wrapping, but also from instabilities of the setup are a serious issue. Especially the double-grating interferometer can be strongly affected by unstable gratings resulting in image artefacts. Here, the single-grating interferometer has a strong benefit as it seems to be more robust against the occurrence of low frequent artefacts.

4 Instrumentation

4.1 Frontend

Both beamlines are equipped with a 2 m undulator as insertion device. The coherence of a light source for long propagation distances z can be expressed by [82, 83]:

$$\xi = \frac{z\lambda}{2\pi\sigma} \ ,$$

(4.1)

with λ as the wavelength of the radiation and σ as source size of the source. A more detailed expression for the spatial coherence and the storage ring characteristics of PETRA III can be found in chapter A. For a 2 m undulator insertion device is denoted as 35 μm in width. The distance from the source is approximately 90 m at the beamline P07 and 70 m for the beamline P05. With this, the coherence length at the experiment for the used energies (20 keV (P05) and 40 keV (P07)) is $\xi_{20keV} = 20 \ \mu m$ and $\xi_{40keV} = 13 \ \mu m$. It was shown that for a sufficient visibility, a spatial coherence length of approximately the grating period is needed for $\pi/2$-shift setup and half of the grating period for a π-shift setup [84]. Thus the spatial coherence at both beamlines is sufficient for the used periods of 4.8 μm (π-shift) and 10 μm ($\pi/2$-shift).

The beamline P05 is equipped with a Si(111) double crystal monochromator (DCM, Bragg-Bragg geometry) in vertical orientation and the energy is tunable from 5 keV to 50 keV. At the beamline P07 also a Si(111) DCM (Laue-Laue geometry) is installed but in horizontal geometry, allowing for an energy range between 33 keV and 150 keV. The vertical geometry causes a slight energy shift in vertical direction, whereas the horizontal geometry invokes a energy shift in horizontal direction. In both cases the energy shift is negligible for DPC-tomography due to the small bandwidth of DCM monochromators ($\Delta E/E \approx 10^{-3} - 10^{-4}$).

4.2 **Tomography End Station**

The tomography setups are placed approximately 70 m (P05) and 90 m (P07) from the source. The main equipment consists of a high precision air-bearing rotation axes (Aerotech Inc.) and a movable detector tower. To allow for sample environments requiring a hanging sample, an alternative hanging rotation axis can be installed with equivalent properties as the primary axis. The detector tower can be equipped with two cameras, selectable by a movable mirror. The front of the camera tower holds a scintillator screen and a lens system with four different objective lenses, allowing for a magnification factor of 5, 10, 20 and 40. The whole detector tower can be moved along the beam direction to freely adjust the propagation distance between sample and scintillator screen.

Coordinate System

The coordinate system at both tomography stations is defined the same way. The x-direction is horizontally perpendicular to the beam direction. The beam direction gives the y-axis and the z-axis is defined vertical.

Camera System

For the experiments of this project, the detector tower was equipped with two different cameras, a CCD-based camera for a high dynamic range, and a CCD-based camera for high resolution and fast acquisition. The CCD-camera is based on a Kodak KAF-09000 chip with 3056×3056 pixels and a pixel size of 12×12 μm^2 and a depth of 16-bit. The CMOS-camera is based on a Cmosis CMV20000 chip with 5120×3840 pixels and a pixel size of 6.4×6.4 μm^2 and a depth of 12-bit. The CMOS-camera is a custom-made system developed by a collaboration between the IPE/KIT[1] and the HZG. This camera is designed for a maximum frame rate up to 30 Hz, while the CCD-camera is limited to ≈ 1 Hz. Both cameras were coupled via the same magnifying optics ($5\times$) to the scintillator screen (100 μm $CdWO_4$), resulting in effective pixel sizes of 2.4 μm and 1.3 μm.

---

[1]Institute for Data Processing and Electronics, Karlsruhe Institute of Technology
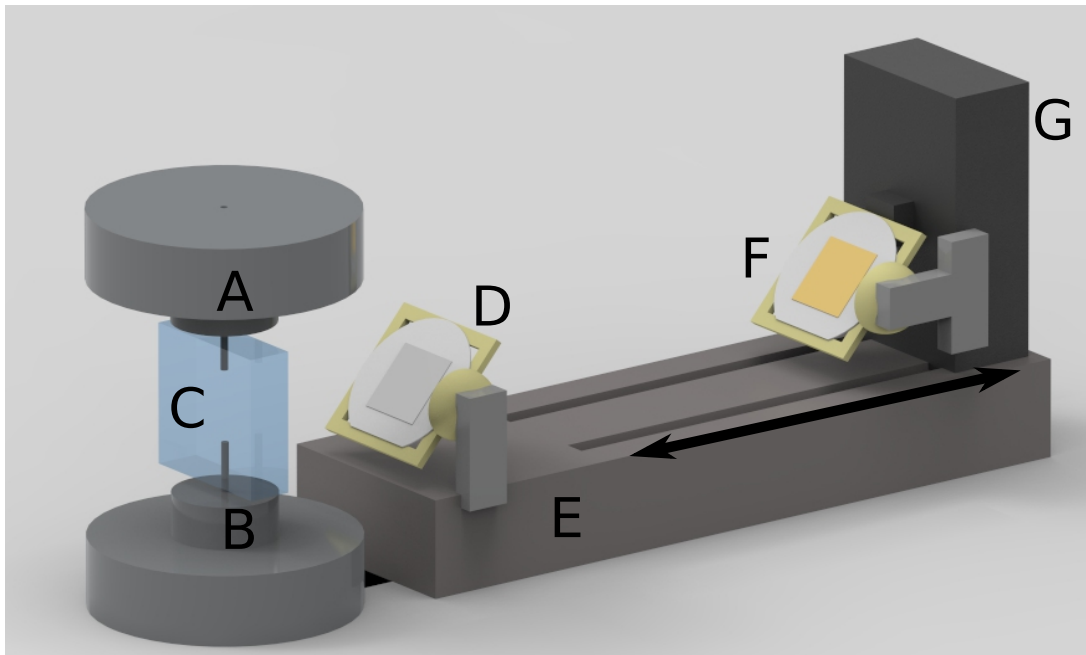
Figure 4.1: Drawing of the experimental setup. The sample can be mounted optionally from the top or bottom (A+B), dependent on the required sample environment (C). The phase grating (D) is mounted to the granite substructure (E). The analyser grating (F) is mounted to the movable detector tower (G). The grating holders allow precise alignment of both gratings individually.

4.3 Interferometer

4.3.1 Grating Holders

The grating holders were fixed independently to the instrument. Unlike the implementation at other beamlines (e.g. ESRF / ID 19), where the whole interferometer is fixed on a common frame, the separate mounting makes the interferometer more vulnerable to instabilities. On the other hand it allows for much more flexibility regarding the alignment of the gratings and the adjustment of the inter-grating distance. The grating holder for the analyser grating is directly fixed to the detector tower to place it on a minimum distance from the scintillator screen. This has the additional advantage that the inter-grating distance can be easily adjusted with high precision by moving the detector tower. Both grating holder units were built from the same components, besides the additional piezoelectric actuator at
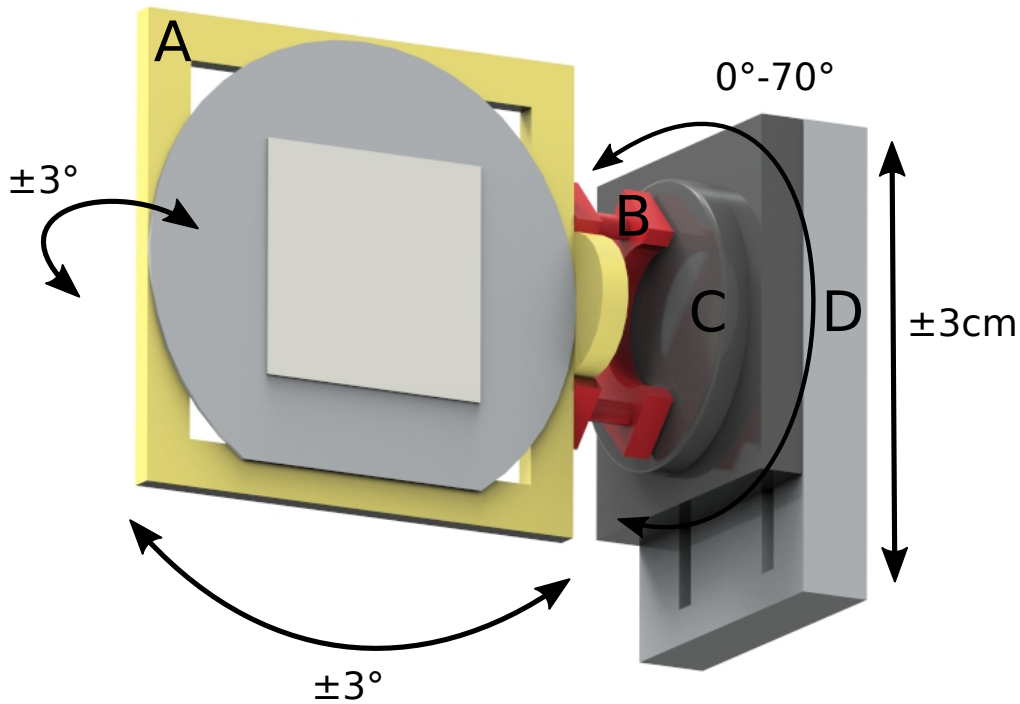
Figure 4.2: Drawing of the designed grating holders. The grating frame (A) is mounted to a combination of mirror mount (B), rotation axis (C) and translation axis (D).

the phase-grating unit. A vertical translation axis allows to move the grating in the range of a few centimetres. With a rotation axis built on the translation axis, the grating can be tilted towards the beam direction (around the x-axis) in the range of 0° to 70°. As connection between the grating frame and the rotation axis, a piezoelectric driven mirror mount (Newport - New Focus) is used to allow for rotation alignment of the grating around the y-axis and z-axis in the range of ±3°. Figure 4.2 shows a drawing of the designed grating holders. The rotation along the x-axis is very important as it lets adjust the effective grating structure height to match the desired energy. This makes a swift change of the used energy and adjustment of the interferometer possible at any time. Moreover this procedure allows to use a continuous energy range in contrary to grating setups relying on separate sets of gratings for distinct energies. The rotation around the y-axis is used for a mostly vertical alignment of the grating structures and for parallel
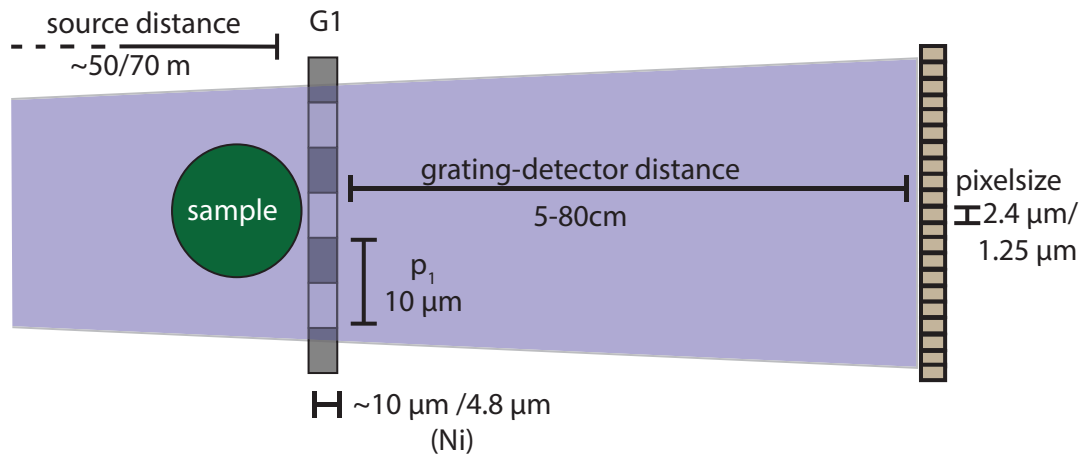
Figure 4.3: Sketch of the single-grating setup instrumentation. The phase grating (nickel) with a period of 10 μm and a height of 10.4 μm is placed behind the sample. The propagation distance can be adjusted between 5 cm and 80 cm. Dependent on the chosen detector system the effective pixel size can be either 2.4 μm or 1.3 μm.

alignment of the structures from both gratings. Due to the beam divergence the projected period of the phase grating onto the analyser grating will differ for different inter-grating distances. To adjust the effective period the phase grating is slightly rotated around the z-axis, resulting in a smaller projected period. The vertical translation is used to slightly shift the grating for a different active area, in case of strong grating effects (e.g. radiation damage).

4.3.2 Setups

All gratings used for the interferometer setups were fabricated by the Institute for Microstructure Technology (IMT) of the Karlsruhe Institute of Technology (KIT) using the LIGA technology [24]. As substrate, 4" Si-wafers with a thickness of 200 μm were used for the phase-gratings. The analyser grating for the double-grating setups used a 525 μm thick 4" wafer as substrate. The grating structures were made of nickel for the phase gratings and gold for the analyser grating.

Single Grating

The single-grating setup for all measurements consists of a phase-grating with period $p_1 = 10\ \mu m$ and a structure height of 10.4 μm, inducing a phase-shift of $\pi/2$ at its design energy of 60 keV. Due to the similarity of the interference pattern related to a phase-shift of $\pi/2$ and $3\pi/2$, the grating is also suitable for an experiment at $20 keV$. For all other energies the effective structure height can be adjusted appropriately by tilting the grating towards beam direction by a certain angle α.

$$\alpha(E) = \begin{cases} \arccos(20\ keV/E) & \text{for } 20\ keV \leq E \leq 60\ keV \\ \arccos(60\ keV/E) & \text{for } E \geq 60\ keV \end{cases} \tag{4.2}$$

An important factor for a satisfying performance is an adequate ratio of interference pattern period p_1 to pixel size s, which should satisfy:

$$\frac{p_1}{s} \geq 4 \tag{4.3}$$

With the effective pixel sizes of 2.4 μm and 1.3 μm, the grating of $10 \mu m$ period fits to equation 4.3 and can be resolved directly with both camera systems. The propagation distance behind the phase-grating is adjusted by placing the detector tower and thereby the scintillator screen to the required position. In total the detector tower can be placed up to 100 cm from the phase-grating. Due to the limited travel distance of the detector tower, the energy range of the single-grating setup is limited by the reachable propagation distance. So far, the highest photon energy used successfully with this setup was 80 keV, but with a very short propagation distance of only a quarter of the first fractional Talbot distance. For higher energies or a larger relative propagation distance a phase grating with a smaller period has to be used. Figure 4.3 presents a sketch of the single-grating setup and its dimensions.

Double Grating

Dependent on the energy range, the double grating interferometer was set up with two different phase gratings. Both gratings have a period of 4.8 μm, with structure heights of 7 μm and respectively 14 μm. These structure heights correspond to

Figure 4.4: Sketch of the double-grating setup instrumentation. The phase grating (nickel) with a period of 4.8 μm is placed behind the sample. Its height is 7 μm respectively 14 μm. The analyser grating (gold) has a period of 2.4 μm with a structure height of $\approx 100~\mu m$. The inter-grating distance can be adjusted between 5 cm and 80 cm. Dependent on the chosen detector system the effective pixel size can be either 2.4 μm or 1.3 μm.

design energies of 20 keV and 40 keV. Other energies than these two can be applied by tilting the appropriate grating towards the beam direction by a certain angle α:

$$\alpha(E) = \begin{cases} \arccos(20~keV/E) & \text{for } 20~keV \leq E < 40~keV \\ \arccos(40~keV/E) & \text{for } E \geq 40~keV \end{cases} \quad (4.4)$$
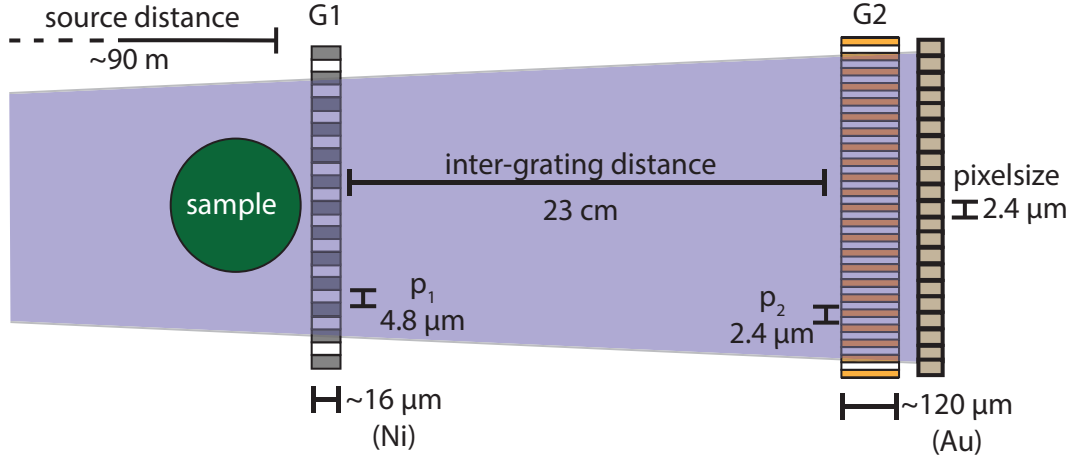
The analyser grating for all setups has a period of 2.4 μm and a structure height of $\approx 100~\mu m$. To achieve such a high aspect ratio, the grating was produced using the 'sunray'-design [85]. For a tilted setup the analyser grating was tilted by the same angle to keep the inter-grating distance constant across the full field of view. The tilt of the analyser grating also results in a higher effective structure height, which comes with a better absorption. With the analyser grating directly mounted to the detector tower, the inter-grating distance was adjusted by moving the detector tower. This setup was successfully utilised in the energy range from 20 keV up to 100 keV [86]. Figure 4.4 gives a sketch and dimensions for the double-grating interferometer setups.

5 Experimental Results

5.1 Performed Experiments

All single-grating experiments were performed with the setup described in section 4.3.2. Only one grating with period $p_1 = 10 \ \mu m$ was available for the single grating setup. The structure height of the phase-grating was $h_1 = 10.4 \ \mu m$, corresponding to a $\pi/2$-shift at the design energy $60 \ keV$. To adjust the projected grating structure height to a given X-ray energy, the phase-grating was tilted towards beam direction with a certain angle. For energies lower than $60 \ keV$, a phase shift of $3\pi/2$ was targeted which creates a intensity pattern of the same period. The tilt angle α for a certain energy E is then described as:

$$\alpha(E) = \begin{cases} \arccos(20 \ keV/E) & \text{for } 20 \ keV \le E \le 60 \ keV \\ \arccos(60 \ keV/E) & \text{for } E \ge 60 \ keV \end{cases} \tag{5.1}$$

For the double-grating setup two different phase gratings were utilised. Both gratings had a period of $p_1 = 4.8\mu m$ while their height was $h_1 = 7\mu m$ and $h_1 = 14\mu m$. For the desired phase-shift of π, these heights are equivalent to design energies of $20 \ keV$ and $40 \ keV$. As for the single-grating setup, energies different than the design energies become available by a tilt towards the beam direction:

$$\alpha(E) = \begin{cases} \arccos(6.7 \ keV/E) & \text{for } 6.7 \ keV \le E \le 20 \ keV \\ \arccos(20 \ keV/E) & \text{for } 20 \ keV \le E \le 40 \ keV \\ \arccos(40 \ keV/E) & \text{for } E \ge 40 \ keV \end{cases} \tag{5.2}$$

Following the simulation results, the propagation distance was set to half of the first fractional Talbot distance for the single-grating setup. The inter-grating distance for the double-grating interferometer was set to the third fractional Talbot distance. At distance strong artefacts are expected, therefore the measurements

Table 5.1: Experimental parameters for the different measurements with the single-grating setup SG and the double-grating setups DG_1, DG_3. Phase grating period p_1, analyser grating period p_2, phase shift Φ, phase grating height h_1, analyser grating height h_2, propagation distance d and visibility V.

		SG	DG_1	DG_3
	p_1	10 μm	4.8 μm	4.8 μm
	p_2	–	2.4 μm	2.4 μm
	Φ	$3\pi/2$	π	π
20 keV	h_1	10.4 μm	7 μm	7 μm
	h_2	–	≈ 100 μm	≈ 100 μm
	d	40 cm	4.6 cm	13.9 cm
	V	8%	49%	38%
40 keV	h_1	20.8 μm	14 μm	14 μm
	h_2	–	≈ 100 μm	≈ 100 μm
	d	80 cm	9.3 cm	27.9 cm
	V	6%	25%	16%

were repeated at the first fractional Talbot distance.

The tomography experiments were conducted at a photon energy of 20 keV and 40 keV using both single-grating and a double-grating setup. The setup parameters are listed in table 5.1. To achieve a phase-grating height of 20.8 μm for the SG-setup the grating was tilted by an inclination angle of 60°.

For the measurements at 20 keV and 40 keV two different cameras were used. For the 20 keV measurements a CCD-based camera with an effective pixel size of 2.4 μm and a dynamic range of 16 bit was used, whereas the measurements at 40 keV were performed using a CMOS-based camera with an effective pixel size of 1.3 μm and a dynamic range of 12 bit. For a subsequent comparison of using the two camera systems the single-grating measurement at 40 keV was repeated using the CCD-camera. For each tomogram a series of 900 projections were taken with a sample rotation over 180°. For each projection a series of four images (three phase steps) was taken, where not otherwise stated. Although the minimum number of phase steps needed to determine the phase of the stepping curve is only two, measurements with only three images per phase-scan where not reliable. All the visibility values for these setups did not match the values
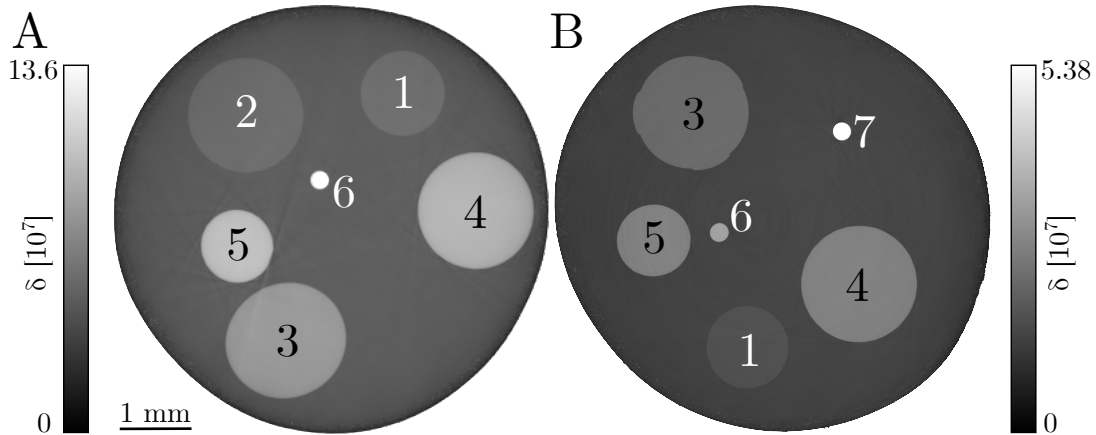
Figure 5.1: Cross section of the phantom samples used at 20 keV (A) and 40 keV (B). 1: PMMA, 2: PA 6.6, 3: Magnesium, 4: PCTFE, 5: PTFE, 6: Aluminium, 7: Titanium.

obtained by simulations, but were much lower. For the single-grating setups only a very low visibility $< 10\%$ could be reached. This indicates that the blurring due to the detector system (scintillator) could be much stronger then expected. For the double-grating setup the visibility difference is most likely a reason of grating imperfections. Especially the analyser grating is easy to be effected by misshaped structures, due to the high aspect ratio.

Phantom Sample

Different polymer and metal rods were embedded in a polymer matrix as phantom samples. The designed diameter of the phantoms is 6 mm in order to match the field of view of the detector system, leaving some free space around the sample for background corrections and noise analysis. Each phantom was fabricated with a compilation of 6 different rods from the materials listed in table 5.2. The table list the values for the mass density ρ_m and the electron density ρ_e. These values are in close relation to the attenuation coefficient μ and respectively the refractive index decrement δ (sec. 2.1), which are energy dependent. The materials and their respective diameters were chosen to cover a wide range of attenuation and phase-shift cross section, and meanwhile keeping the maximum attenuation low enough to minimize the possible starvation effects [87].

Table 5.2: List of the used materials for the test phantoms, describing their diameter, mass density ρ_m and electron density ρ_e.

Material	Diameter $[mm]$	ρ_m $[g/cm^3]$	ρ_e $[10^{23}/cm^3]$
PA 6.6[1]	1.6	1.14	3.77
PMMA[2]	1	1.19	3.87
Mg	1.6	1.74	5.17
PCTFE[3]	1.6	2.13	6.25
PTFE[4]	1	2.16	6.24
Al	0.25	2.70	7.83
Ti	0.25	4.50	12.45
HMA[5]	≈6	≈0.9	≈3.2

The selected rods were fixated on a sample holder, a certain distance between the rods was kept for the segmentation later on and also to reduce the probability of trapping air voids when filling up with the polymer matrix. To embed the phantom in the matrix a straw first was filled with the hot-melt adhesive. While still hot, the phantom was slowly plunged into the still soft polymer. Due to its solid components and the sealing by the polymer matrix the phantom is mechanically stable and insensitive for environmental influences.

Liquid phantoms are often used in phase-contrast tomography as test samples. They consist of several tubes with various solutions of different concentrations[22, 88]. This type of phantom clearly benefits from the flexibility in material composition. With careful selection of solute and solvent a mixture of almost any wanted electron and mass density can be created. In comparison to a liquid phantom, a solid phantom provides a long term stability. Loss of solvent due to evaporation or a partially decomposition of the solutions in liquid phantoms makes the concentration unreliable after storing for some time. The possible range of mass or electron density for a solid phantom is not as broad as for liquid ones. However, the physical properties of the phantom are better defined and thus the obtained

---

[1]Polyamid, Nylon 6.6

[2]Polymethylmethacrylat

[3]Polychlortrifluorethylen

[4]Polytetrafluorethylen

[5]Hot melt adhesive, composition not known.
  The values listed in the table correspond to Polyethylene a common base material of HMA.

results are more reliable. Especially for later verification measurements or when the experiments has to be repeated, the composition stability is more reliable for the solid samples.

5.2 Evaluation Aspects

Aim of the performed experiments was to evaluate the performance of a single grating interferometer, especially in the framework as an experiment at PETRA III. To achieve comparative data from the different setup modalities, different test phantoms with well defined materials were used. The following characteristics were used to access and evaluate the results:

Accuracy

One advantage of grating-based phase-contrast imaging is the quantitative data obtained from the measurements. As this ability to retrieve exact values for the refractive index is the main advantage against the propagation-based phase-contrast, the accuracy of the retrieved values is of high importance to justify the additional effort of this method. The retrieved refractive index decrement values were compared to literature values given by the DABAX database using the XOP software[32]. The signal-to-noise ratio (SNR) is also calculated to compare the results, namely to define a reliability of the retrieved δ-values.

Noise

The noise values were not only retrieved from the tomographic reconstructions in combination with the quantitative δ-values to calculate the SNR, but also from the projections dataset to determine the sensitivity of the method by its minimum detectable refraction angle (eq. 3.2). As a mean criteria for the obtained image quality we can look at the signal to noise ration of the different materials at the distinct measurements. This gives a rather good assessment of the quality of the system. The variation is mainly driven by the noise level as the signal should be only material dependent. Sensitivity and visibility of the system are the leading factors to influence the noise.

Spatial Resolution

One of the main reasons to perform an experiment at a synchrotron radiation facility instead of a conventional source is the achievable spatial resolution in combination with high density resolution. Grating-based phase-contrast especially benefits from the high spatial resolution achieved without a magnifying cone beam setup. Therefore the spatial resolution is the most important performance characteristic. A typical instrument for the determination of the spatial resolution of full-field imaging techniques is the projection of a test-pattern. A Siemens Star [89] is the most common used test pattern for most tomography experiments, in order to precisely detect the spatial resolution. Other instruments like different sized line pairs are also suitable. However, to create such a test pattern to characterize the spatial resolution using a grating interferometer is challenging, because the obtained signal relies on a differential phase-shift. A suitable object would have to consist of bar pattern with raising thickness in each of the bars. In the small micrometer range such structures are extremely difficult to fabricate. A more applicable method to determine the resolution exploits the modulation transfer function(MTF) of a precise edge which can be found as the border between two individual materials in a 3D-reconstruction [90, 91, 92].

Acquisition Speed

For attenuation-based experiments the speed of a phase-contrast tomography is of high interest. More and more experiments performed at synchrotron radiation facilities rely on a very fast acquisition time in order to visualize time-dependent developments within the sample. Built on an attenuation-based experiment as basis, the possibilities to speed up the grating-based phase-contrast experiment are very limited. To be exact, the speed of the system is given by the tomography system used as base and modified by the time needed to perform the phase-stepping. For this reason the number of phase steps has to be kept as small as possible for time-critical experiments. A simple solution to avoid this additional acquisition time is to rely on the single-shot or fringe-analysis approach [66, 93, 67, 94]. This method allows for an acquisition time equal to the one of an attenuation-based tomography. A consequence of this method is the reduced resolution, which is limited to the fringe period analysed (sec. 2.3.4). Another option to gain an

experiment with a reasonable time consumption is to rely on fast detector system. Two camera systems (CMOS-based vs CCD-based) and their achieved image quality were compared to evaluate how much the tomogram quality suffers from the reduced accuracy of the camera system and if it is acceptable in respect to the reduced acquisition time.

Setup Preparation and Stability

Speed as performance characteristic can not only be determined by the needed acquisition time for a tomogram using the investigated interferometer setup. An evaluation also has to take into account the time needed for alignment. This is a critical point, since the alignment of the interferometer can only be done with the X-ray beam. A fast and precise alignment therefore is desired to save precious beamtime. Also the possibility of the interferometer to 'fail' has to be minimized. Another point where speed is a relevant quantity is for the time spend on reconstructing a dataset. As the experiments at the synchrotron tomography stations are often designed for a high speed acquisition in order to investigate a large number of samples, the time needed to post-process the acquired datasets can easily accumulate to an immense workload. Therefore an automatized post-processing and reconstruction workflow is needed to provide the experiment users with reconstructed datasets within a reasonable time. To keep an automatized reconstruction workflow alive, the failures and instabilities of the experimental setup have to be minimized.

Reconstruction Artefacts

Although reconstruction artefacts are a rather subjective criteria as an automated evaluation is not possible to quantify, it is still a major criteria for the performance analysis. The most common reconstruction artefacts are: Ring artefacts, cupping as a reason of phase wrapping, streak artefacts from phase wrapping but also caused by corrupted projections and so-called clouds occurring from remaining fringes in the projections. While ring artifacts can easily be removed by several computational methods [95, 96, 97], the implementation of those filters in most cases requires a manual adjustment of the filter parameters, which are dependent on the actual dataset.

Table 5.3: Sensitivity values obtained for the different measurements. Minimum detectable angle in *nrad*.

Energy	SG	DG_1	DG_3
20 keV	145	246	123
40 keV	87	123	42

5.3 Sensitivity

The sensitivity of three different modalities was determined by evaluation of the background noise in the taken projections. As measure for the sensitivity, the minimum resolvable refraction angle a_{min} (eq. 3.2) was calculated. For each projection the standard deviation outside of the object area was determined. With the average over all projections the values listed in table 5.3 were obtained.

From the ratios of grating period to propagation distance, a factor of 2 respectively 0.7 would be expected between the single-grating setup and the double-grating setup at the 1st respectively 3rd fractional Talbot-distance. Beside the measurement for the DG_3-setup, the double-grating sensitivity values are better then expected in comparison to the single-grating setup. The comparison between the two double-grating setups gives the expected factor of 3 for the measurement at 40 keV, but only a factor of 2 at 20 keV. While the too low sensitivity values for the single-grating setup can be explained by the comparable low visibility value, the discrepancy between the sensitivity for the DG_3 at 20 keV and the expected ratio must lie in an additional noise source, e.g. remaining fringes, grating instability or grating defects.

From the determined minimum refraction angle a specific dynamic of the setup can be defined. This dynamic D in the taken projections can be expressed by the ratio of the maximum detectable refraction angle without phase-wrapping, correspondent to a signal of π, to the angle α_{min}.

$$D = \frac{\alpha_{max}}{\alpha_{min}} = \frac{p}{2d} \cdot \frac{1}{\alpha_{min}} \tag{5.3}$$

Table 5.4 list the values for the setup dynamic for the specific setups retrieved from their sensitivity values.

Table 5.4: Dynamic of the different setup configurations given by equation 5.4.

Energy	SG	DG_1	DG_3
20 keV	86	106	70
40 keV	72	106	103

Reported sensitivity values for grating-based phase-contrast at other synchrotron radiation facilities are 67 *nrad* at the Swiss Light Source (TOMCAT) [78] and 14 *nrad* at ESRF (ID19) [98]. Although these are well below the obtained values, the reference values where obtained with a larger pixel size, larger propagation distance and more phase steps[1,2].

5.4 Quantitative Evaluation

For each material, the mean value of the retrieved δ-values and the signal to noise ratio (SNR) were calculated. The SNR value is conventionally calculated by taking the average over the signal and the standard deviation of an uniform background. However, the noise within the areas of the materials is strongly dependent on their properties. Especially the scattering caused by the sample has strong effects as it directly negatively influences the visibility which in return deteriorates the image quality. Therefore the noise values were taken from within the material instead of the background. This approach is applicable, because the object composed of homogeneous materials where the noise level is not compromised by inhomogeneity features from within the object.

For all tomographic reconstructions three slices equally separated were analysed. On each slice the mean value of each material and the correspondent noise value was determined in a square field in the middle of the material. Each area was 60×60 pixels large. This relatively small area had to be chosen with respect to the small diameter of the Aluminium rod.

Table 5.5 list the results from the measurements at 20 *keV*. The retrieved δ-

---

[1]TOMCAT: *grating period = 2 μm, pixel size = 7.4x7.4 μm², distance = 121 mm, steps = 5*
[2]ID19: *grating period = 2 μm, pixel size = 15.7x15.7 μm², distance = 361 mm, steps = 7*

Table 5.5: Signal quality comparison for a single-grating (SG) and a double-grating interferometer at the first (DG_1) and at the third (DG_3) fractional Talbot distance. Mean values of material dependent δ-values and related signal to noise ratios for measurements at 20 keV are given. The deviation from the literature values $\Delta\delta$ gives the accuracy of the retrieved values.

	Material	$\delta[10^{-7}]$	SNR	$\Delta\delta[\%]$	Literature
	PMMA	6.26	79.62	-6.1	6.67
	PA 6.6	6.26	75.10	-3.1	6.46
SG	Mg	8.50	109.13	-5.0	8.95
	PCTFE	9.75	123.11	-8.9	10.70
	PTFE	10.50	134.52	-4.5	11.00
	Al	12.56	119.65	-7.6	13.60
	PMMA	6.75	119.80	$+1.2$	6.67
	PA 6.6	6.65	138.59	$+2.9$	6.46
DG_1	Mg	8.85	167.82	-1.1	8.95
	PCTFE	10.19	171.75	-4.8	10.70
	PTFE	10.96	184.75	-0.4	11.00
	Al	12.81	255.40	-5.8	13.60
	PMMA	6.02	93.90	-9.7	6.67
	PA 6.6	5.80	105.79	-10.2	6.46
DG_3	Mg	8.01	152.13	-10.5	8.95
	PCTFE	9.45	181.58	-11.7	10.70
	PTFE	9.73	217.39	-11.5	11.00
	Al	11.64	242.74	-14.4	13.60

values, the SNR, and the deviation from the literature values are given. The table shows that both types of the interferometer retrieve values, that differ from the literature values in the range from 5% up to more than 10% for the more dense materials. For all materials the best results of the mean δ-value are obtained by the double-grating interferometer at the first fractional Talbot distance (DG_1). The values from the double-grating setup at the third fractional Talbot distance (DG_3) and from the single-grating setup (SG) have a relative large deviation from the theoretical values. One possible reason for this lies in the phase-wrapping artefacts, which occur at the borders between the different materials (sec. 5.4). Phase-wrapping in the single projections not only affects the reconstruction by
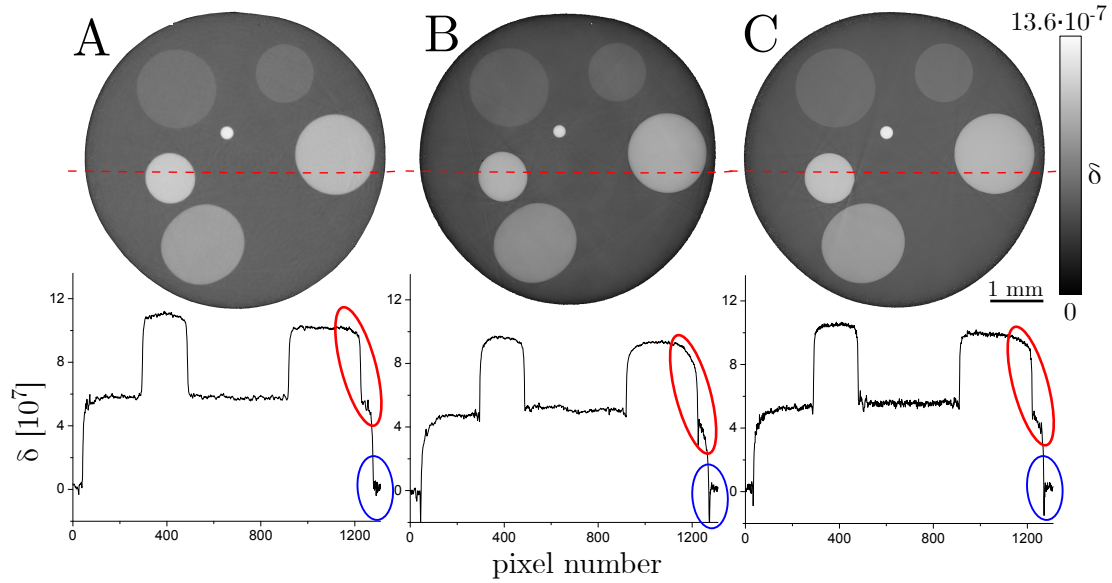
Figure 5.2: Reconstructed slices and the corresponding line profiles (red dashed line) of the test phantom at the different setups. A: Double-grating setup at the first fraction Talbot distance (DG_1). B: Double-grating setup at the third fraction Talbot distance (DG_3). C: Single-grating setup at 40 *cm* propagation distance (SG). The comparison of the three measurements shows strong corruption for DG_3 and SG as consequence of phase-wrapping. At the border of the sample strong negative values occur (marked in blue). The resulting cupping-artefact is easily recognised by the rounded edged (marked in red).

generating streak artefacts tangential to the materials border, but also leading to cupping artefacts, that disturb the whole grey-level distribution, which are similar to artefacts occurring at region-of-interest measurements for conventional μCT [99].

A two dimensional cross section of the reconstructed volumes is presented in figure 5.2. The artefacts from phase-wrapping can be detected at the sample border and appears like a bell-shaped envelope on the reconstructed slices. This envelope induces a false grey level distribution of the sample, especially obvious in the border region.

To have a systematic comparison of the quantitative results, the experiment was repeated with a slightly different phantom at a photon energy of 40 *keV*. At this energy the corruption from phase-wrapping is negligible for the SG measurement, which can be seen from the obtained $\Delta\delta$-values and the increased SNR listed in

Table 5.6: Signal quality comparison for a single-grating (SG) and a double-grating interferometer at the first (DG_1) and at the third (DG_3) fractional Talbot distance. Mean values of material dependent δ-values and related signal to noise ratios for measurements at 40 keV are given. The deviation from the literature values $\Delta\delta$ gives the accuracy of the retrieved values.

	Material	$\delta[10^{-7}]$	SNR	$\Delta\delta[\%]$	Literature
SG	PMMA	1.65	89.23	-2.4	1.67
	Mg	2.22	100.42	-0.4	2.23
	PCTFE	2.67	148.45	$+0.4$	2.66
	PTFE	2.69	140.89	-1.8	2.74
	Al	3.34	180.10	-1.2	3.38
	Ti	5.32	218.43	-1.1	5.38
DG_1	PMMA	1.69	131.74	$+1.2$	1.67
	Mg	2.25	162.44	$+0.9$	2.23
	PCTFE	2.66	166.39	±0.0	2.66
	PTFE	2.80	180.43	$+2.2$	2.74
	Al	3.43	144.10	$+1.5$	3.38
	Ti	5.12	196.37	-4.8	5.38
DG_3	PMMA	1.60	117.23	-4.2	1.67
	Mg	2.08	137.76	-6.7	2.23
	PCTFE	2.53	165.76	-4.9	2.66
	PTFE	2.64	153.45	-3.6	2.74
	Al	3.17	168.73	-6.2	3.38
	Ti	4.80	154.60	-10.8	5.38

table 5.6. The measurement using the DG_1 again show very good agreement to the literature values and slightly improved SNR values to those from the same measurement at 20 keV. The δ-values retrieved from the DG_1 measurement are again in very good agreement with the literature values and the SNR values are comparable to those from the 20 keV measurement. For the DG_3 measurement a strong improvement in the accuracy of the δ values is recognisable, although the deviation from the literature values is still strong. This indicates that the measurement still suffers from phase-wrapping and can be proven by the two dimensional cross section shown in figure 5.3.
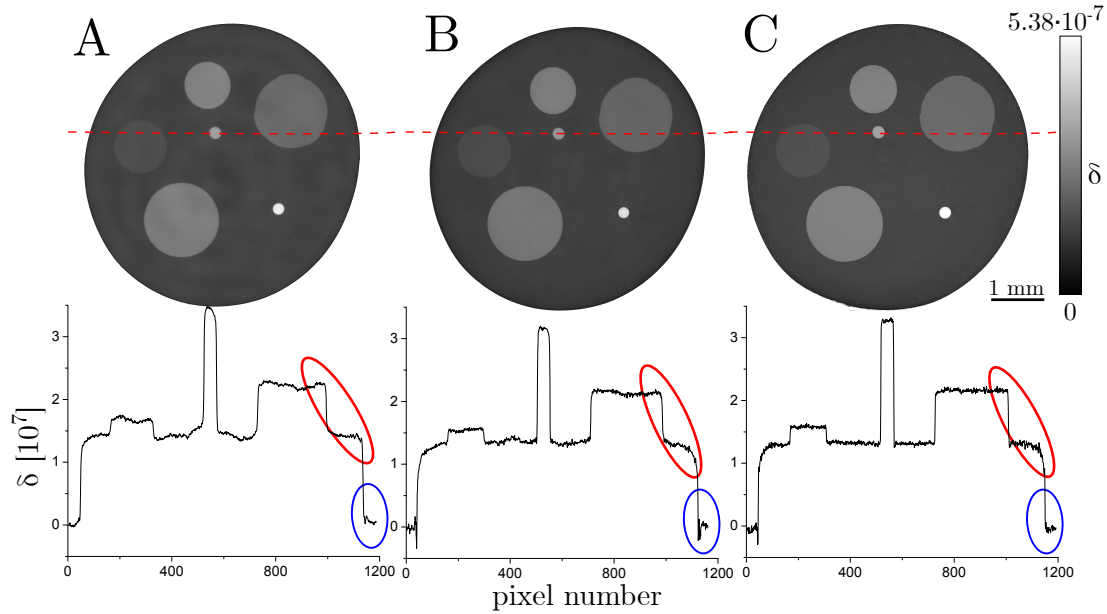
Figure 5.3: Reconstructed slices and line profiles of the test phantom at the different setups. A: Double-grating setup at the first fraction Talbot distance (DG_1). B: Double-grating setup at the third fraction Talbot distance (DG_3). C: Single-grating setup at 80 cm propagation distance (SG). As for the measurement at 20 keV, DG_3 is still affected by phase-wrapping and according cupping artefacts. SG also shows slight indication for phase-wrapping but seem to be not affected by cupping, as the profile shows sharp edges between the materials. The wavy background of DG_1 is a consequence of not matching reference projections and will be discussed in section 5.7.
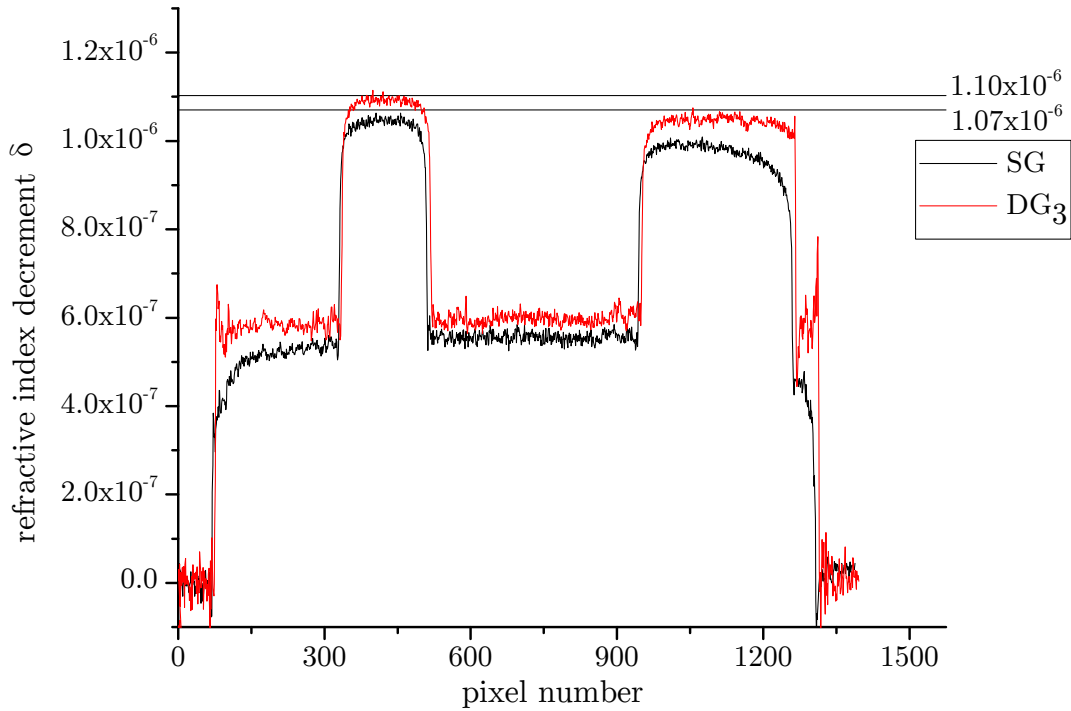
Unwrapping

The previous findings have shown that phase-wrapping is crucial for the quality of a DPC measurement. One obvious corruption, directly visible from table 5.5, is that obtained quantitative values of the dataset are not accurate any more. Due to the phase wrapping, the quantitative results give too low values, dependent on the intensity of the wrapping. The morphology of this phase-wrapping artefact is analog to the cupping artefacts retrieved from beam-hardening or local tomography [99]. A common solution to avoid phase-wrapping occurring from the strong phase-shift difference between sample surface and surrounding air is to perform the experiment with the sample immersed in some liquid with a similar refractive index (usually water). Although this method is adequate to avoid phase-wrapping at the sample surface it has no influence on wrapping events inside the sample.

Table 5.7: Signal comparison of the two measurements at 20 keV that have shown strong phase-wrapping after a unwrapping algorithm was applied.

|	Material	$\delta[10^{-7}]$	SNR	$\Delta\delta[\%]$	Literature
	PMMA	6.79	61.41	$+0.4$	6.67
	PA 6.6	6.76	73.28	$+4.6$	6.46
SG	Mg	9.02	91.41	$+0.8$	8.95
	PCTFE	10.29	123.11	-3.8	10.70
	PTFE	10.96	123.86	-0.4	11.00
	Al	12.97	127.17	-4.6	13.60
	PMMA	6.62	56.53	-0.7	6.67
	PA 6.6	6.37	78.27	-1.4	6.46
DG$_3$	Mg	8.71	117.17	-2.7	8.95
	PCTFE	10.25	131.70	-4.2	10.70
	PTFE	10.44	169,93	-5.1	11.00
	Al	12.35	157.33	-9.2	13.60

Dependent on the sample itself it might also not be applicable to immerse the sample. To solve the problem and correct for phase-wrapping during the image processing various different unwrapping techniques were developed [100]. All these algorithms are user determined or sample dominated. Thus, there is no universal and objective routine to remove or alleviate the phase-wrapping. Nevertheless the suitability of unwrapping was checked for the datasets datasets SG and DG_3 from the measurements at 20 keV. The applied algorithm is an iterative approach based on the comparison of the propagation-based signal and the differential phase contrast and evaluated the resulting reconstruction. A scheme of the algorithm can be found in the appendix E. Table 5.7 gives the quantitative values for the phantom materials. Compared to the original data, a strong improvement in the accuracy after unwrapping can be seen but meanwhile a decrease in the signal to noise ratio also occurs. Figure 5.4 shows that the unwrapping procedure helps to remove the cupping artefacts on the reconstruction but also brings additional streak artefact. From overcompensation and false unwrapping of not corrupted pixels, these streak artefacts can be the source of the decreased signal-to-noise ratio.

Although the algorithm used here for phase-unwrapping obviously are able to re-

Figure 5.4: The profile of the unwrapped profile shows the significant improvement of the data quality due to the removed cupping artefact. The improvement is clearly recognised by more accurate δ-values and sharp edges.

store correct quantitative values and remove the cupping artefacts, it is not applicable as universal algorithm available that can be used without manual parameter adjustment. Therefore it is necessary to directly avoid the occurrence of phase-wrapping in order to have a reliable experiment for large measurement series. Not only for its applicability but also for a precise measurement, the occurrence of phase wrapping should be avoided. Easiest solution to achieve a wrapping-free measurement is by choosing an adequate high energy. A higher photon energy can effectively decrease the phase-wrapping, which can be seen from the experiment results. First, the comparison of the unwrapped dataset from the single-grating setup with the measurement at 40 keV shows a better signal-to-noise ratio for the higher energy. Second, the comparison of both measurements at the first fractional Talbot-distance for the double-grating setup show a comparable signal-to-noise ratio, even for the very light materials (PMMA and Magnesium).
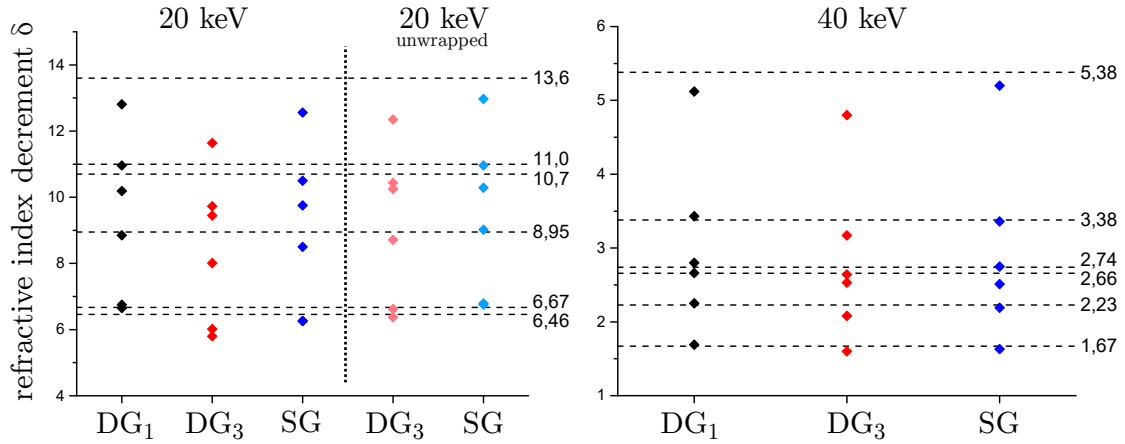
Figure 5.5: Plotted δ-values from the measurements with single- and double-grating interferometer at 20 keV and 40 keV. DG_1: Double-grating setup at first fractional Talbot-distance. DG_3: Double-grating setup at third fractional Talbot-distance. SG: Single-grating setup. The dotted horizontal lines give the literature values of the phantom materials. For 20 keV only DG_1 directly gives correct δ-values. After unwrapping the values from SG are comparable to DG_1 while the values from DG_3 still have a large deviation. At 40 keV the values from DG_1 and SG are in good agreement with the literature values while the values from DG_3 are systematically lower.

Summary

The analysis of the quantitative δ-values have shown, that both setup types are suitable to retrieve phase-contrast signals in very good agreement with the literature values. Nevertheless, the investigation has also shown that the obtained data has to be free of phase-wrapping artefacts in order to obtain reliable results. Unwrapping algorithms are in general suitable to counter the negative effects of phase-wrapping, but with strong restrictions. A comparison of all retrieved δ-values is shown in figure 5.5. For those datasets, which are almost unaffected by phase-wrapping (SG and DG_1 at 40 keV) the comparison shows that the accuracy of the δ-values is comparable. The values obtained at 20 keV also show a good agreement between the literature values and the values retrieved by the DG_1 and the SG after applying the unwrapping algorithm. For the DG_3 on the other hand the algorithm results are not satisfying.

The comparison of the SNR-values for the different measurements indicates that the double-grating interferometers provide better SNR and hence are less affected
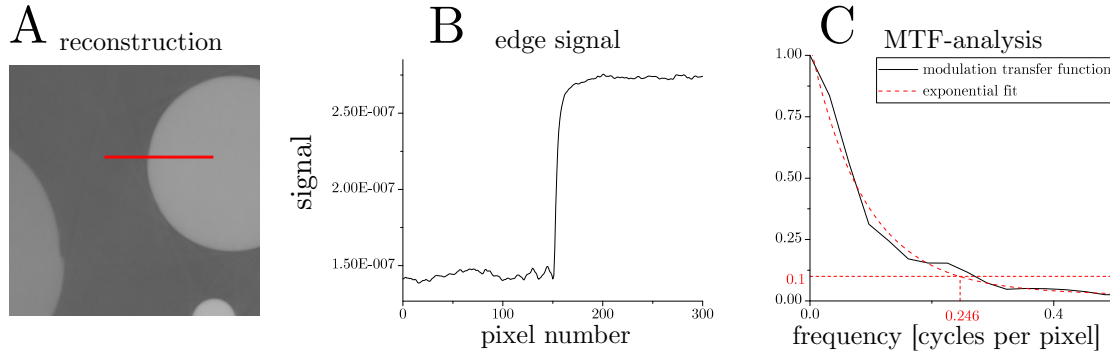
Figure 5.6: For each material in the phantoms a line profile starting in the base material and ending in the evaluated material is selected (A+B). The MTF-analysis of the line profile (C) is used to determine the resolution. The cut-off frequency is chosen where the the MTF-value falls below 10%.

by high frequent noise. This finding is contrary to the expectations out of section 3.3, that states that the DG_3 should give the highest sensitivity and therefore the best SNR among the tested setups, followed by the SG. However, taken into account the low visibility value of the single-grating setup of only 8% at 20 keV and 6% at 40 keV, the retrieved values seem to exceed the expectations.

5.5 Spatial Resolution

The measurement of the spatial resolution is always dependent on the experimental parameters and different setup conditions require different test pattern. A typical test pattern for micro-tomography such as a Siemens star is not suitable for grating-based phase contrast as previously discussed. Another well established method to determine the spatial resolution is the analysis of a sharp edge by exploiting the modulation transfer function (MTF). For grating-based phase-contrast the analogy to a sharp edge can be realised using the continuous slope of a wedge that will produce a step function [101]. However, to ensure that all related factors influencing the resolution are taken into account, the analysis was performed on the three-dimensional datasets. The structure of the phantom with its well separated materials allows to determine the spatial resolution using the well defined interface between the individual rods and the filling material. This interface represents a step function that can be analysed via an MTF, similar to the projection of a wedge.

Table 5.8: Spatial resolution for different phantom materials, determined by analysing the modulation transfer function. Values are given in μm.

	Material	SG	DG_1	DG_3
20 keV	PA	4.65	10.39	13.19
	PMMA	4.84	10.76	11.43
	Mg	5.35	10.13	18.32
	PCTFE	8.60	10.91	16.78
	PTFE	7.84	10.81	16.00
	Al	6.59	11.82	19.20
40 keV	PMMA	3.88	—[1]	5.82
	Mg	4.76	14.71	7.19
	PCTFE	5.22	16.20	8.05
	PTFE	5.22	16.00	7.95
	Al	5.77	15.80	9.41
	Ti	6.04	14.71	5.02[2]

Figure 5.6 illustrates the analysis of the spatial resolution. For each rod of the test phantom, a line starting in the filling material and ending in the corresponding material was taken as source for the MTF analysis. For a perfect spatial resolution this line would represent a step function. In the acquired experimental data, the edge of the material is always represented as slope, where a steeper slope corresponds to a higher spatial resolution. The MTF can be derived from the linear function and a certain cut-off frequency was taken to determine the spatial resolution using the voxel edge length. The Rayleigh criteria states that the resolution limit is reached at an 80% loss in peak to peak contrast [102]. This is according to a modulation transfer value of $\approx 10\%$ [90, 89]. Therefore the cut-off frequency to define the spatial resolution was selected at the MTF value of 10%. From the simulations, a strong dependency of the spatial resolution on the investigated material is expected. Therefore, the resolution was determined separately for each material present in the phantom.

The results of the analysis are listed in table 5.8. All calculated results show,

---

[1]MTF-calculation did not succeed due to image artefacts and background noise

[2]Due to phase-wrapping at the border of the Titanium rod the edge function is corrupted, leading to a false determined value.

that the resolution is strongly influenced by the examined material. The highest resolution can be achieved for the lightest material (PMMA & PA 6.6). On the contrary the materials with the highest density (Al & Ti) give the lowest resolution. A better resolution of the single-grating setup is also proven in this table. Using the single-grating interferometer the resolution for every material is well below 10 μm, while three of four measurements with a double-grating setup cannot reach a visibility below 10 μm. Only the DG_3 measurement at 40 keV could achieve a resolution below 10 μm and also shows the characteristic material dependency. A reason for the coarse resolution of the DG-setups is supposed to lie in the presence of low-frequent image artefacts, which are present across the whole reconstruction. This will be further discussed in section 5.7. It is noticeable in the SG results, that a higher energy provides a better spatial resolution. This can be easily explained by the ratio of increased distance (factor of 2) to decreased δ-value (factor of 4) accompanied by a smaller refraction angle. This causes a reduced blurring caused by signal and therefore the better resolution.

Summary

The results indicate that, although the beamline setup plays a big role for the resolution, the reachable spatial resolution is mainly determined by the investigated material itself. For the lightest materials a resolution even below 5 μm could be reached. Although the phase-grating period has an strong influence on the spatial resolution due to its influence on the propagation distance, the resolution is not strictly limited by its period as it is reported for the double-grating setup [40].

The presented investigation show that a single-grating interferometer allows for higher spatial resolution as the double-grating interferometer. However, it is most likely that the maximum reachable resolution for the double-grating interferometer lies within the same range, but is not accessible due to a high level of instability. The results also show that for a higher energy a better resolution can be reached, but which in return will come with a lower signal.

The superior resolution achieved by the single-grating setup could also be shown for biological samples, published by Thalmann et. al. [92]. Here, also a resolution of roughly 5 μm was reached, although a smaller grating period was chosen.
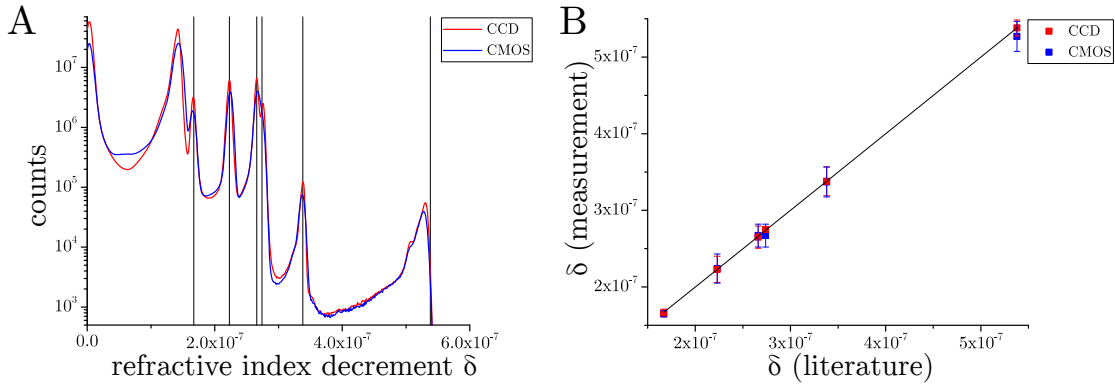
Figure 5.7: A: Histogram of a selected slice of the whole volume.
B: Visualization of the peak positions of the single materials as comparison to
the literature values (straight line). The error bars indicate the width of the
individual peaks. Both plots show the advantage of using the CCD-system.
Using the CMOS-based system the peaks for PCTFE and PTFE cannot be
distinguished.

5.6 Influence of Camera System

As mentioned previously, mainly two strategies can be used to improve the ac-
quisition speed of a grating interferometer setup. The single-shot approach (sec.
2.3.4), which avoids the necessity of recording a stepping series and the appli-
cation of a fast camera system. The single-shot method is easily applicable as
no additional equipment or configuration is needed. However, it comes with a
resolution limitation determined by the grating period, which is contrary to the
aim to establish a high-resolution grating-based phase-contrast setup. Another
alternative relies on a camera that allows for a very high frame rate, which in
contrary comes with a much lower dynamic range. To test for the influence of
this reduced dynamic range for gbDPC, measurements with a CCD-based camera
and a CMOS-camera were compared. The CCD-sensor shows a higher dynamic
range and photon sensitivity, whereas the CMOS-sensor gives the benefit of a
much shorter readout time and a smaller pixel size (sec. 4.2).

Both tomography scans were obtained at the P07 beamline with the same exper-
imental setup just by replacing the camera itself. This ensures to have all other
experimental parameters kept exactly the same.

The retrieved phase projections were binned by a factor of two in case for the CCD

Table 5.9: Peak positions retrieved from the data histograms presented in figure 5.7. The full width at half maximum is given to compare the noise.

Material	Literature	CCD Peak / FWHM $[10^{-7}]$	CMOS Peak / FWHM $[10^{-7}]$
PMMA	1.67	1.67 / 0.09	1.63 / 0.08
Mg	2.23	2.20 / 0.17	2.19 / 0.14
PCTFE	2.66	2.64 / 0.19	2.65 / 0.23[1]
PTFE	2.74	2.76 / 0.07	2.65 / 0.23[1]
Al	3.38	3.37 / −	3.32 / −
Ti	5.38	5.27 / −	5.30 / −

camera and by a factor of four in case of the CMOS camera to gain a comparable effective pixel size. To analyse the performance of the two measurements not only the obtained mean δ-values for the phantom materials, but also the whole histograms are compared. The results are plotted in figure 5.7. In both cases the histogram peaks are in very good accordance with the literature values (marked by vertical lines).

Figure 5.7 (right) and table 5.9 show that the mean values of the different materials in both measurements are in good agreement with the literature values and also to each other. A main difference is observed for the $PCTFE$ and $PTFE$ rods, which can be clearly distinguished for the CCD-measurement but only result in a joint peak for the CMOS-measurement. The relative strong deviation for the Titanium values is mainly a consequence of the strong signal. This strong signal causes a significant blurring at the edge of the rod which results in a lowered mean value. Nevertheless, this effect is independent of the used camera system.

By an exact comparison of the mean values and the histogram peaks from the two measurements, an advantage from using the CCD-camera is observed. The higher dynamic range clearly gives a benefit for the distinction between materials with very similar refractive index.

However, the acquisition time for the CMOS-based measurements could be performed with roughly a quarter of the acquisition time of the CCD-measurement.

---

[1]PCTFE and PTFE share same peak
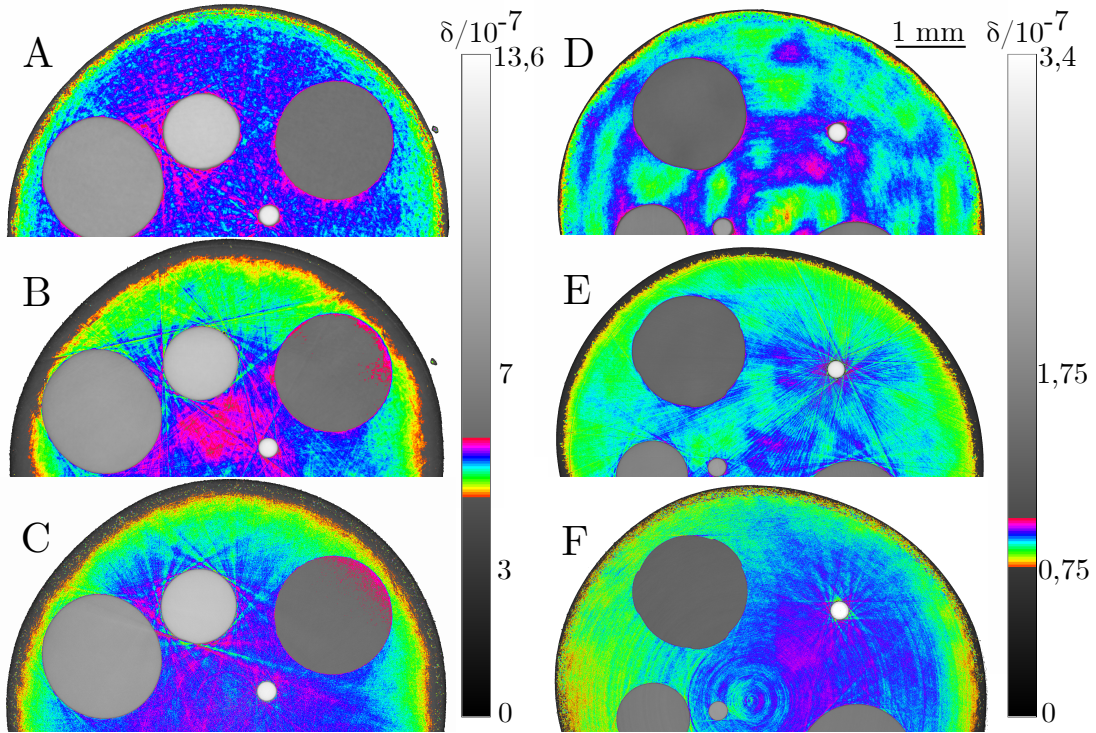
Figure 5.8: Comparison of reconstructed slices measured at 20 keV (A-C) and at 40 keV (D-F) for the three different setups. The comparison shows significant long scale artefacts for the DG_1 measurements (D). The DG_3 measurements do not suffer that strongly from low frequent artefacts, but are strongly affected by streak artefacts at the materials borders. The SG measurements show less streak artefacts than the DG_3 measurements, while long scale artefacts are absent. The base material of the sample is visualised in false colors for better visualisation of the artefacts.

For most applications this decrease in needed acquisition time is an invaluable advantage whereas the high dynamic of the CCD is only essential in rare cases.

5.7 Qualitative Evaluation

The qualitative evaluation is based on the image quality of the reconstructed slices, that is hard to be expressed by quantitative values like the signal to noise ratio or the spatial resolution. It mainly comprises of a subjective interpretation of the image quality regarding the homogeneity of the background and the occurrence of streak artefacts. For a lot of applications these two characteristics are an

important quality factor. An uniform background for example is an essential property for automatic image segmentation or visualization applications. While an inhomogeneous background affects the whole image, streak artefact are localized artefact. Although they do not affect the complete image plain, their presence can cover valuable information from small features.

Figure 5.8 shows reconstructed slices for the different setups at both investigated energies. The DG_1 measurements show a significant wavy background. The reason for this are remaining Morié-fringes remaining in the projection after flat-field correction. These remaining fringes and the resulting wavy background are a clear evidence for a unstable setup. Due to the use of two gratings and the signal being dependent on their relative position to each other, this setup is much more vulnerable to instabilities. As the created Morié-pattern is strongly affected by any kind of changing grating alignment the whole instrument is very sensitive to outside influences e.g. vibrations, air convection and temperature.

5.8 Summary

The experiments performed with the three different setups have proven that all setups produce accurate images of the examined samples, on the condition that the reconstruction is not corrupted by strong phase-wrapping artefacts. Phase-wrapping can result in a strong mismatch between the retrieved values and the literature values. The comparison of the signal to noise ratios have shown an advantage of the double-grating interferometer. The larger propagation distance of the DG_3-setup theoretically results in a clearly better SNR-value than for the DG_1-setup. However, the occurrence of wrapping artefacts deteriorates the image quality, which in return decreases the SNR-values to about the same level as for the DG_1-setup. The SNR values for the SG-setup, which were expected to be between the values for the DG_1 and DG_3 setups from the simulations, are very low. This can be explained by the very low visibility reached for this setup.

Both the mismatch of the δ-values and the SNR values below the expectations for the DG_3 setup is mainly caused by the phase-wrapping artefacts. Although an applied unwrapping algorithm can effectively remove most of the artefacts, the resulting image quality does not reach the same quality as an original uncorrupted

reconstruction.

The resolution achieved with the single-grating setup exceeds the resolution with the double-grating interferometer for all measurements. With a spatial resolution down to 4 μm this type of interferometer gives an excellent performance, where the actual spatial resolution is dependent on the investigated material. For lighter materials the resolution is in general higher and also can be improved with a higher energy. This proves again, that the achievable resolutions is strongly dependent on the materials properties rather than the experimental setup parameters.

With the double-grating interferometer a spatial resolution on the same length scale could be obtained, but the investigations have shown that this is highly dependent on the presence of reconstruction artefacts. Not merely wrapping artefacts, but rather instabilities of the interferometer like small grating vibrations have a major impact on the achievable spatial resolution. These instabilities also can cause a strongly disturbed background which is a big disadvantage for automatic image processing routines (e.g. segmentation). Due to the presence of only one grating and the larger period, the single grating interferometer is less influenced by this effect. Regarding the camera, the results have shown that the used type of camera sensor, more precisely the dynamic range of the camera has only little effect on the image quality. The drawback of reduced dynamic will be acceptable for most applications in view of the fact that the required acquisition time is dramatically reduced.

6 Application Examples

This chapter will present different user experiments that successfully were performed using the single-grating interferometer system developed during this work. The examples show the usability in a wide range of energy and for different kinds of material. All presented single-grating measurements were performed using the same 10 μm-pitch phase grating with a structure height of 10.4 μm (design energy: 60 keV).

6.1 Water Transport in Concrete

One of the very first user experiments using the single-grating interferometer presented here was performed by Fei Yang et al.[1][103] at the beamline P07. Goal of the research was to identify the water distribution within concrete and limestone samples at different drying states. Main condition of the experiment was to distinguish between water and air filled pores without use of a contrast agent. The measurements were performed at a photon energy of 55 keV and a propagation distance of 80 cm. Due to the good sensitivity and the high spatial resolution of the single-grating setup it was possible to easily differentiate between air filled and water filled pores with a spatial resolution of 5 μm.

Figure 6.1 shows an exemplary result of these measurements. The pores within the samples could be identified and classified on the basis of their grey value in the reconstructed 3-D volume. By comparison of the sample reconstruction at different drying states the individual pores which lost their water content were easily recognised. In figure 6.1 those pores are marked in blue. Pores which were air-filled at both measurements are marked in green. Some areas are marked in red, indicating water gain in-between the two measurements.

---

[1]Swiss Federal Laboratories for Materials Science and Technology (EMPA), Überlandstrasse 129, 8600 Dübendorf, Switzerland
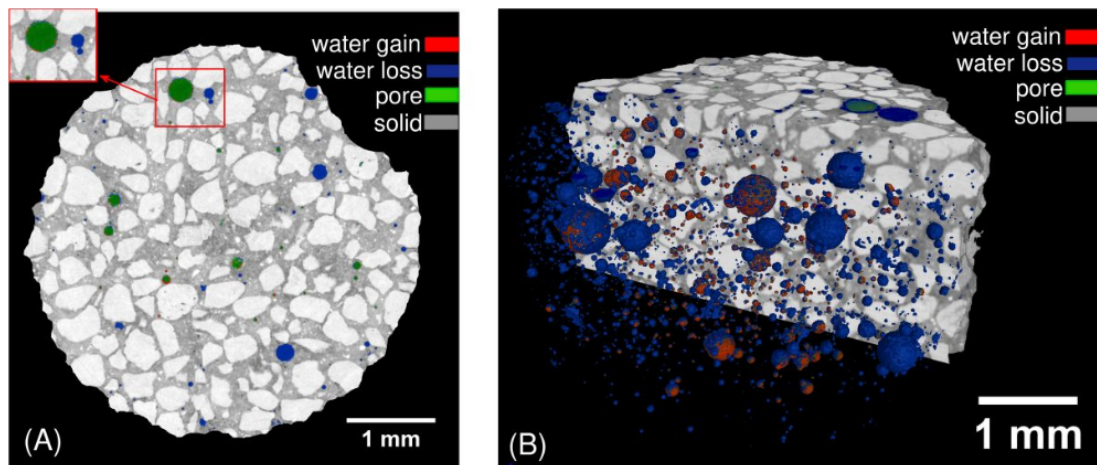
Figure 6.1: Water distribution in concrete sample. A: shows a slice of the reconstructed 3D-volume. B: shows a 3-D rendering of the same volume. For better visualisation of the pores only a part of the concrete matrix is shown in the rendering. In both images different types of pores are marked in distinct colors. Pores, that were already air-filled before starting the drying process are marked in green, while those pores which dried during the experiment are marked in blue. Some regions, marked in red, have gained water during the experiment. Images are taken from F. Yang et al.[103]

6.2 Calcified Coronary Arteries

The results on human coronary arteries presented here, were achieved within the beamtime of Marzia Buscema[2]. Core of the project is to investigate the anatomical changes in terms of lumen morphology of constricted arteries[104]. Within the project, human coronary arteries were examined using both single- and double-grating interferometers.

The comparison between the single- and double-grating measurement can be used to directly compare the image quality for both setups on the same sample, as shown in Figure 6.2. Both measurements were performed at 45 keV and a propagation distance of 80 cm (SG) respectively 31.4 cm (DG), corresponding to the third fractional Talbot-distance, at the beamline P07. The comparison focuses on the strong calcification within the coronary artery for better visualisation of small features within the calcification.

---

[2]Biomaterials Science Center, University of Basel, Gewerbestrasse 14, 4123 Allschwil, Switzerland
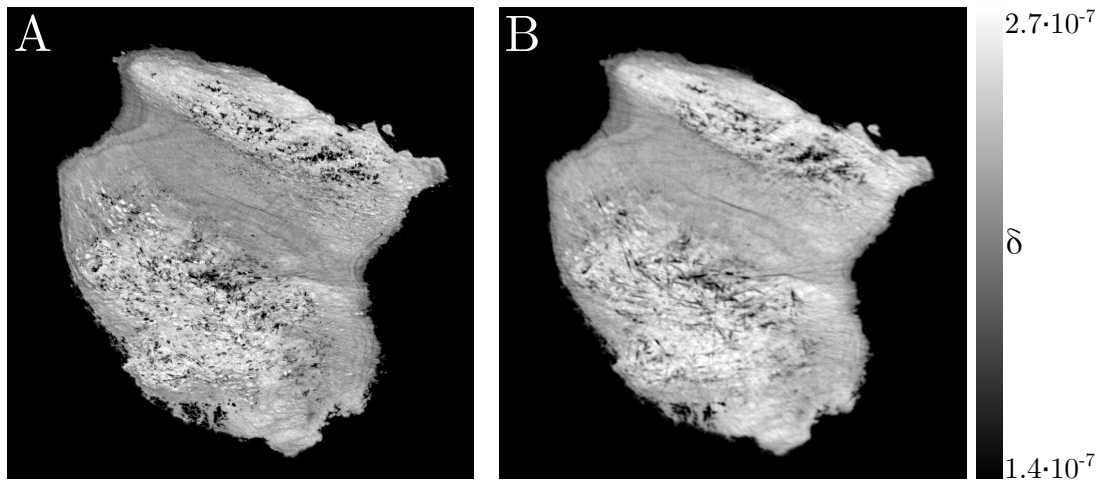
Figure 6.2: Comparison of single-grating measurement (A) and double-grating measurement (B) of the same sample. The direct comparison of the two methods clearly shows the superior image quality of the single-grating setup. The fine structure within the calcification becomes much better visible in the single-grating measurement, while the double-grating measurement is affected by stronger image blurring.

The chemical composition of the calcification in arteries has been identified to be identical to hydroxyapatite ($Ca_{10}[PO_4]_6[OH]_2$) [105]. Pure hydroxyapatite would result in a refractive index decrement δ of $3.2 \cdot 10^{-7}$. Both reconstructions give similar $\delta-$values in the range between $1.4 \cdot 10^{-7}$ and $2.7 \cdot 10^{-7}$. These lower values are reasonable considering that the hydroxyapatite will not be deposited as pure substance, but as mixture with other components, such as soft plaque [106].

Both reconstructions give the same information about the electron density and its distribution. Nevertheless, the reconstruction from the single-grating measurement shows less image blurring and therefore finer features become visible. With the focus on the spatial resolution, the single-grating setup clearly outperforms the double-grating setup.
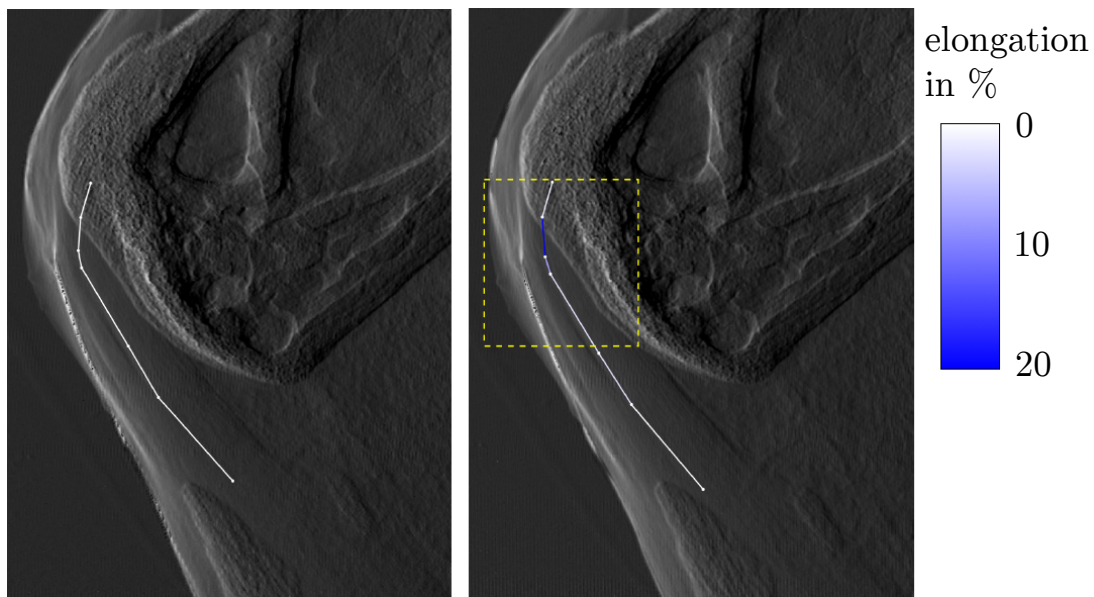
Figure 6.3: Murine Achilles tendon insertion in the relaxed (left) and deformed state (right). The color of the lines corresponds to the relative unidirectional strain between their end points. Figure supplied by J. Sartori.

6.3 Deformation of the Tendon-Bone Insertion

At the beamline P05, Julian Sartori et al.[3] performed the first in-situ experiment in combination with the developed single-grating interferometer.

The project is dealing with the deformation of the tendon-bone insertion under defined forces. For this purpose a series of DPC-based projections were acquired while having a defined force applied on the Achilles tendon. At certain intervals the series of projections was interrupted to perform a full tomography of the current deformation state for later 3D-investigations. The measurements were performed at a photon energy of 23 keV. For higher resolution and a reduction of phase-wrapping artefacts the propagation distance was set to 20 cm, which corresponds to a quarter of the first fractional Talbot distance.

The most recent results, presented in figure 6.3, show the deformation of the tendon with applied force by means of its elongation in comparison to the relaxed state. The used setup configuration allows to have reasonable contrast between

---

[3]Institute of Systematic Zoology and Evolutionary Biology, Friedrich-Schiller-University Jena, Ebertstrasse 1, 07743 Jena, Germany

the tendon and the surrounding tissue to measure its exact shape.

Although this is a still ongoing project, the results so far show very well the operational capability of the singe-grating interferometer for in-situ measurements. This suggests the assumption that further enhancement of the acquisition scheme, resulting in a shorter acquisition time, will allow this interferometer to be used for in-situ tomography experiments.

For further experiments a mixed acquisition scheme where the projections are taken at a larger propagation distance, while the tomography scans are kept a the shorter distance is conceivable due to the high flexibility of the setup which allows an automatic and fast adjustment of the propagation distance. This would allow to enhance the contrast between tendon and surrounding tissue for the projections. The wrapping artefacts which would occur, would be localised at the bone and not affect the soft tissue contrast. For the tomography scans the propagation distance has to be kept short enough to avoid phase-wrapping as they would corrupt the whole volume.

6.4 Mammalian Teeth under Pressure

The last user experiment presented here was performed by Ellen Schulz-Kornas et al.[4]. To investigate the deformation of the periodontal apparatus, measurements of a mammalian jaw segment with a certain force applied are planned. To investigate the usability of grating-based phase-contrast for these experiments an exemplary tomography of such a jaw segment has been performed.

Figure 6.4 demonstrates the enormous range in contrast, that becomes available using grating-based phase contrast. Different types of soft tissue, bone and teeth are clearly distinguishable in the reconstruction of the jaw segment. Especially the thin fibres connecting the teeth to the bone are nicely visible. These fibres have a thickness of only a few micrometer and therefore give a nice demonstration of the high spatial resolution achievable using a single-grating interferometer.

---

[4]Max Planck Institute for Evolutionary Anthropology, Deutscher Platz 6, 04103 Leipzig, Germany
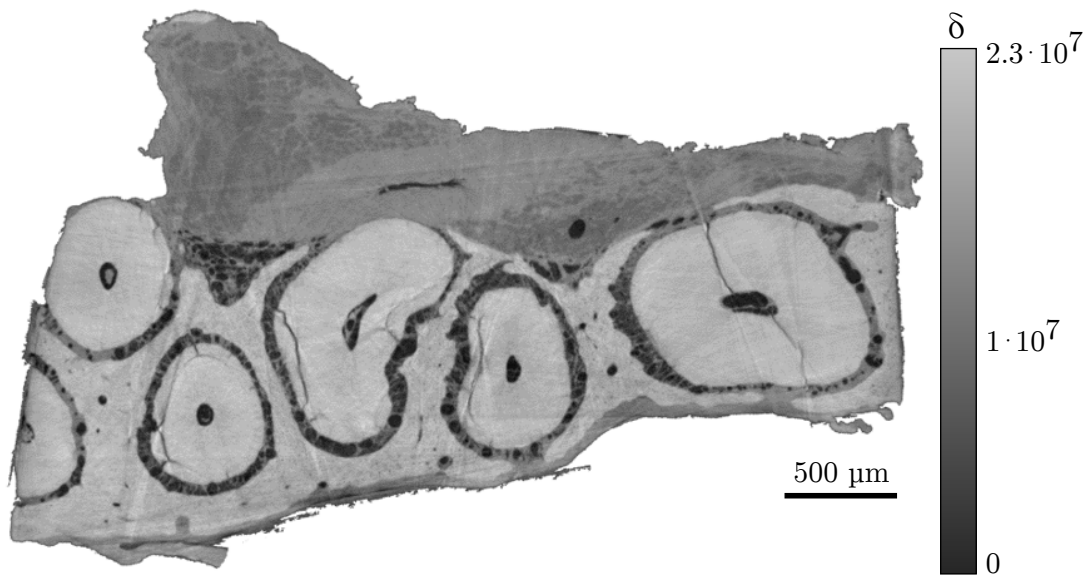
Figure 6.4: Part of a mammalian jaw. Teeth, bone, gum, and perforating fibres are clearly distinguishable, using phase-contrast tomography. Especially the thin fibres filling the gap between bone and teeth are of great interest.

6.5 Summary

The presented user experiments show convincingly that the developed interferometers successfully became an established user experiment. With focus on the single-grating interferometer these experiments demonstrate the enormous potential of this technique for tomographic measurements with a high-spatial resolution and a large contrast range. Moreover the experiments show that in-situ measurements with advanced sample environments can be combined with the developed grating interferometer.

7 Conclusion and Outlook

The comparison between the simulations and experiments are most widely in a very good agreement. In this chapter the main findings and results will be summarised. The final conclusion and an outlook will be given at the end of this chapter

7.1 Summary

Image Quality

The simulations predicted the occurrence of streak artefacts and cupping artefacts due to phase-wrapping. These predictions could be proved by the experiments. Also, the artefact intensity is related to the sensitivity of the setup. By using a less sensitive interferometer setup or measuring at an increased photon energy will lower the risk of unwanted artefacts, but on the other side is leading to a lower contrast within the sample.

The inhomogeneous background of the double-grating setup reconstructions refers to an instability of the grating setup due to vibrations or drift of the gratings. Simulations taking care of an unstable grating position gave a similar disturbance of the reconstruction background and moreover have shown, that a single-grating setup is much less vulnerable to such an instability. This clearly indicates the high reliability and robustness of a single-grating interferometer.

Signal to Noise Ratio (SNR)

SNR-values obtained from the simulations clearly stated an advantage of the single-grating interferometer against the both double-grating interferometers. The expected height performance of the double-grating interferometer at the third frac-

tional Talbot distance could not be observed, as the reconstructions are strongly corrupted by image artefacts.

Although the results of the simulation results do match the experimental findings for the DG_3-setup, the prediction of a superior performance for the single-grating setup could not be confirmed by the experiments. As reason for this, the low visibility of the single-grating setup at both energies could be identified. Nevertheless, in spite of the very low visibility, the quantitative data obtained by single-grating setup is surprisingly good.

Spatial Resolution

With regards to the spatial resolution, a similar behaviour for both setup types was expected. With the findings from the simulations the experiments were set up in a configuration, which should allow a resolution in the range of 5 μm. The simulated reconstructions did not show a material dependency, but a homogeneous spatial resolution of ≈ 5 μm.

However, the experimental determination of the spatial resolution has shown the expected material dependency in the obtained reconstructions. The targeted resolution of $5\mu m$ was reached for both setup types, but only for the materials with the lowest signal. The strong impact of the signal itself on the resolution could also be confirmed by a better spatial resolution at a higher X-ray energy. Due to instabilities of the double-grating interferometer, this high spatial resolution was not observed for each measurement. In direct comparison between the best performing double-grating measurement and the single-grating measurement, the single-grating setup gives slightly better results, but also this might be a cause from remaining instabilities.

Applications

As final proof of the enormous potential of a single-grating interferometer for high-resolution phase-contrast measurements, several user experiments were presented. The outcome from these experiments confirm the findings from the simulations and according experimental verification based on a phantom sample. While the individual experiments demonstrate the large contrast range in combination with

a high spatial resolution, they also show the high flexibility in terms of investigated material in their entirety.

7.2 Conclusion

The aim of this project was to design and establish a grating-based phase-contrast imaging modality for high spatial resolution at the synchrotron radiation facility PETRA III. With respect to the availability to a large user community, the reliability and robustness of the provided setup are main characteristics to evaluate the designed setups. The investigations by simulations and the following experimental verification have proven, that a single-grating interferometer, despite of its larger grating period, will give a similar image quality as a double-grating interferometer. Moreover, the single-grating setup has a better long-term stability during the measurement and thereof provides more reliable results. Another big advantage of the single-grating interferometer is the absence of a complex alignment procedure. Therefore, the single grating interferometer is clearly the preferred setup type aiming on high-resolution grating-based phase-contrast tomography. With an achievable resolution in the range of 5 μm, the potential of the beamlines P05 and P07 can be fully exploited and the single-grating interferometer is a successful implementation of a high-resolution phase-contrast technique. With the two key features, a freely adjustable propagation distance and the possibility to tilt the gratings, the here created grating interferometer can be operated in a continuous energy range without need for any mechanical changes. This allows to use this instrument for an extreme variety of user experiments.

Regarding previous work [26], that have shown the suitability of a single-grating interferometer for phase-contrast imaging, these investigations extend those findings significantly. On the one hand it was proven that the achievable spatial-resolution is influenced, but not limited by the grating period. On the other hand the direct comparison to a double-grating interferometer together with the variety of application examples shows the full potential of this technique. Especially the achieved ratio of spatial-resolution to sample-diameter, shows much improvement.

7.3 Outlook

To further enhance the possibilities of grating-based phase-contrast imaging, several developments in different directions are possible.

The development of micro-structure fabrication towards smaller grating periods allows to have multiple periods averaged in one pixel for a double-grating interferometer. Consequently artefacts induced by grating defects would decrease and the sensitivity at the first fractional Talbot distance would be further increased. However, smaller periods would also make the interferometer more sensitive to instabilities, primarily vibrations. Additionally, the development of smaller periods, especially for the analyser grating, where a large structure height is needed, is a challenging task.

The applicability of a smaller period grating for a single grating setup could be a desirable solution for further improvement. Grating periods in the range of 5 μm, would allow to operate the interferometer at a quarter of the current distance. Thus, higher energies are applicable as the limitation set by the possible detector distance applies a four times higher energy. Main requirement for this attempt, is the spatial resolution provided by the detector system with the scintillator screen as weakest point. The low visibility of below 10% already shows, that the current setup is operated at its limit regarding the grating period. Therefore, primary investigations for an improved single-grating setup have to start with the search for a scintillator material allowing for higher spatial resolution of the detector system.

A PETRA III

PETRA III is a third-generation synchrotron radiation source, which took up operation in 2009. It is part of the DESY research-facility located in Hamburg. With a brilliance up to $10^{21} ph/(s\ mm^2\ mrad^2\ 0.1\%\ BW)$, it is one of the most brilliant synchrotron light sources worldwide. The storage ring is operated in a top-up mode, which keeps the photon flux stable within 1%. In 2017, 17 beamlines are available for user experiments and additional beamlines will be attached to the storage ring the next years.

The X-ray beam characteristics for a 2 m undulator [107] insertion device and the resulting parameters for the beamlines P05 and P07 at the tomography setup position are listed in table A.1.

Table A.1: Storage ring and X-ray source characteristics.

Energy:	6	GeV
Circumference:	2304	m
Horizontal Emittance:	1.2	$nmrad$
Vertical Emittance:	1.2	$nmrad$
Electron Beam Current:	100	mA
Horizontal Source Size:	36	μm
Vertical Source Size:	6.1	μm
Horizontal Beam Divergence:	28	μrad
Vertical Beam Divergence:	4.0	μrad
Horizontal Beam at experiment:	≈ 7	mm
Vertical Beam at experiment:	≈ 2	mm
Energy Range at P05:	$5 - 50$	keV
Energy Range at P07:	$35 - 150$	keV

B Filtered Backprojection

To derive the algorithm for the *filtered backprojections* the *Fourier slice theorem* is utilized. It states that the the value of the 2D Fourier transform of $f(x, y)$ along a line at the inclination angle θ is given by the 1D Fourier transform of $p(r, \theta)$, the projection profile of the sinogram acquired at angle θ.

With $\mathcal{F}(\nu_x, \nu_y)$ being the 2D Fourier transform of f(x,y) and $\mathcal{P}(\nu, \theta)$ the 1D Fourier transform of $p(r, \theta)$ we can set up the equation:

$$f(x, y) = \int\limits_{-\infty}^{\infty} \int\limits_{-\infty}^{\infty} d\nu_x d\nu_y \mathcal{F}(\nu_x, \nu_y) e^{-i2\pi\nu_x x} e^{-i2\pi\nu_y y} \tag{B.1}$$

$$= \int\limits_{0}^{2\pi} d\theta \int\limits_{0}^{\infty} d\nu \nu \mathcal{F}(\nu\cos\theta, \nu\sin\theta) e^{-i2\pi\nu x \cos\theta} e^{-i2\pi\nu y \sin\theta} \tag{B.2}$$

$$= \int\limits_{0}^{2\pi} d\theta \int\limits_{0}^{\infty} d\nu \nu \mathcal{P}(\nu, \theta) e^{-i2\pi\nu(x\cos\theta + y\sin\theta)} \tag{B.3}$$

From the symmetry of the sinogram we can follow $p(r, \theta) = p(-r, \theta + \pi)$ which translates in Fourier space to $\mathcal{P}(\nu, \theta + \pi) = \mathcal{P}(-\nu, \theta)$. With this can continue

$$\int\limits_{\pi}^{2\pi} d\theta \int\limits_{0}^{\infty} d\nu \nu \mathcal{P}(\nu, \theta) e^{-i2\pi\nu(x\cos\theta + y\sin\theta)} \tag{B.4}$$

$$= \int\limits_{0}^{\pi} d\theta \int\limits_{0}^{\infty} d\nu \nu \mathcal{P}(-\nu, \theta) e^{-i2\pi\nu(x\cos(\theta+\pi) + y\sin(\theta+\pi))} \tag{B.5}$$

$$= \int\limits_{0}^{\pi} d\theta \int\limits_{-\infty}^{0} d\nu (-\nu) \mathcal{P}(\nu, \theta) e^{-i2\pi\nu(x\cos\theta + y\sin\theta)} \ . \tag{B.6}$$

This concludes to

$$f(x, y) = \int\limits_{0}^{\pi} d\theta \int\limits_{-\infty}^{\infty} d\nu |\nu|) \mathcal{P}(\nu, \theta) e^{-i2\pi\nu(x\cos\theta + y\sin\theta)} \tag{B.7}$$

$$= \int\limits_{0}^{\pi} d\theta p'(x cos\theta + y sin\theta, \theta) \tag{B.8}$$

where

$$p'(r, \theta) = \int\limits_{-\infty}^{\infty} d\nu |\nu| \mathcal{P}(\nu, \theta) e^{-i2\pi\nu r} d\nu \tag{B.9}$$

$$= p(r, \theta) \star b(r) . \tag{B.10}$$

The ramp filter b(r) is applied in frequency space as $\mathcal{B}(\nu) = |\nu|$.[1]

---

[1]Other filter functions then the ramp filter (e.g. Hanning, Ram-Lak) can be applied. The choice of filter will have an effect on the spatial resolution and noise distribution.

C Fresnel Diffraction Integral

The Fesnel diffraction integral over the area A to describe the electric field U at (x, y) is defined as [108]:

$$U_z(x, y) = \frac{e^{ikz}}{i\lambda z} \iint\limits_A U_0(x', y') e^{\frac{ik}{2z}\left[(x-x')^2+(y-y')^2\right]} \, dx' \, dy' \tag{C.1}$$

This can be seen as a convolution of then functions $U_0(x, y)$ and $e^{\frac{ik}{2z}\left[(x)^2+(y)^2\right]}$. According to the convolution theorem

$$f * g = \mathcal{F}^-1 \left\{ \mathcal{F}(f) \cdot \mathcal{F}(g) \right\} , \tag{C.2}$$

we can rewrite equation C.1 to

$$U_z(x, y) \propto \mathcal{F}^{-1} \left\{ \mathcal{F} \left\{ u_0(x', y', 0) \right\} \cdot \mathcal{F} \left\{ h(x', y') \right\} \right\} , \tag{C.3}$$

with $h_z(x, y) = e^{\frac{ik}{2z}\left[(x)^2+(y)^2\right]}$.

To reduce numerical errors from using a FFT algorithm we can use replace the Fourier transform of $h(x, y)$ by its analytical result [109]:

$$\mathcal{F}(h) \propto e^{i\pi\lambda z \nu^2} . \tag{C.4}$$

With $\nu = \sqrt{\nu_x^2 + \nu_y^2}$ as the spatial frequency this leads to an easy form of the Fresnel diffraction equation as base for simulations of a grating interferometer.

$$U_z(x, y) \propto \mathcal{F}^-1 \left\{ \mathcal{F} \left\{ U_0(x', y', 0) \right\} \cdot e^{i\pi\lambda z \nu^2} \right\} . \tag{C.5}$$

D Grating Production
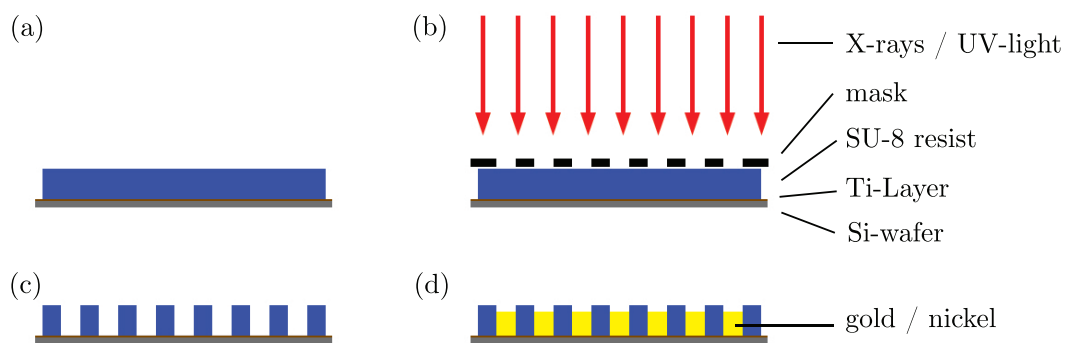
Figure D.1: Principle of the LIGA-process. (a) A Si-wafer is covered with SU-8 resist. (b) The wafer is covered with a mask of the grating layout and exposed to UV-light or X-rays. (c) Not cross-linked resist is washed away. (d) Grating structures are formed via electroplating.

The principle of grating production using the LIGA-process is outlined in figure D.1. A silicon wafer typically with a thickness of 200 μm is used as the base for the grating structure. The attempt to use different materials, such as carbon or polymer substrates is made to provide more stability along with lower attenuation [110]. Before the actual process starts, the wafers are covered with a thin slightly oxidised titanium layer. This titanium layer is later on necessary to provide the wafer with enough conductivity and a rough surface for a better adhesion of the resist.

SU-8 is a commonly used negative resist meaning that it becomes insoluble to a resist developer after exposing to X-rays or UV-light (figure D.1(a)). The resist is spread over the surface using a spin-coater. The rotation speed of the spin-coater determines the resulting thickness of the resist layer [25].

The coated wafers are covered with a mask of the grating layout and exposed to either X-rays or UV-light, dependent on the structure size and the resist height (figure D.1(b)). The radiation activates the polymer content of the resist which then starts cross-linking at the exposed areas. After the cross-linking is finished, the not exposed resist is removed using a developer solution (figure D.1(c)).

The resist on the wafer now has the negative grating layout. The grooves in this structure can be filled with metal through electroplating (figure D.1(d)). To achieve an homogeneous growing of the metal, the conductivity from the Ti-layer is necessary. After the electroplating process, the negative resist structures can be removed by plasma etching.

The high aspect ratio of the resist structures make them vulnerable to capillary forces. Therefore the step taking the wafer from the developer solution into the electroplating bath has a high risk that the resist structures collapse. To avoid collapsing structures the layout of the gratings comes with frequent connections, so-called bridges, between the resist lamellas. These connections later on result in interruptions of the grating bars which in turn limit the performance of the interferometer. Therefore new techniques are under development to avoid these bridges. The 'sunray' grating design for instance shows a significant increase of the achievable visibility. Here, the resist structure has reinforcement bars penetrating the lamellas under an angle between 30° and 45°. These reinforcement bars result in holes in the grating bars, but avoid complete interruptions [85]. Especially for high-resolution applications where the grating structures can be resolved by the detector system, the presence of bridges needs to be avoided.

E Unwrapping Algorithm

The applied unwrapping algorithm relies on comparison between the retrieved differential phase-contrast (DPC) and the derivation of the propagation-based phase-contrast (PBC). Where the difference between both signals exceeds a threshold value, 2π is added to or subtracted from the DPC signal. The best threshold value is determined by the minimum image entropy [111, 112] of the reconstruction of the modified data. Figure E.1 outlines the unwrapping procedure.
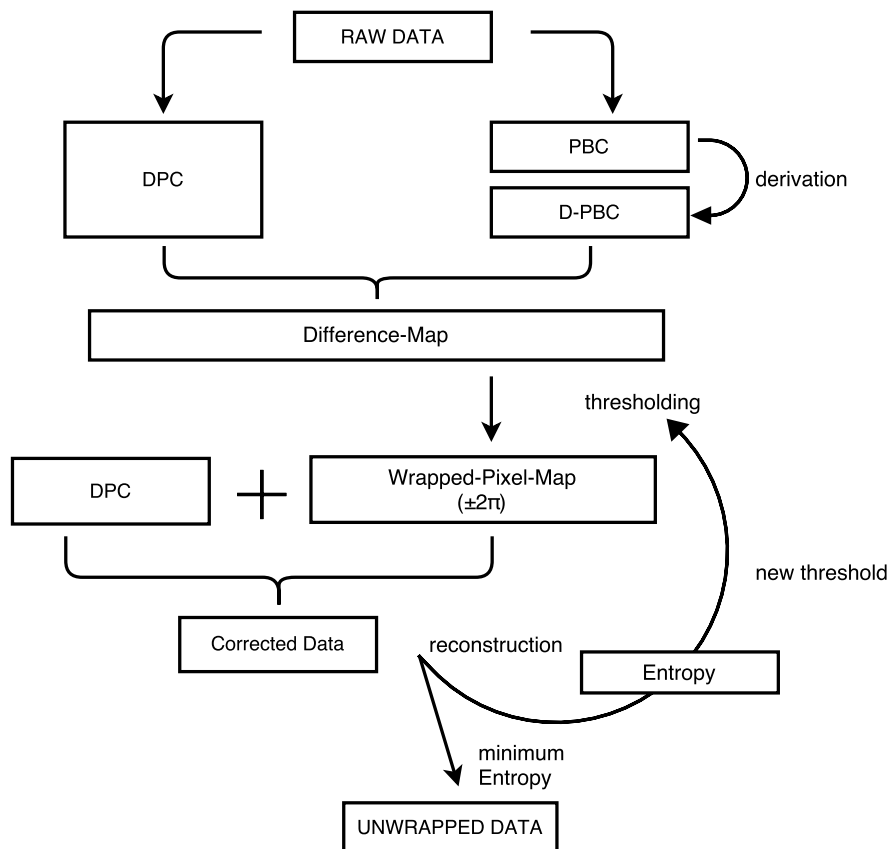
Figure E.1: Schematic of the unwrapping algorithm.

F Publications based on the developed grating interferometers

1. *Grating-based X-ray phase-contrast imaging at Petra III [86]

> In this publication the first realisation of grating-based phase-contrast at the PETRA III beamlines P05 and P07 is presented. The applicability of both setup types for a wide energy range is shown on the basis of a fixed interferometer geometry. First use cases are presented on biomedical samples.

2. *Single-grating interferometer for high-resolution phase-contrast imaging at synchrotron radiation sources [113]

> A theoretical performance analysis of a single-grating interferometer is given in this paper. With the focus on the achievable resolution it shows that a single-grating interferometer is capable to achieve the same spatial resolution than a double-grating interferometer. Experimental data compares the signal to noise ratios of a single- and double-grating interferometer.

3. *High-resolution grating interferometer for phase-contrast imaging at PETRA III [114]

> In this paper the built up setups at the beamlines P05 and P07 are presented. Additionally the capabilities of a single-grating interferometer for high-resolution grating-based phase-contrast are discussed in detail along with quantitative evaluations.

---

*first author

94

4. Advancing the visualization of pure water transport in porous materials by fast, talbot interferometry-based multi-contrast x-ray microtomography [103]

The investigations presented in this publications were carried out with the single-grating interferometer developed during this work. The high quality of the obtained data gives a proof of the high performance and reliability of the single-grating interferometer at high X-ray energies (60 keV).

5. Single and double grating-based X-ray microtomography using synchrotron radiation [92]

In this paper the performance of the single- and double-grating interferometer are compared on base of a biological object. The results confirm the findings of this thesis of a superior resolution using the single-grating setup.

6. Characterization of the CCD and CMOS cameras for grating-based phase-contrast tomography [115]

This paper compares the characteristics of a CCD-based and a CMOS-based camera and discusses their usability for grating-based differential phase-contrast.

7. Histology-validated X-ray tomography for imaging human coronary arteries [104]

In this use case the single- and double-grating interferometer were used to compare the obtained data to a histological dataset. Here, the highly calcified artery sample demands for a setup with a high dynamic range.

8. **†X-ray micro-tomography for investigations of brain tissues on cellular level** [116]

> A proof for cellular resolution using a single-grating setup and comparison to other high resolution imaging techniques.

9. **†X-ray phase micro-tomography with a single grating for high-throughput investigations of biological tissue** [117]

> Presentation of applicability of a single-grating interferometer for high resolution phase-contrast tomography based on a biological specimen.

---

†performed at Diamond Light Source, Harwell, UK

List of Figures

List of Tables

Bibliography

[1] U. Bonse and F. Busch. "X-ray computed microtomography (μCT) using synchrotron radiation (SR)". en. In: *Progress in Biophysics and Molecular Biology* 65.1-2 (Jan. 1996), pp. 133–169. DOI: `10.1016/S0079-6107(96)00011-9`.

[2] L. Helfen et al. "Viewing the Early Stage of Metal Foam Formation by Computed Tomography using Synchrotron Radiation". In: *Advanced Engineering Materials* 4.10 (Oct. 2002), pp. 808–813. DOI: `10.1002/1527-2648(20021014)4:10<808::AID-ADEM808>3.0.CO;2-U`.

[3] F. Mees et al. "Applications of X-ray computed tomography in the geosciences". en. In: *Geological Society, London, Special Publications* 215.1 (2003), pp. 1–6. DOI: `10.1144/GSL.SP.2003.215.01.01`.

[4] F. Friedrich and R. G. Beutel. "Micro-computer tomography and a renaissance of insect morphology". In: ed. by S. R. Stock. Aug. 2008, 70781U. DOI: `10.1117/12.794057`.

[5] A. Larrue et al. "Synchrotron Radiation Micro-CT at the Micrometer Scale for the Analysis of the Three-Dimensional Morphology of Microcracks in Human Trabecular Bone". en. In: *PLoS ONE* 6.7 (July 2011). Ed. by M. W. Brechbiel, e21297. DOI: `10.1371/journal.pone.0021297`.

[6] R. Fitzgerald. "Phase-Sensitive X-Ray Imaging". en. In: *Physics Today* 53.7 (2000), p. 23. DOI: `10.1063/1.1292471`.

[7] A. Bravin, P. Coan, and P. Suortti. "X-ray phase-contrast imaging: from pre-clinical applications towards clinics". In: *Physics in Medicine and Biology* 58.1 (Jan. 2013), R1–R35. DOI: `10.1088/0031-9155/58/1/R1`.

[8] A. Momose and J. Fukuda. "Phase-contrast radiographs of nonstained rat cerebellar specimen". en. In: *Medical Physics* 22.4 (Apr. 1995), pp. 375–379. DOI: `10.1118/1.597472`.

[9] F. Beckmann et al. "X-Ray Microtomography (μCT) Using Phase Contrast for the Investigation of Organic Matter:" en. In: *Journal of Computer Assisted Tomography* 21.4 (July 1997), pp. 539–553. DOI: `10.1097/00004728-199707000-00006`.

[10] Z. Qi et al. "Quantitative imaging of electron density and effective atomic number using phase contrast CT". In: *Physics in Medicine and Biology* 55.9 (May 2010), pp. 2669–2677. DOI: 10.1088/0031-9155/55/9/016.

[11] D. Paganin et al. "Simultaneous phase and amplitude extraction from a single defocused image of a homogeneous object". en. In: *Journal of Microscopy* 206.1 (Apr. 2002), pp. 33–40. DOI: 10.1046/j.1365-2818.2002.01010.x.

[12] I. Schelokov, T. Weitkamp, and A. Snigirev. "Reconstruction of an object phase transmission function from in-line X-ray holograms". en. In: *Optics Communications* 213.4-6 (Dec. 2002), pp. 247–258. DOI: 10.1016/S0030-4018(02)02081-3.

[13] A. Burvall et al. "Phase retrieval in X-ray phase-contrast imaging suitable for tomography". en. In: *Optics Express* 19.11 (May 2011), p. 10359. DOI: 10.1364/OE.19.010359.

[14] C. David et al. "Differential x-ray phase contrast imaging using a shearing interferometer". en. In: *Applied Physics Letters* 81.17 (2002), p. 3287. DOI: 10.1063/1.1516611.

[15] A. Momose, T. Takeda, and Y. Itai. "Contrast effect of blood on phase-contrast x-ray imaging". en. In: *Academic Radiology* 2.10 (Oct. 1995), pp. 883–887. DOI: 10.1016/S1076-6332(05)80067-4.

[16] S. W. Wilkins et al. "Phase-contrast imaging using polychromatic hard X-rays". In: *Nature* 384.6607 (Nov. 1996), pp. 335–338. DOI: 10.1038/384335a0.

[17] F. Pfeiffer et al. "Phase retrieval and differential phase-contrast imaging with low-brilliance X-ray sources". In: *Nature Physics* 2.4 (Apr. 2006), pp. 258–261. DOI: 10.1038/nphys265.

[18] A. Tapfer et al. "Development of a prototype gantry system for preclinical x-ray phase-contrast computed tomography: Prototype gantry system for preclinical x-ray phase-contrast CT". en. In: *Medical Physics* 38.11 (Oct. 2011), pp. 5910–5915. DOI: 10.1118/1.3644844.

[19] P. M. Bidola et al. "Optimization of propagation-based phase-contrast imaging at a laboratory setup". EN. In: *Optics Express* 23.23 (Nov. 2015), pp. 30000–30013. DOI: 10.1364/OE.23.030000.

[20] A. Khimchenko et al. "Implementation of a double-grating interferometer for phase-contrast computed tomography in a conventional system nanotom ® m". en. In: *APL Bioengineering* 2.1 (Mar. 2018), p. 016106. DOI: 10.1063/1.5022184.

[21]   T. Donath. "Quantitative X-ray microtomography with synchrotron radiation". English. PhD thesis. 2007.

[22]   J. Herzen et al. "Quantitative phase-contrast tomography of a liquid phantom using a conventional x-ray tube source". EN. In: *Optics Express* 17.12 (June 2009), pp. 10010–10018. DOI: 10.1364/OE.17.010010.

[23]   M. Willner et al. "Quantitative breast tissue characterization using grating-based x-ray phase-contrast imaging". In: *Physics in Medicine and Biology* 59.7 (2014), pp. 1557–1571. DOI: 10.1088/0031-9155/59/7/1557.

[24]   W. Bacher, W. Menz, and J. Mohr. "The LIGA technique and its potential for microsystems-a survey". In: *IEEE Transactions on Industrial Electronics* 42.5 (Oct. 1995), pp. 431–441. DOI: 10.1109/41.464604.

[25]   E. Reznikova et al. "Soft X-ray lithography of high aspect ratio SU8 submicron structures". en. In: *Microsystem Technologies* 14.9-11 (Oct. 2008), pp. 1683–1688. DOI: 10.1007/s00542-007-0507-x.

[26]   Y. Takeda et al. "X-Ray Phase Imaging with Single Phase Grating". en. In: *Japanese Journal of Applied Physics* 46.No. 3 (Jan. 2007), pp. L89–L91. DOI: 10.1143/JJAP.46.L89.

[27]   H. P. Klug and L. E. Alexander. *X-ray diffraction procedures for polycrystalline and amorphous materials.* 2d ed. New York: Wiley, 1974. ISBN: 978-0-471-49369-3.

[28]   Y. Waseda, E. Matsubara, and K. Shinoda. *X-Ray diffraction crystallography: introduction, examples and solved problems.* OCLC: ocn690089734. Heidelberg [Germany] ; New York: Springer, 2011. ISBN: 978-3-642-16634-1.

[29]   J. D. Garcia. "X-Ray Production Cross Sections". en. In: *Physical Review A* 1.5 (May 1970), pp. 1402–1403. DOI: 10.1103/PhysRevA.1.1402.

[30]   A. Snigirev et al. "On the possibilities of x-ray phase contrast microimaging by coherent high-energy synchrotron radiation". en. In: *Review of Scientific Instruments* 66.12 (Dec. 1995), pp. 5486–5492. DOI: 10.1063/1.1146073.

[31]   B. Henke, E. Gullikson, and J. Davis. "X-Ray Interactions: Photoabsorption, Scattering, Transmission, and Reflection at E = 50-30,000 eV, Z = 1-92". en. In: *Atomic Data and Nuclear Data Tables* 54.2 (July 1993), pp. 181–342. DOI: 10.1006/adnd.1993.1013.

[32] M. S. del Río and R. J. Dejus. "XOP v2. 4: recent developments of the
      x-ray optics software toolkit". In: *SPIE Optical Engineering+
      Applications*. International Society for Optics and Photonics, 2011,
      pp. 814115–814115.

[33] J. D. Ingle and S. R. Crouch. *Spectrochemical analysis*. Englewood Cliffs,
      N.J: Prentice Hall, 1988. ISBN: 978-0-13-826876-3.

[34] B. Cordero et al. "Covalent radii revisited". en. In: *Dalton Transactions*
      21 (2008), p. 2832. DOI: `10.1039/b801115j`.

[35] U. Bonse and M. Hart. "AN X-RAY INTERFEROMETER". en. In:
      Applied Physics Letters 6.8 (1965), p. 155. DOI: `10.1063/1.1754212`.

[36] V. N. Ingal and E. A. Beliaevskaya. "X-ray plane-wave topography
      observation of the phase contrast from a non-crystalline object". In:
      Journal of Physics D: Applied Physics 28.11 (Nov. 1995), pp. 2314–2317.
      DOI: `10.1088/0022-3727/28/11/012`.

[37] T. J. Davis et al. "Phase-contrast imaging of weakly absorbing materials
      using hard X-rays". In: *Nature* 373.6515 (Feb. 1995), pp. 595–598. DOI:
      `10.1038/373595a0`.

[38] D. Chapman et al. "Diffraction enhanced x-ray imaging". In: *Physics in
      Medicine and Biology* 42.11 (Nov. 1997), pp. 2015–2025. DOI:
      `10.1088/0031-9155/42/11/001`.

[39] A. Momose et al. "Demonstration of X-Ray Talbot Interferometry". en.
      In: *Japanese Journal of Applied Physics* 42.Part 2, No. 7B (July 2003),
      pp. L866–L868. DOI: `10.1143/JJAP.42.L866`.

[40] T. Weitkamp et al. "X-ray phase imaging with a grating interferometer".
      en. In: *Optics Express* 13.16 (Aug. 2005), p. 6296. DOI:
      `10.1364/OPEX.13.006296`.

[41] A. Momose. "Demonstration of phase-contrast X-ray computed
      tomography using an X-ray interferometer". en. In: *Nuclear Instruments
      and Methods in Physics Research Section A: Accelerators, Spectrometers,
      Detectors and Associated Equipment* 352.3 (Jan. 1995), pp. 622–628. DOI:
      `10.1016/0168-9002(95)90017-9`.

[42] F. A. Dilmanian et al. "Computed tomography of x-ray index of
      refraction using the diffraction enhanced imaging method". In: *Physics in
      Medicine and Biology* 45.4 (Apr. 2000), pp. 933–946. DOI:
      `10.1088/0031-9155/45/4/309`.

[43] S. Mayo et al. "X-ray phase-contrast microscopy and microtomography".
      en. In: *Optics Express* 11.19 (Sept. 2003), p. 2289. DOI:
      `10.1364/OE.11.002289`.

[44] A. Momose. "Phase-sensitive imaging and phase tomography using X-ray interferometers". en. In: *Optics Express* 11.19 (Sept. 2003), p. 2303. DOI: 10.1364/OE.11.002303.

[45] C. David et al. "Hard X-ray phase imaging and tomography using a grating interferometer". en. In: *Spectrochimica Acta Part B: Atomic Spectroscopy* 62.6-7 (July 2007), pp. 626–630. DOI: 10.1016/j.sab.2007.03.001.

[46] A. Kostenko. *Phase-contrast x-ray tomography for soft and hard condensed matter*. English. OCLC: 905870308. S.l.: s.n., 2013. ISBN: 978-94-6203-441-9.

[47] J. Herzen et al. "X-ray grating interferometer for materials-science imaging at a low-coherent wiggler source". en. In: *Review of Scientific Instruments* 82.11 (Nov. 2011), p. 113711. DOI: 10.1063/1.3662411.

[48] L. Birnbacher et al. "Experimental Realisation of High-sensitivity Laboratory X-ray Grating-based Phase-contrast Computed Tomography". In: *Scientific Reports* 6 (2016). DOI: 10.1038/srep24022.

[49] K. Takashima et al. "X-ray phase-contrast computed tomography visualizes the microstructure and degradation profile of implanted biodegradable scaffolds after spinal cord injury". In: *Journal of Synchrotron Radiation* 22.1 (Jan. 2015), pp. 136–142. DOI: 10.1107/S160057751402270X.

[50] H. Talbot. "LXXVI. Facts relating to optical science. No. IV". en. In: *Philosophical Magazine Series 3* 9.56 (Dec. 1836), pp. 401–407. DOI: 10.1080/14786443608649032.

[51] A. W. Lohmann, H. Knuppertz, and J. Jahns. "Fractional Montgomery effect: a self-imaging phenomenon". EN. In: *JOSA A* 22.8 (Aug. 2005), pp. 1500–1508. DOI: 10.1364/JOSAA.22.001500.

[52] T. Zhou et al. "Noise analysis of speckle-based x-ray phase-contrast imaging". en. In: *Optics Letters* 41.23 (Dec. 2016), p. 5490. DOI: 10.1364/OL.41.005490.

[53] H. Wang et al. "X-ray phase contrast tomography by tracking near field speckle". In: *Scientific Reports* 5 (2015). DOI: 10.1038/srep08762.

[54] T. Zhou et al. "Speckle-based x-ray phase-contrast imaging with a laboratory source and the scanning technique". en. In: *Optics Letters* 40.12 (June 2015), p. 2822. DOI: 10.1364/OL.40.002822.

[55] P. C. Diemoz et al. "Sensitivity of edge illumination X-ray phase-contrast imaging". en. In: *Philosophical Transactions of the Royal Society A: Mathematical, Physical and Engineering Sciences* 372.2010 (Jan. 2014), pp. 20130128–20130128. DOI: 10.1098/rsta.2013.0128.

[56] M. Endrizzi et al. "Asymmetric masks for laboratory-based X-ray phase-contrast imaging with edge illumination". In: *Scientific Reports* 6 (May 2016), p. 25466. DOI: 10.1038/srep25466.

[57] P. R. Munro et al. "A simplified approach to quantitative coded aperture X-ray phase imaging". en. In: *Optics Express* 21.9 (May 2013), p. 11187. DOI: 10.1364/OE.21.011187.

[58] H. Wang et al. "X-ray microscopy using two phase contrast imaging techniques: two dimensional grating interferometry and speckle tracking". In: *Journal of Physics: Conference Series* 463 (Oct. 2013), p. 012042. DOI: 10.1088/1742-6596/463/1/012042.

[59] N. Morimoto et al. "Design and demonstration of phase gratings for 2D single grating interferometer". en. In: *Optics Express* 23.23 (Nov. 2015), p. 29399. DOI: 10.1364/OE.23.029399.

[60] M. Jiang, C. L. Wyatt, and G. Wang. "X-Ray Phase-Contrast Imaging with Three 2D Gratings". en. In: *International Journal of Biomedical Imaging* 2008 (2008), pp. 1–8. DOI: 10.1155/2008/827152.

[61] I. Zanette et al. "2D grating simulation for X-ray phase-contrast and dark-field imaging with a Talbot interferometer". In: 2010, pp. 73–79. DOI: 10.1063/1.3399260.

[62] T. J. Suleski. "Generation of Lohmann images from binary-phase Talbot array illuminators". en. In: *Applied Optics* 36.20 (July 1997), p. 4686. DOI: 10.1364/AO.36.004686.

[63] F. Pfeiffer et al. "Hard-X-ray dark-field imaging using a grating interferometer". In: *Nature Materials* 7.2 (Feb. 2008), pp. 134–137. DOI: 10.1038/nmat2096.

[64] M. Bech et al. "Advanced contrast modalities for X-ray radiology: Phase-contrast and dark-field imaging using a grating interferometer". en. In: *Zeitschrift für Medizinische Physik* 20.1 (Mar. 2010), pp. 7–16. DOI: 10.1016/j.zemedi.2009.11.003.

[65] T. H. Jensen et al. "Directional x-ray dark-field imaging". In: *Physics in Medicine and Biology* 55.12 (June 2010), pp. 3317–3323. DOI: 10.1088/0031-9155/55/12/004.

[66]   M. Takeda, H. Ina, and S. Kobayashi. "Fourier-transform method of fringe-pattern analysis for computer-based topography and interferometry". en. In: *Journal of the Optical Society of America* 72.1 (Jan. 1982), p. 156. DOI: `10.1364/JOSA.72.000156`.

[67]   H. H. Wen et al. "Single-shot x-ray differential phase-contrast and diffraction imaging using two-dimensional transmission gratings". en. In: *Optics Letters* 35.12 (June 2010), p. 1932. DOI: `10.1364/OL.35.001932`.

[68]   J. Als-Nielsen and D. McMorrow. *Elements of Modern X-ray Physics: Als-Nielsen/Elements.* Hoboken, NJ, USA: John Wiley & Sons, Inc., Mar. 2011. ISBN: 978-1-119-99836-5 978-0-470-97395-0. DOI: `10.1002/9781119998365`.

[69]   T. Martin and A. Koch. "Recent developments in X-ray imaging with micrometer spatial resolution". In: *Journal of Synchrotron Radiation* 13.2 (Mar. 2006), pp. 180–194. DOI: `10.1107/S0909049506000550`.

[70]   S. Y. Lee. *Accelerator physics.* 2nd ed. Hackensack, N.J: World Scientific, 2004. ISBN: 978-981-256-182-4 978-981-256-200-5.

[71]   H. Wiedemann. *Synchrotron Radiation.* English. OCLC: 851388201. Berlin, Heidelberg: Springer Berlin Heidelberg, 2003. ISBN: 978-3-662-05312-6.

[72]   J. Nordgren et al. "Soft x-ray emission spectroscopy using monochromatized synchrotron radiation (invited)". en. In: *Review of Scientific Instruments* 60.7 (July 1989), pp. 1690–1696. DOI: `10.1063/1.1140929`.

[73]   Y. Amemiya et al. "Design of small-angle X-ray diffractometer using synchrotron radiation at the photon factory". en. In: *Nuclear Instruments and Methods in Physics Research* 208.1-3 (Apr. 1983), pp. 471–477. DOI: `10.1016/0167-5087(83)91170-5`.

[74]   U. Bonse et al. "High resolution tomography with chemical specificity". en. In: *Nuclear Instruments and Methods in Physics Research Section A: Accelerators, Spectrometers, Detectors and Associated Equipment* 246.1-3 (May 1986), pp. 644–648. DOI: `10.1016/0168-9002(86)90167-1`.

[75]   B. P. Flannery et al. "Three-Dimensional X-ray Microtomography". en. In: *Science* 237.4821 (Sept. 1987), pp. 1439–1444. DOI: `10.1126/science.237.4821.1439`.

[76]   G. W. Faris and R. L. Byer. "Three-dimensional beam-deflection optical tomography of a supersonic jet". en. In: *Applied Optics* 27.24 (Dec. 1988), p. 5202. DOI: `10.1364/AO.27.005202`.

[77] T. Donath et al. "Inverse geometry for grating-based x-ray phase-contrast imaging". en. In: *Journal of Applied Physics* 106.5 (2009), p. 054703. DOI: `10.1063/1.3208052`.

[78] P. Modregger et al. "Sensitivity of X-ray grating interferometry". In: *Optics express* 19.19 (2011), pp. 18324–18338.

[79] R. Magnusson and T. K. Gaylord. "Diffraction efficiencies of thin phase gratings with arbitrary grating shape". en. In: *Journal of the Optical Society of America* 68.6 (June 1978), p. 806. DOI: `10.1364/JOSA.68.000806`.

[80] F. Wilde et al. "Micro-CT at the imaging beamline P05 at PETRA III". In: vol. 1741. 2016. DOI: `10.1063/1.4952858`.

[81] M. Stampanoni et al. "Trends in synchrotron-based tomographic imaging: the SLS experience". In: ed. by U. Bonse. Aug. 2006, p. 63180M. DOI: `10.1117/12.679497`.

[82] P. H. van Cittert. "Die Wahrscheinliche Schwingungsverteilung in Einer von Einer Lichtquelle Direkt Oder Mittels Einer Linse Beleuchteten Ebene". In: *Physica* 1.1 (Jan. 1934), pp. 201–210. DOI: `10.1016/S0031-8914(34)90026-4`.

[83] F. Zernike. "The concept of degree of coherence and its application to optical problems". In: *Physica* 5.8 (Aug. 1938), pp. 785–795. DOI: `10.1016/S0031-8914(38)80203-2`.

[84] T. Thüring. "Compact X-ray grating interferometry for phase and dark-field computed tomography in the diagnostic energy range". PhD thesis. 2013.

[85] J. Mohr et al. "High aspect ratio gratings for X-ray phase contrast imaging". In: vol. AIP Conference Proceedings 1466. 2012, pp. 41–50. DOI: `10.1063/1.4742267`.

[86] A. Hipp et al. "Grating-based X-ray phase-contrast imaging at Petra III". In: vol. Proc. SPIE 9212. 2014. DOI: `10.1117/12.2061776`.

[87] J. F. Barrett and N. Keat. "Artifacts in CT: Recognition and Avoidance". en. In: *RadioGraphics* 24.6 (Nov. 2004), pp. 1679–1691. DOI: `10.1148/rg.246045065`.

[88] A. Tapfer et al. "Experimental results from a preclinical X-ray phase-contrast CT scanner". en. In: *Proceedings of the National Academy of Sciences* 109.39 (Sept. 2012), pp. 15691–15696. DOI: `10.1073/pnas.1207503109`.

[89] C. Loebich et al. "Digital camera resolution measurement using sinusoidal Siemens stars". In: vol. Proc. SPIE 6502. 2007, 65020N–65020N.

[90]   D. Williams and P. D. Burns. "Diagnostics for digital capture using MTF". In: vol. PICS. 2001, pp. 227–232.

[91]   P. Thurner, F. Beckmann, and B. Müller. "An optimization procedure for spatial and density resolution in hard X-ray micro-computed tomography". en. In: *Nuclear Instruments and Methods in Physics Research Section B: Beam Interactions with Materials and Atoms* 225.4 (Oct. 2004), pp. 599–603. DOI: `10.1016/j.nimb.2004.05.027`.

[92]   P. Thalmann et al. "Single and double grating-based X-ray microtomography using synchrotron radiation". In: *Applied Physics Letters* 110.6 (2017). DOI: `10.1063/1.4975679`.

[93]   A. Momose et al. "High-speed X-ray phase imaging and X-ray phase tomography with Talbot interferometer and white synchrotron radiation". en. In: *Optics Express* 17.15 (July 2009), p. 12540. DOI: `10.1364/OE.17.012540`.

[94]   N. Bevins et al. "Multicontrast x-ray computed tomography imaging using Talbot-Lau interferometry without phase stepping". en. In: *Medical Physics* 39.1 (Jan. 2012), pp. 424–428. DOI: `10.1118/1.3672163`.

[95]   E. M. A. Anas, S. Y. Lee, and M. Kamrul Hasan. "Classification of ring artifacts for their effective removal using type adaptive correction schemes". en. In: *Computers in Biology and Medicine* 41.6 (June 2011), pp. 390–401. DOI: `10.1016/j.compbiomed.2011.03.018`.

[96]   C. Raven. "Numerical removal of ring artifacts in microtomography". en. In: *Review of Scientific Instruments* 69.8 (1998), p. 2978. DOI: `10.1063/1.1149043`.

[97]   J. Hsieh. "Adaptive streak artifact reduction in computed tomography resulting from excessive x-ray photon noise". en. In: *Medical Physics* 25.11 (1998), p. 2139. DOI: `10.1118/1.598410`.

[98]   F. Pfeiffer et al. "High-resolution brain tumor visualization using three-dimensional x-ray phase contrast tomography". In: *Physics in Medicine and Biology* 52.23 (Dec. 2007), pp. 6923–6930. DOI: `10.1088/0031-9155/52/23/010`.

[99]   F. E. Boas and D. Fleischmann. "CT artifacts: Causes and reduction techniques". In: *Imaging Med.* 4.2 (2012), pp. 229–240.

[100] F. Epple et al. "Unwrapping differential x-ray phase-contrast images through phase estimation from multiple energy data". In: *Optics Express* 21.24 (2013), pp. 29101–29108. DOI: `10.1364/OE.21.029101`.

[101] J. Herzen. "A grating interferometer for materials science imaging at a second-generation synchrotron radiation source". In: (2010).

[102] M. Born and E. Wolf. *Principles of Optics: Electromagnetic Theory of Propagation, Interference and Diffaction of Light*. Pergamon Press, 1959.

[103] F. Yang et al. "Advancing the visualization of pure water transport in porous materials by fast, talbot interferometry-based multi-contrast x-ray micro-tomography". In: vol. 9967. 2016. DOI: `10.1117/12.2236221`.

[104] M. Buscema et al. "Histology-validated X-ray tomography for imaging human coronary arteries". In: vol. 9967. 2016. DOI: `10.1117/12.2238702`.

[105] L. A. Fitzpatrick et al. "Diffuse calcification in human coronary arteries. Association of osteopontin with atherosclerosis." en. In: *Journal of Clinical Investigation* 94.4 (Oct. 1994), pp. 1597–1604. DOI: `10.1172/JCI117501`.

[106] S. Motoyama et al. "Atherosclerotic Plaque Characterization by 0.5-mm-Slice Multislice Computed Tomographic Imaging". en. In: *Circulation Journal* 71.3 (2007), pp. 363–366. DOI: `10.1253/circj.71.363`.

[107] M. Barthelmess et al. "Status of the PETRA III Insertion devices". In: (2008).

[108] J. W. Goodman. *Introduction to Fourier optics*. 3rd ed. Englewood, Colo: Roberts & Co, 2005. ISBN: 978-0-9747077-2-3.

[109] C. Kopp and P. Meyrueis. "Near-field Fresnel diffraction: improvement of a numerical propagator". en. In: *Optics Communications* 158.1-6 (Dec. 1998), pp. 7–10. DOI: `10.1016/S0030-4018(98)00549-5`.

[110] F. J. Koch et al. "Note: Gratings on low absorbing substrates for x-ray phase contrast imaging". en. In: *Review of Scientific Instruments* 86.12 (Dec. 2015), p. 126114. DOI: `10.1063/1.4939055`.

[111] D. Atkinson et al. "Automatic correction of motion artifacts in magnetic resonance images using an entropy focus criterion". In: *IEEE Transactions on Medical Imaging* 16.6 (Dec. 1997), pp. 903–910. DOI: `10.1109/42.650886`.

[112] T. Donath, F. Beckmann, and A. Schreyer. "Automated determination of the center of rotation in tomography data". en. In: *Journal of the Optical Society of America A* 23.5 (May 2006), p. 1048. DOI: `10.1364/JOSAA.23.001048`.

[113] A. Hipp et al. "Single-grating interferometer for high-resolution phase-contrast imaging at synchrotron radiation sources". In: vol. Proc. SPIE 9967. 2016. DOI: `10.1117/12.2237582`.

[114]   A. C. Hipp et al. "High-resolution grating interferometer for
        phase-contrast imaging at PETRA III". In: ed. by B. Müller and
        G. Wang. SPIE, Sept. 2017, p. 7. ISBN: 978-1-5106-1239-6
        978-1-5106-1240-2. DOI: 10.1117/12.2273892.

[115]   P. Lytaev et al. "Characterization of the CCD and CMOS cameras for
        grating-based phase-contrast tomography". In: vol. 9212. 2014. DOI:
        10.1117/12.2061389.

[116]   A. Khimchenko et al. "X-ray micro-tomography for investigations of brain
        tissues on cellular level". In: vol. 9967. 2016. DOI: 10.1117/12.2237554.

[117]   M.-C. Zdora et al. "X-ray phase microtomography with a single grating
        for high-throughput investigations of biological tissue". In: *Biomedical
        Optics Express* 8.2 (2017), pp. 1257–1270. DOI: 10.1364/BOE.8.001257.

Acknowledgements